UNIVERSITÀ DEGLI STUDI DI MILANO

DEPARTMENT OF PHYSICS

PH.D SCHOOL IN:
PHYSICS, ASTROPHYSICS AND APPLIED PHYSICS

CYCLE XXXIV

Soft polymeric devices for morpho-functional mimicry of biological structures

Disciplinary Scientific Sector < FIS/07 >

Ph.D Thesis of:
Marco Piazzoni

Director of the School: Prof. Matteo Paris
Supervisor of the Thesis: Prof. Cristina Lenardi

A.Y. 2021-2022

External Referees:

- Prof. Francesco Mantegazza: BioNanoMedicine Center NANOMIB, School of Medicine and Surgery, University of Milano-Bicocca, Monza, Italy.
- Prof. Marco Rasponi: Department of Electronics, Information and Bioengineering, Politecnico di Milano, Milan, Italy

Exam Board:

- Prof. Justin Cooper-White: Australian Institute for Bioengineering and Nanotechnology, School of Chemical Engineering, University of Queensland, Brisbane, Australia.
- Prof. Dominiek Reynaerts: Department of Mechanical Engineering, KU Leuven and Flanders Make Leuven, Belgium.
- Prof. Cristina Lenardi: Physics Department, Università degli studi di Milano, Milan, Italy.

Final Examination Date:

December 13th, 2021.
Physics Department, University of Milan, Italy.

Index

"*The more our world functions like the natural world, the more likely we are to endure on this home that is ours, but not ours alone*"

Janine Benyus

1. Introduction

Biomimicry: innovation inspired by nature

In the time-lapse of hundreds of millions of years, living organisms have continuously evolved within the constraints imposed by the external environment, developing a myriad of astonishing forms and abilities to be often inspirational for man. For example, geckos have millions of dry, adhesive hairs (setae) on their feet that allow them to stick to nearly any surface (**Figure 1.1**); the microstructure of shark skin significantly reduces the drag force in water; spider silk possesses extraordinary tensile strength and extensibility; vascular systems in animals comprise efficient multiscale networks of blood vessels providing tissues with oxygen and nutrients as well as removing CO_2 and wastes products [1].

Figure 1.1: The gecko's secret lies in the composite structure of its feet, on which every single toe pad is covered with millions of keratinous hair-like bristles

called setae. Each seta branches into 100-1'000 flat tips (spatulas) that exploit van der Waals forces to generate adhesion. Adapted from [1].

But how does nature provide exquisite adaptivity at all levels of organisation? How does nature acquire and process multiple inputs and respond with multiple outputs? What are the guiding principles and benefits of its inherent hierarchical organization? These and many other open questions are so complex, and sometimes even temperamental, that maybe the answers will remain forever concealed [2]. Nonetheless, the process of discovering things, knowing how they work and for what purpose, it is one of the very primordial human behaviour and it is particularly fascinating to embrace with regard of the natural world. It is not just a matter of satisfying curiosity, but a way to unlock mother nature logic, and, as Neri Oxman said, "*the beauty of being inspired by nature is where editing begins*".

In 1997 Janine Benyus paved the onset of a revolutionary discipline called biomimicry. Biomimicry can be elegantly defined as *"innovation inspired by nature"*. From a practical point of view, it is an approach to innovation that aims to solve human challenges by emulating nature's time-tested tactics. To be more precise, two different biomimicking strategies can be identified: the so-called biology-to-design method, which begins with understanding a biological phenomenon and then, applying it to a human design challenge (solution-driven), and, by contrast, the design-to-biology method, that starts with a human challenge, identifies its main core and then looks to nature to see how various organisms or ecosystems have achieved that goal (problem-driven). A range of technological advances have been inspired by living organisms and examples of biomimicry now include synthetic materials with new mechanical properties that emulate the brick-and-mortar architecture found in bone and mollusc shells; nanoparticles and cell-based therapies with strong potential for developing novel and more effective therapeutic and imaging systems; high-speed trains in Japan with a nose emulation the kingfisher bird's beak as a way of eliminating the buildup of atmospheric pressure when passing through tunnels; and

renewable energy production by using bio-engineered bacteria capable of synthesising almost 1000 litres of hydrogen gas per hectare [3].

A new era in material design

We are at the threshold of a new era for science and engineering in which biologically inspired designs offer novel and sustainable technological solutions to society's problems that may not be provided as quickly or economically by traditional approaches. To address this demand, there is a continual quest to seek new materials with unprecedented integration of properties and functionalities at minimal production costs.

The building blocks employed by living organisms are limited principally to hard bio-minerals (elastic moduli in the order of 10^9-10^{12} pascals) and soft bio-polymers (elastic moduli in the order of 10^4-10^9 Pa) phases, nevertheless, natural materials can possess extremely impressive combinations of properties far surpassing those of their single constituents and usually outperforming their man-made counterparts. Such remarkable performance essentially evolves from the ingenious manner that the building blocks are assembled over multiple length scales. The proper term to define this feature is functional gradient. In nature, functionally graded materials are fundamentally associated with changes in two sorts of ingredients: (i) the chemical compositions-constituents, and the (ii) structural characteristics, which include the arrangement, distribution, dimensions, and orientations of building units. The appendages of mantis shrimps are an extraordinary example of a biological material composed of a combination of multiple gradients (both in terms of architecture and composition), with the final result of a remarkably resilient and damage tolerant weapon (**Figure 1.2**).

Functional gradients are a basic structural element in nature but are not the only fundamental feature that distinguishes a natural material from a synthetic one. As a matter of fact, seven unique characteristics have been highlighted to describe biomaterials: (i) self-assembly; (ii) self-healing; (iii) evolutionary and environmental constraints; (iv) importance of hydration; (v) mild synthesis conditions (mostly at temperatures of 300 K and pressures of 1 atm); (vi) multi-functionality; (vii) hierarchy of structure at nano-, micro-, meso- and macro-levels [4].

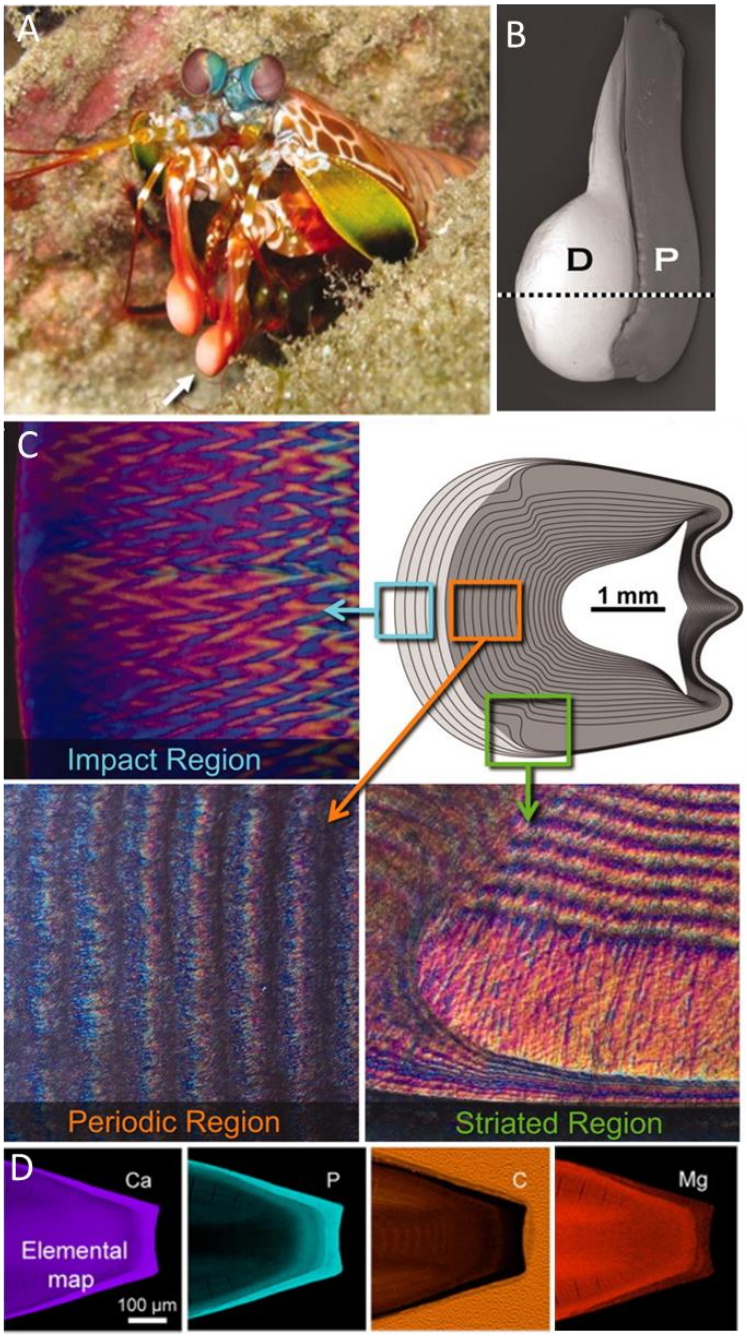

Figure 1.2: A) Picture of a peacock mantis shrimp (*Odontodactylus scyllarus*); B) Backscattered scanning electron micrograph of the club's external morphology. (D) dactyl and (P) propodus segments; C) Cross-sectional analysis of the club

illustrates the plywood structural motif of the impact region, the pseudo-laminations of the periodic region, and the thickened circumferential band with parallel chitin fibers in the striated region; D) A primary chemical gradient exists between the impact and periodic regions with the former markedly abundant in calcium and phosphorous, yet deficient in carbon and magnesium. Adapted from [5, 4].

How bioinspired advanced materials that are structurally and functionally optimized, can be designed, manufactured, and successfully employed to mimicry natural systems?

The complicated architectures in nature far exceed the capability of traditional design and fabrication technologies, which hinders the progress of biomimetic studies and their use in engineering systems. In this context, advanced manufacturing techniques like additive manufacturing (AM), many-axes machining, and advanced casting techniques have created new opportunities for manipulating and mimicking the intrinsically multiscale, multi-material, and multifunctional natural structures [6]. Particular focus has been given to AM because of its intrinsic potential of design freedom at the software level (CAD – computer-aided design) and for its freeform manufacturing at the hardware one. Nowadays many types of 3D printers capable of shaping several class of materials, including metals, polymers, ceramics and various types of composites have become available on the market. These new design capabilities allow to mould organic shapes resembling natural forms. On the long list of practical examples it is possible to find honeycomb-like structures used as lightweight objects which have found a wide range of applications in architecture, transportation, and chemical engineering; fully soft and untethered robots that, compared to those rigid, provide safer interactions with humans and a more robust adaptation to unstructured environments; and interweaving functional electronic components with biological tissues carrying the potential to generate customized replacement parts for the human body, restore loss of organs' functionality and real-time monitoring of patients' health (**Figure 1.3**) [7].

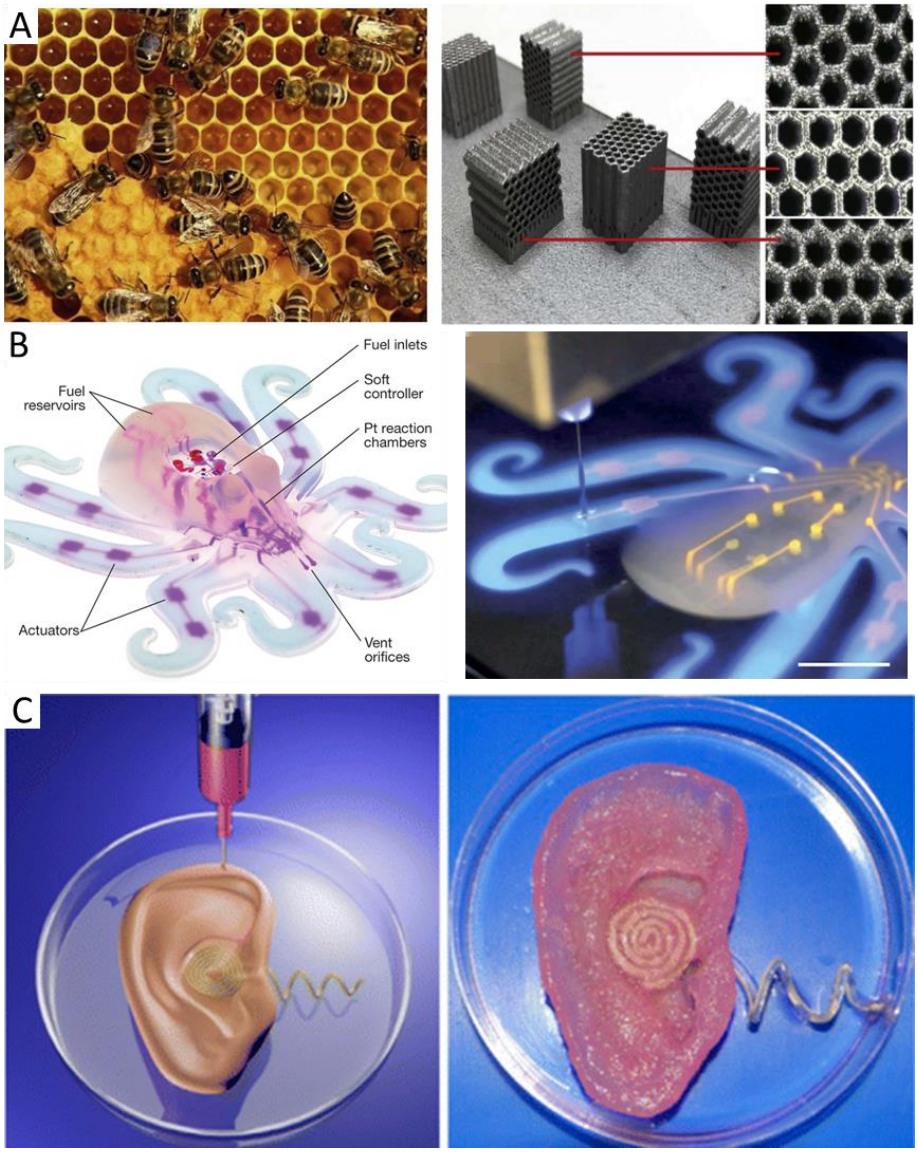

Figure 1.3: A) Honeycomb structures real (left) and 3D printed (right). Adapted from [6]; B) Fully soft, autonomous robot (right). A multi-material, embedded printing method to fabricate pneumatic networks within a moulded, elastomeric robot body (left). Adapted from [8]; C) Illustration of the 3D-printed bionic ear (left) and an electrical characterization tests (right). Adapted from [9].

A ternary paradigm for the future of biomimicry

It doesn't elicit a good feeling to be upbeat about the environment. With the planet's freshwater resources dwindling, the polar ice caps rapidly melting, and the biodiversity loss due to destruction of natural habitats, poaching, and the introduction of invasive species, to mention just a few of the unfolded ecocatastrophes, prospects for the earth and humankind do not look bright [10]. Proponents of biomimicry believe that this discipline will help to solve some of these major problems created by the global growth of industrialization and the exploitation of natural resources. However, such high hopes often create false expectations around public opinion and even among field experts about the real effectiveness of biomimicry [2]. The flow of biological knowledge into the field of design has undoubtedly led to novel discoveries across many disciplines including materials science, medicine, urban design, computer science, and robotics, but it is worth reminding that imitating nature is a very complex endeavour and being inspired by it or having good ideas is only a first step. Much work needs to be done to unleash the boasted biomimicry potential, capable of sparking a technological, environmental, and social revolution. Related to this, the European Science Foundation (ESF), published an article explaining that to meet the challenge imminent actions are required on three fronts: (i) education, to train a new generation of researchers in both life sciences and engineering disciplines before Ph.D level; (ii) collaboration, to enhance cross-fertilisation between relevant broad disciplines and for creation of international teams, not constrained by geographical boundaries; (iii) policy implications, to better support research projects by guaranteed funding and by establishing an international expert committee that would identify bottlenecks and priorities stimulating bio-inspired research on a global level [3].

1.1 Ph.D Projects & Objectives

My Ph.D. research work focused on the development of materials, manufacturing processes, and devices that aim at solving current technological issues in the field of soft robotics, tissue engineering, and environmental control of harmful insects.
In particular, in **Section 1**, it is first discussed the development of a soft material embedding a functional mechanical gradient, resembling those found in fishes propelling with body-caudal fin locomotion. Such material has been successfully used to develop an untethered soft robot swimmer (**Chapter 2**).
The second work presented in this section it is framed inside the general field of tissue engineering. A macroscopic all-soft bioreactor for *in vitro* engineering of 3D skeletal muscle cell cultures, possessing bio-mechanical features typical of the native tissue, was successfully produced (**Chapter 3**).
In **Section 2** the focus is shifted towards the use of biodegradable compounds to be employed as smart delivery systems against invasive mosquito species, particularly problematic for the public health of European countries (**Chapter 4**).

SECTION 1.

2.

Monolithic Three-Dimensional Functionally Graded Hydrogels For Bioinspired Soft Robots Fabrication

2.1 Scientific Background

2.1.1 Functionally graded biological structures

Soft robotics is an interdisciplinary research area pursuing the development of robots featured with abilities typical of living organisms, as body compliance, adaptation to unstructured environments, and a large number of degrees of freedom [11]. To this regard, one of the ten grand challenges pinpointed by Yang et al. in designing bioinspired soft robots, is to reproduce the complex hierarchy and architecture of biological tissues into monolithic bodies using synthetic materials [12]. More specifically, it is possible to find in vertebrates tissues with Young's moduli (E) spanning over seven orders of magnitude, but that can still be perfectly interfaced with each other (**Figure 2.1.1**) [13]. This is made possible by the establishment of a compliancy gradient along with the overall structure that enhances its mechanical performance minimizing stress concentration and improving interfacial bonding, and that besides, also enables it with additional functional characteristics [4]. An astonishing, but very common example of a naturally-occurring rigidity gradient, is the transition from muscle ($E = 10^4$ Pa) to bone ($E = 10^{10}$ Pa) tissue, which takes place continuously thanks to a gradual variation in protein and cellular composition [14]. Another example, typical of marine life, can be regularly observed in fish anatomy, where body flexibility increases from head to tail, so to confer greater swimming mobility [15].

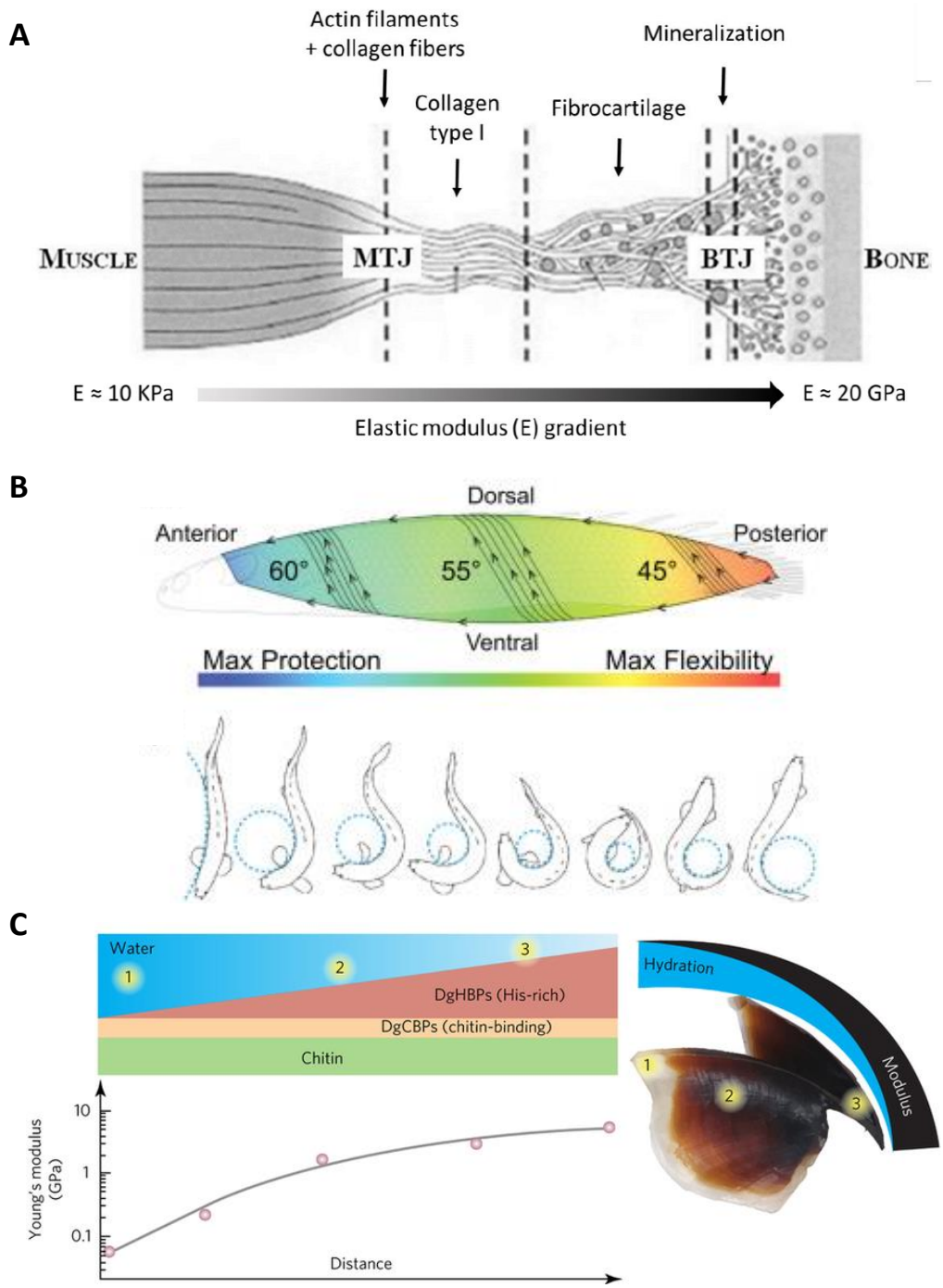

Figure 2.1.1: A) Tendon structure and junctions with muscle (MTJ) and bone (BTJ) tissues. Adapted from [16]; B) Schematic illustrating the transition from protection near the head of the fish (in blue) to flexibility near the tail of the fish (in

red). Adapted from [15];C) In the squid beak, the content of histidine-rich proteins decreases from the tip to the base, while at the same time the hydration degree varies inversely, leading to a gradient in Young's modulus. Adapted from [4].

2.1.2 Hydrogels: tunable materials

Hydrogels are polymeric materials similar to soft biological tissue in terms of their mechanical behaviour, making them ideal candidates to be employed for the fabrication of soft robot bodies [17]. Hydrogels are three-dimensional networks capable of absorbing and retaining large amounts of water, due to the presence of hydrophilic functional groups on their molecular backbone (**Figure 2.1.2**) [18]. The network can be composed of homopolymeric or co-polymeric chains which are linked together through chemical or physical crosslinks [19]. An outstanding characteristic of hydrogel-based materials is the possibility to tune their mechanical properties by engineering their chemical formulation; parameters like crosslinking density, monomer types, and reciprocal ratios, are pivotal to determine network architecture and swelling degree, thus defining the final gel stiffness [20].

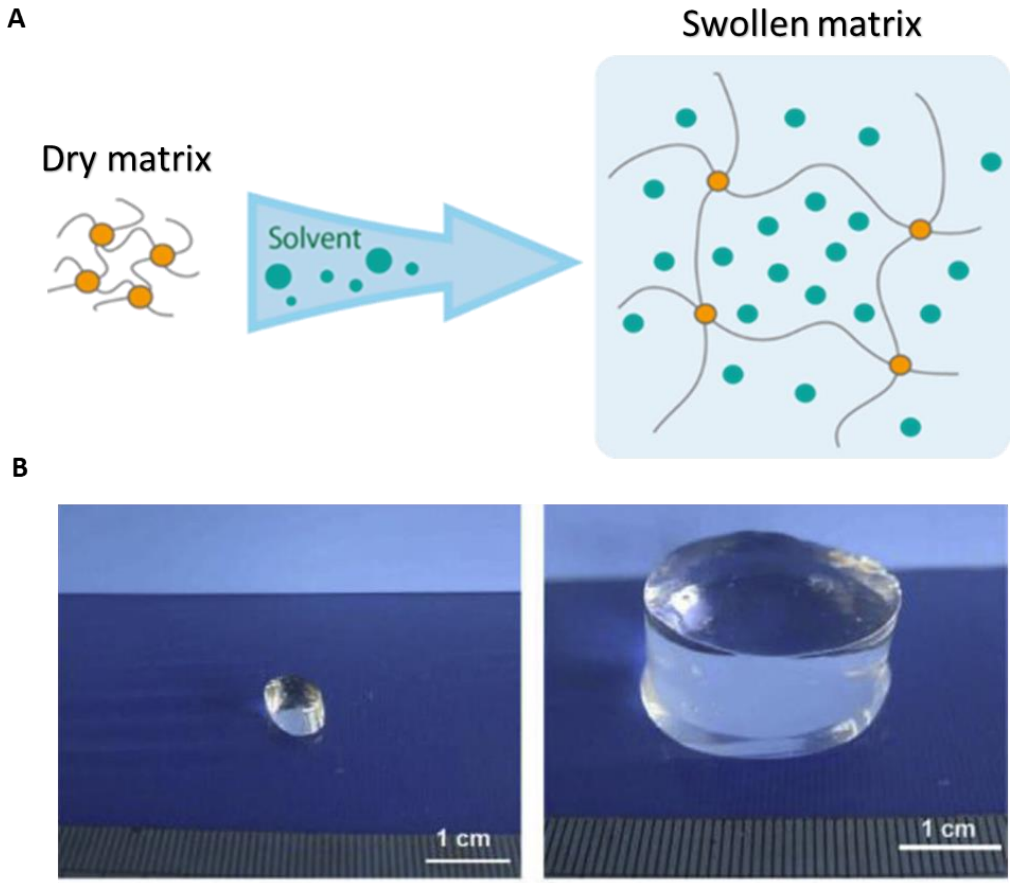

Figure 2.1.2: A) Illustration of a hydrogel matrix in a dry state (left) and in a swollen state (right) after water immersion; B) Real hydrogel based on cellulose before (left) and after (right) swelling in a 0.1 M NaCl solution. Adapted from [21].

2.1.3 Emulating natural gradients into synthetic materials

Despite the manufacturing versatility of hydrogels, the creation of morphological and mechanical gradients inside hydrogel-based monolithic structures is a technological challenge that was addressed over the past two decades with a number of different strategies (**Figure 2.1.3A, B**) [22]. The most used techniques to produce hydrogel-based functionally graded materials include stacking or rolling thin layers of different polymers over each other, and changing monomer

concentrations or crosslinking density in a selective pattern or direction [23, 24, 25, 26]. Microfluidic-assisted foaming was also investigated to generate a pore size distribution into hydrogels [27]. Such approaches represent effective solutions to engineer simple and bi-dimensional (2D) robotic systems, where length scales need to be restrained at the sub-millimeter scale. Specific practical examples manufactured with these techniques include micromechanical actuators, bioinspired shape transformers, microsurgery devices, and biodegradable smart sensors (**Figure 2.1.3C, D, E**) [17, 28, 29, 30]. However, the abovementioned approaches are not suitable to fabricate macrostructures based on three-dimensional functionally graded hydrogels (3D-FGH), preserving design freedom and avoiding laborious procedures.

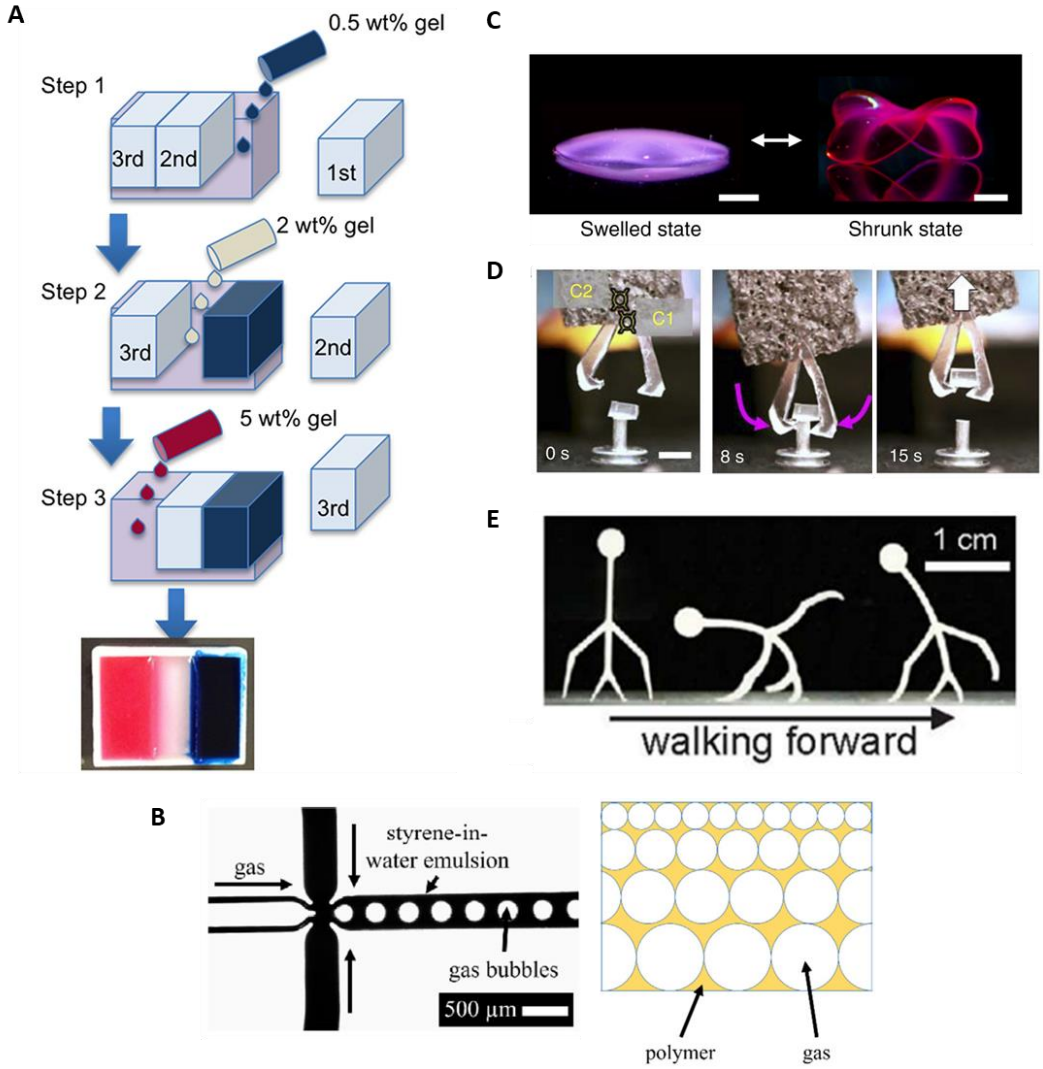

Figure 2.1.3: A) A multi properties hydrogel made with different concentrations (0.5 - 5 wt %) of low melting point agarose. For a better understanding of the gel concentration, a different colouring agent was used. Adapted from [25]; B) Microfluidic devices used to produce functionally graded foams via foamed emulsion templating. Changing the gas pressure during foam production leads to a gradient in bubble size. Adapted from [27]; C) thermo-responsive hydrogels programmed to transform into 3D structures based on gradients created with digital light projection grayscale lithography; D) Electrosensitive hydrogel soft tweezers actuating to catch a cube; E) Bidirectional locomotion of a 3D printed human-like electroactive hydrogel structure. Adapted from [29].

2.1.4 Liquid foam templating

To pursue this goal, techniques based on pores generation from a liquid foam template can be a valid route to be pursued [31]. A representative example was reported by Mac Murray et al [32]. In this work, the authors proposed a fabrication technique based on a lost-salt process to create compliant porous bodies for fluidic soft actuators. They demonstrated the possibility of tuning pore size; however, the establishment of a porosity gradient within the material was not investigated (**Figure 2.1.4A**). On the other hand, Luo et al. presented a hydrogel with a continuous graded porous structure produced by a heterobifunctional crosslinker enabled hydrothermal process [33]. The material was used to engineer several shape-changing 2D-actuators at the mesoscale, but no scale-up for the production of 3D macroscopic components was explored and furthermore, the hydrothermal synthesis required relatively high working temperatures (180°C) (**Figure 2.1.4B**).

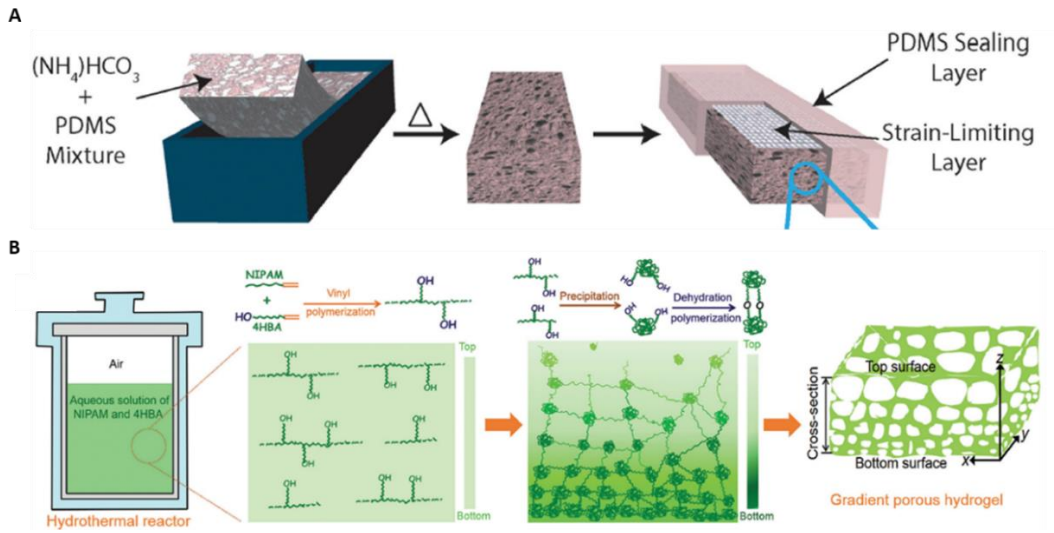

Figure 2.1.4: A) Bending actuator fabrication process: curing porogen and PDMS mixture together, heating to remove porogen, and patterning inextensible fiber under a PDMS sealing layer. Adapted from [32]; B) Reaction process of hydrothermally forming a gradient porous hydrogel: a pre-gel solution containing NIPAM and 4HBA in a hydrothermal reactor is heated. NIPAM is polymerized

with 4HBA, forming NIPAM polymer chains with pendant hydroxyl groups. The polymer chains are precipitated and crosslinked to form a gradient porous hydrogel. Adapted from [33].

2.1.5 Aim of the project

Here it is reported the manufacturing and characterization of 3D-FGHs fabricated using a novel liquid foam templating (LFT) technique. The material network is a co-polymer based on 2-hydroxyethyl methacrylate (HEMA) and acrylonitrile (AN) monomers, which have been photo-chemically crosslinked using polyethylene glycol dimethacrylate (polyEGDMA). To incorporate a porosity gradient within the hydrogel, we developed a foaming technique relying on the molding of a monomer-based template solution incorporating a blowing agent (ammonium bicarbonate - NH_4HCO_3). The LFT was optimized to generate a liquid foam embedding a distribution of bubbles that increased in size moving from the bottom to the top region of the mold. After complete crosslinking of the material, the solid foam presented a porous morphology with variable pores distribution conferring a heterogeneous mechanical behavior to the 3D-FGHs. Through the LFT technique, a monolithic soft swimmer is fabricated, and its body is seamlessly interfaced with an electro-responsive hydrogel able to actively provide untethered underwater actuation [34, 35]. The presence of a spatial stiffness gradient in the soft body strongly improved the swimming performance of the robot. The proposed fabrication approach constitutes a promising solution for the development of macroscopic functionally graded hydrogel-based structures and components, employable in biomimetic soft robotic applications [36].

2.2 Results & Discussions

2.2.1 LFT technique for 3D-FGHs fabrication

3D-FGHs were obtained with a custom-designed liquid foam templating (LFT) technique that relies on the thermal decomposition of the sparkling salt ammonium bicarbonate (NH_4HCO_3) to produce CO_2 and NH_3 bubbles in the monomer-based template solution [37]. The monomer-based template solution was injected inside a dedicated mold and the graded solid foam was obtained by entrapping the generated bubbles in the hydrogel network during UV-induced photo-polymerization (**Figure 2.2.1**, Experimental Section).

The LFT technique was finely engineered taking into consideration several physicochemical properties of the hydrogel foaming and technical aspects to obtain 3D-FGHs with tailored morphology. Liquid foams usually undergo several ageing mechanisms such as coalescence (breakage of the thin films separating neighboring bubbles), coarsening (gas diffusion from smaller to larger bubbles), and drainage (liquid drainage to the bottom of the foam) that inevitably modify pores' size, shape, and distribution [31]. As a consequence, the final solid foam will result randomly inhomogeneous, and this will be reflected in its mechanical properties. Our purpose was to obtain a porosity increasing along a preferential direction in order to produce a hydrogel with a smooth stiffness gradient, and we therefore could exploit some of the aforementioned ageing mechanisms to our advantage. In fact, drainage phenomena dragged the foam liquid fraction towards the bottom of the mold under the influence of gravity, while pushing bubbles on top of it [38]. Furthermore, bubbles increased in size while surfacing due to pressure reduction and tended to aggregate more because coalescence and coarsening phenomena were far more intense in zones characterized by a low liquid fraction [31]. For such reasons, by maintaining the mold upright throughout the whole hydrogel polymerization process, it was

possible to obtain a liquid foam template with bubbles possessing diameters increasing along the vertical direction (**Figure S4**, Supporting Information).

However, viscosity was a key factor that proved to be necessarily adjusted to build up and stabilize the graded foam until the onset of gelation. In fact, the native monomer-based template solution viscosity (2.30 mPa×s) was not high enough to stabilize the liquid foam (**Figure S3**, Supporting Information), and as a result, bubbles quickly rose to the top surface and easily escaped from it. We decided to partially cure the template solution to be poured over the salt prior to foaming by exposing it to UV light for a total of 4 minutes since it is known that highly viscous solutions make more stable foams [39, 40]. In this way, the new viscosity value (20.71 mPa×s) guaranteed enough liquid foam stabilization to entrap the bubble gradient. On the other hand, foaming needed to be terminated before high crosslinking degrees started hampering bubble formation. To this purpose, parameters such as blowing agent amount (100 mg) and hot bath temperature (T_{water} = 62° C) were selectively chosen, on an empirical basis, to ensure foaming kinetics (2 minutes) consistent with the hydrogel curing timescale once reached the required viscosity.

The proposed manufacturing approach can be easily translated to other hydrogel template solutions by adjusting viscosity (in the order of tens of mPa×s) and foaming parameters, so to obtain stable and graded foams before the onset of gelation.

The presented templating method enables the fabrication of monolithic hydrogel-based graded foams without changing the intrinsic swelling ability of the material since no crosslinking density gradients are present in the structure. This in turn avoids undesired deformations of the manufactured part in aqueous environments, which could take place from different local water uptakes and swelling capabilities of the polymeric network.

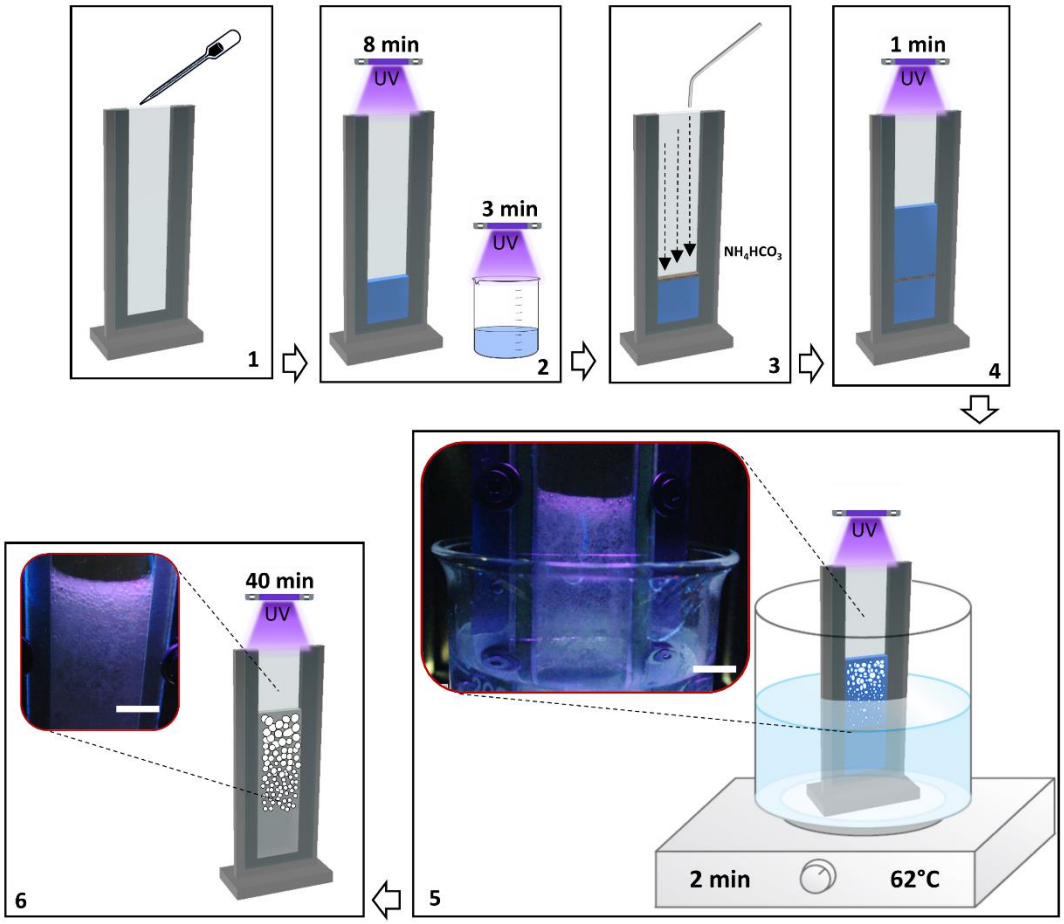

Figure 2.2.1: Schematic representation of the manufacturing process by LFT. The template solution is pipetted inside the custom-made mold (1) and is exposed to UV light (2). Ammonium bicarbonate is added on top of the cured hydrogel present inside the mold (3) and it is covered with other template solution. The hydrogel is again exposed to UV light (4), before being placed inside a hot water bath for foaming (5). UV-induced photo-polymerization is carried out for a total of 40 minutes (6). Scale bar in sub-images 5 and 6 is 15 mm.

2.2.2 3D-FGHs inhomogeneous deformation

Uniaxial tensile tests were performed on the 3D-FGHs at a constant displacement rate. **Figure 2.2.2A** reports digital image correlation (DIC) analysis images, reproducing the true strain measured in the loading

direction z (ε_z), within the area of interest (AOI) for one of the tested specimens. The images correspond to different values of the nominal strain (ε_n). As it can be observed, the strain is almost homogeneous along the specimen width direction (y-axis), whereas a pronounced strain localization can be observed considering the specimen length direction (z-axis), especially at higher values of ε_n. In particular, the strain increases moving from the bottom of the specimen, where the material is less expanded, to the top of the specimen, where the material is more expanded. Low values of strain are measured beyond the expanded zone because the hydrogel becomes again in a fairly bulky state (Experimental Section). **Figure 2.2.2B** reports the true strain measured along the z-axis, ε_z, at different values of ε_n for three specimens. Strain distribution is quite similar among samples, but some differences in strain peaks localization can be detected. Nevertheless, the hydrogel specimens' region undergoing the highest deformations is always placed in correspondence of the most expanded zones.

Uniaxial tensile tests on bulky hydrogel specimens were performed in the same conditions adopted for the 3D-FGHs. In this case, DIC analysis images (**Figure 2.2.2C**) showed that the strain is highly homogeneous both along the specimen length (z-axis) and along its width (y-axis) and, even though small peaks are observable at higher values of deformation (**Figure 2.2.2D**), it was possible to calculate a mean deformation value (ε_m) across the entire specimen gauge length. This allowed evaluation of the bulky hydrogel Young's modulus as the slope of the stress-strain curve at low strains (**Figure S6**, Supporting Information), which results to be 0.37 ± 0.03 MPa.

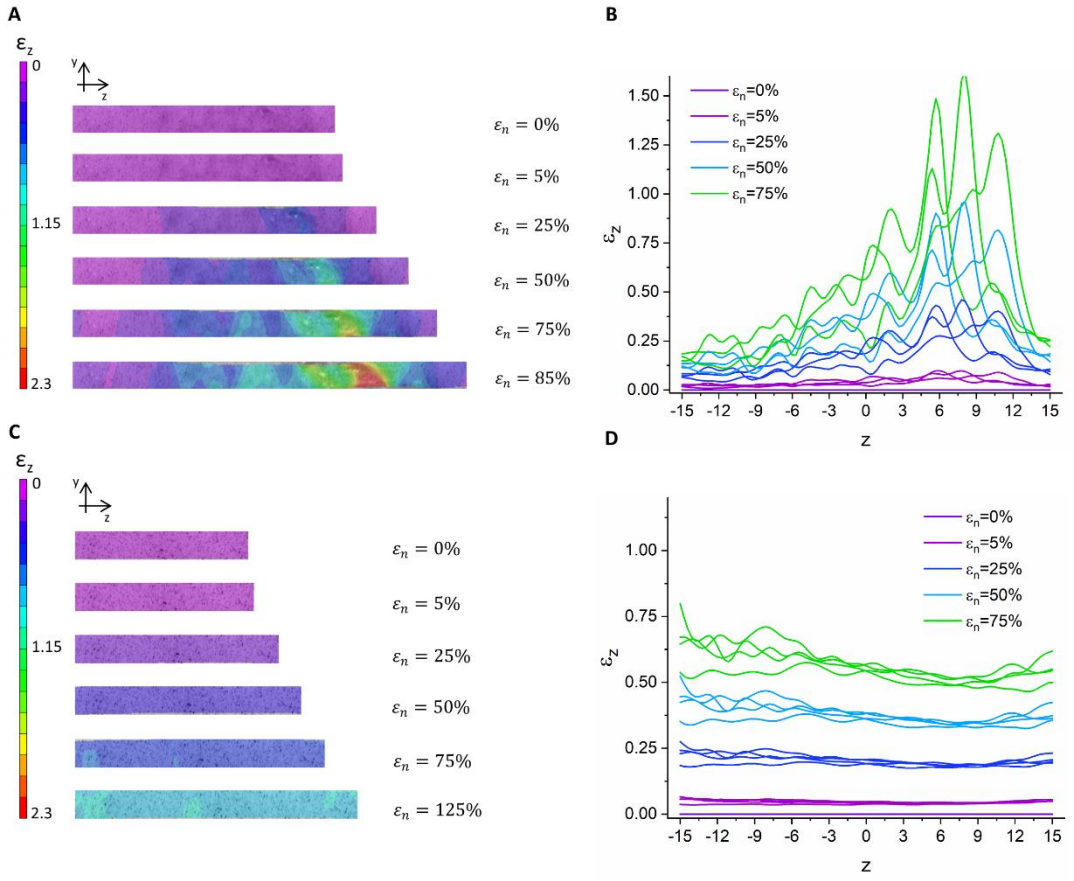

Figure 2.2.2: A) DIC analysis images within the area of interest (AOI) of one 3D-FGH specimen, reproducing the maps of the true strain measured in the loading direction z (ε_z), at different values of the nominal strain (ε_n) equal to 0, 5, 25, 50, 75 and 85% (the maximum ε_n reached). B) True strain (ε_z) of 3D-FGHs specimens measured along the z-axis versus a spatial coordinate (L) whose origin is in the centre of the specimen, at different values of ε_n equal to 0, 5, 25, 50, 75 %. C) DIC analysis images within the AOI of one bulky hydrogel specimen reproducing the maps of the true strain measured in the loading direction z, at different values of the ε_n equal to 0, 5, 25, 50, 75, 125 % (the maximum ε_n reached). D) ε_z of bulky hydrogels specimens measured along the z-axis versus L whose origin is in the centre of the specimen, at different values of ε_n equal to 0, 5, 25, 50, 75 %.

2.2.3 Structure versus mechanical response of 3D-FGHs

To properly correlate local strain values with the material voids fraction, the gauge length volume of a 3D-FGH specimen was cut into five parts and the mean value of a porosity index (P%) was measured for each of them. The analysis was performed on two specimens and very reproducible results were obtained (± 0.01). In **Figure 2.2.3A** P% is plotted versus the coordinate z, whose origin is placed in the center of the specimen. P% is about 10 % in the external parts and it increases up to 50 % moving towards the hydrogels' highest porosity region. The same plot reports also ε_z dependency on z for a value of the nominal strain of 75 % and it can be observed a consistent trend between ε_z and P%: the higher the porosity, the higher the local strain.
Dividing the applied nominal stress by the true strain (ε_z) measured at low values of ε_n, an apparent Young's modulus (E_{app}) can be evaluated as a function of z and thus, of P%. In **Figure 2.2.3B**, E_{app} is plotted versus the porosity index. The bulky hydrogel modulus E (0.37 MPa) is also reported for a P% value equal to zero. Notably, these results clearly show that there is a perfect correspondence between the structural variation of the material and its mechanical behavior, mirroring the generation of a seamless stiffness gradient into the hydrogel (**Figure 2.2.3C**). For such reason, our 3D-FGH can be considered a promising candidate material able to mimic the morpho-functional relationship typical of those soft biological structures that can change their mechanics gradually without abrupt interruptions.

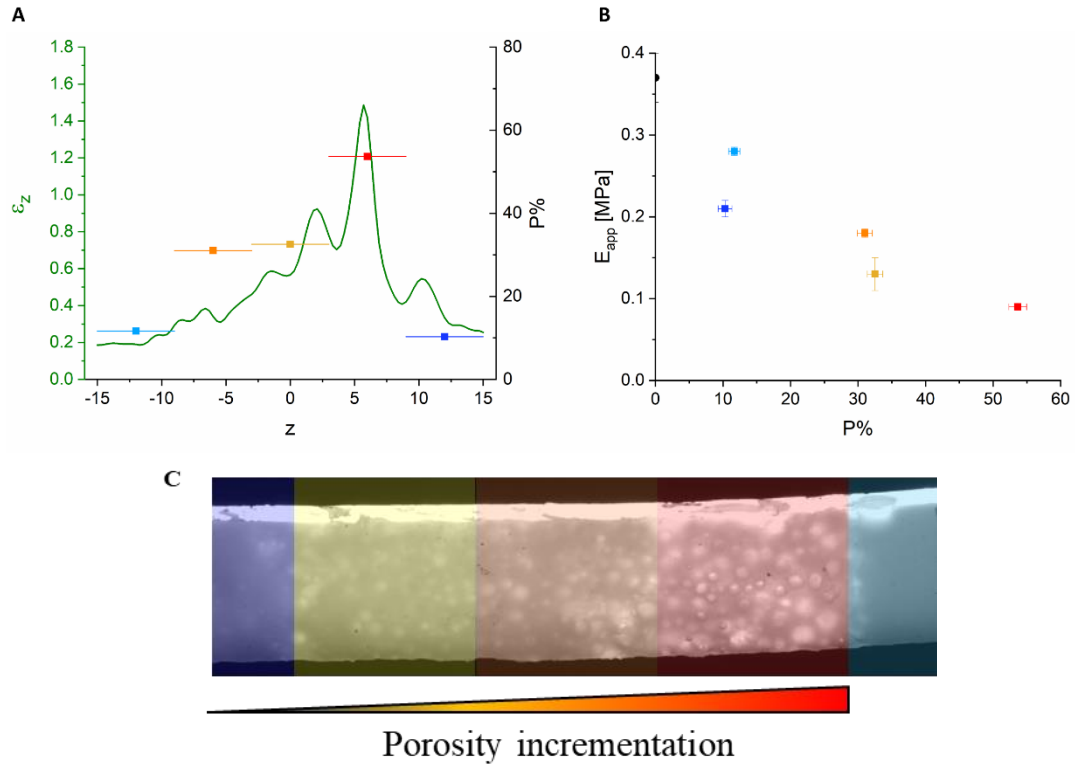

Figure 2.2.3: A) The plot reports the distribution of the true strain measured along the z loading direction (ε_z), for a value of the nominal strain of 75%, and the distribution of porosity (P%), along with the specimen on z. Each hydrogel part is represented with a different colour. The uncertainty in z corresponds to half of the length of each hydrogel part used for porosity measurement. B) Apparent elastic modulus (E_{app}) versus the index of porosity (P%) of each hydrogel part measured. The color code used in panel A is maintained. C) A picture of a real 3D-FGH specimen. The colour-coded bars schematically depict zones with different porosity.

2.2.4 3D bioinspired soft swimmers

Taking inspiration from marine biology, we designed a functionally graded (FG) swimmer with morpho-functional properties typical of those fish propelling with a body/caudal fin (BCF) locomotion, by employing our 3D-FGH as the robot body's main constituent. More

precisely, the FG soft robot's swimming mechanism can be associated with the BCF sub-classification of carangiform and/or a thunniform fish, which are considered the culminating point of swimming design evolution [41]. In these fishes, body flexibility gradually increases from head to tail, enhancing the animal hydrodynamics and maneuverability [15].

The soft swimmers are provided with embedded electro-responsive hydrogel tails for actuation. This last component is a polymeric material still based on HEMA and AN monomers, but with the addition of Na-4-vinylbenzenesulfonate (Na-4-VBS) as an electro-active monomer (relative monomer molar ratio of 0.5:6.5:3 among Na-VBS, HEMA, and AN), which has been already extensively characterized by our group [34]. To fabricate the FG swimmer, first, a thin layer (100 μm thick) of the electro-responsive hydrogel was polymerized and cut into rectangles of 40 x 7 mm. Then, two of them were placed on the inner sides of the hydrogel mold's glass and UV-induced photo-polymerization was carried out by means of the LFT technique as already described. When the process ended, using a fish-shaped hollow cutter the cured hydrogels samples were punched to obtain the final swimmer design slides (**Figure 2.2.4A**). The bulky swimmer was produced using the same mold and procedure but without the addition of NH_4HCO_3.

The employed fabrication strategy allowed to produce a seamless interconnection between the body and the tails of the swimmers due to both physical and chemical crosslinking of the two materials, thus creating monolithic all-soft robots with no rigid mechanical joints. Furthermore, in the FG swimmer, a continuous stiffness gradient is built along with the overall structure, since the apparent Young's moduli reduction (E_{app} from 0.37 MPa to 0.09 MPa) across its body manages to match Young's modulus of the tails (E = 0.1 MPa) without any sudden transition [35].

The soft swimmers (**Figure 2.2.4B**) result to be around 90 mm long (tail included), a maximum of 15 mm wide and 5 mm thick. Our FG swimmer is one of the fewest examples found in the literature of underwater 3D soft robots actuated by electro-active polymers at the macroscale. In this contest, dielectric elastomers (DEs) have been employed so far as actuators, but they need extremely high voltages (kV range) to generate

fast and large displacements [42, 43]. We instead used an electro-responsive hydrogel able to provide underwater actuation at much lower voltages (V and sub-V range) [34]. In addition, since the hydrogel's actuation can be remotely controlled with an electric field applied by two distant electrodes, our underwater vehicles are completely untethered from the power source (**Figure 2.2.4C**; Supporting Information).

As shown in **Figure 2.2.4C**, the application of an AC potential at the remote electrodes causes the electro-active tails to alternatively bend in opposite directions, generating a force that results in an overall linear motion of the soft robots. The swimming behavior of the FG swimmer was compared to that one of the bulky swimmer. The optimal actuation frequency for swimming speed generation is found to be 0.3 Hz for both robot designs, nevertheless, average horizontal speed comparison (**Figure 2.2.4D**), interestingly shows that the FG swimmer outperforms the bulky swimmer at every frequency; with a maximum speed of 0.5 mm s^{-1} and 0.2 mm s^{-1} respectively. The swimming velocity results are comparable with other values found in the literature of underwater soft robots actuated by electro-active polymers at low voltages [44, 45]. These results can be explained by the progressive stiffness reduction that characterizes the FG swimmer's body structure. This last property makes the rear of the body more prone to bend with the electro-responsive tails compared to the front, producing a slight undulatory motion that limits induced drag and translates into improved hydrodynamics. In a more rigid structure, such as the bulky swimmer body, this effect is strongly limited, since the body tends to oscillate instead and, by consequences, less efficient swimming is achieved [46]. A softer bulky swimmer, on the other hand, would also underperform due to the global reduction of the body stiffness, which leads to lower natural frequencies and, hence, lower achievable speeds. Moreover, the absence of the asymmetric effect between the front and the rear of the swimmer would also decrease the thrust generation [47, 48]. A comparison of the natural frequencies and the asymmetric effects of the three different swimmer configurations is reported in Supporting Information (**Figure S8**, Supporting Information).

Another interesting characteristic of the soft robot's structure is its dimensional stability (i.e. it does not swell massively in water). As a matter of fact, by comparing the swelling degree (Q%) of the hydrogel

right after demolding with those registered upon immersion in aqueous solutions of increasing ionic strength (from 0 to 500 mM), it can be noted that no significant mass variations were observed (**Figure S5**, Supporting Information). This comes particularly handy in view of designing and molding soft robot's components with tailored 3D geometries and also for using them in a variety of real aqueous environments of possible applicative interest, since the material will preserve its structural integrity and thus, its mechanical performance.

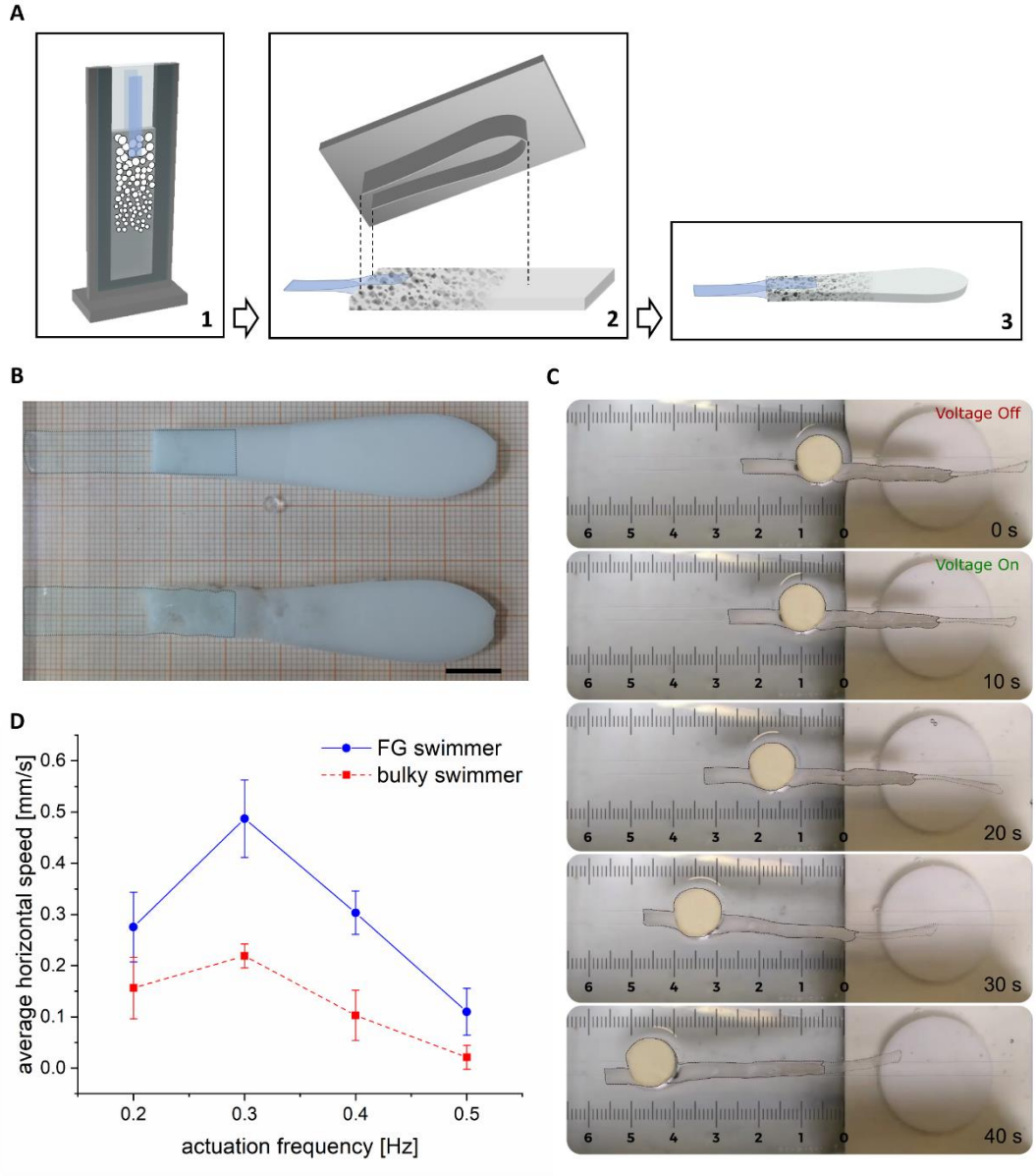

Figure 2.2.4: A) Schematic representation of the functionally graded swimmer fabrication procedure. Hydrogel curing process with the electro-responsive tails stuck on the glasses' borders (1). Swimmer hollow cutter punching the cured hydrogel (2). Functionally graded soft swimmer (3). B) bulky and functionally graded swimmers. The light blue dotted rectangles highlight the transparent

electro-responsive hydrogel tails. Scale bar is 1 cm. C) Live snapshots of the functionally graded swimmer underwater propulsion. Scale bar is in cm. D) Actuation frequency versus average horizontal speed.

2.2.5 Conclusions and future outlooks

We demonstrated a novel liquid foam templating (LFT) technique for the fabrication of 3D functionally graded hydrogels (3D-FGHs) displaying inhomogeneous mechanical response under the application of uniaxial tensile loads as a consequence of their tailored morphological properties. Robust characterization of the materials underlined a well-defined decrease in apparent Young's moduli (E_{app} from 0.37 MPa to 0.09 MPa) correlated to a density variation (P% from 0% to 50%) along with the hydrogel structure. We produced an all-soft untethered swimmer based on the 3D-FGH and provided it with integrated electro-active tails that exhibited a motility behavior mirroring that locomotion mechanism of body/caudal fin (BCF) fish. The proposed manufacturing approach is suitable for the design and development of monolithic hydrogel-based structures at the macroscale with functionally graded properties, that can find potential applications in biomimetic underwater soft robotics.

2.3 Experimental Section

2.3.1 Hydrogels' chemical formulation

The hydrogel network (**Figure S**1 and **Figure S2**, Supporting Information) is a co-polymer based on 2-hydroxyethyl methacrylate (HEMA) (MW = 130.14 g/mol) and acrylonitrile (AN) (MW = 53.06 g/mol) monomers mixed together in a reciprocal stoichiometric ratio of 6:4 (HEMA = 6 mM; AN = 4 mM). The amount of deionized water used as the solvent (4.728 ml) was set equal to 90% of the HEMA volume. UV-induced photo-polymerization was obtained using a high-power UV-lamp (Black Ray B100-AP UVP, 100 W, $\lambda = 365$ nm), polyethylene glycol dimethacrylate (polyEGDMA) (average Mn = 550) at 0.04 mM as crosslinker and 2,2-Dimethoxy-2-phenylacetophenone (DMPA) at 0.06 mM as photo-initiator.
The pre-polymer solution was always prepared in the following manner for all hydrogel samples: first, the crosslinker was weighed in a beaker, then HEMA, AN, and water were added sequentially. The solution was stirred for 10 minutes and finally, the initiator was added right before starting the polymerization procedure. After polymerization, hydrogels samples were maintained in deionized water until further testing. All reagents were purchased from Sigma Aldrich.

2.3.2 Liquid foam templating technique

3 ml of the monomer-based template solution were pipetted inside a custom-made mold and were exposed to UV light for 8 minutes. In the meanwhile, another 5 ml of template solution was exposed to UV light for 3 minutes in a beaker. Using a straw, 100 mg of ammonium bicarbonate were added on top of the cured hydrogel present inside the mold, and then, it was covered with the 3 minute-cured template solution.

At this point, the mold was again exposed to UV light for another minute, before being placed inside a hot water bath (T_{water} = 62° C) for foaming (2 minutes). Finally, the mold was extracted from the hot bath and the UV-induced photo-polymerization was carried out for a total of 40 minutes in order to completely crosslink the hydrogel.

2.3.3 Hydrogels' molding for mechanical testing

To produce 3D-FGH samples designated for mechanical testing, the LFT fabrication technique was implemented with a further step, in order to generate a bulky hydrogel region also on top of the pores. This operation proved to be necessary to ensure an even solid grip with the INSTRON testing machine clamps at both samples' terminal sides. It was achieved by pouring 4 ml of a 3-minute cured template solution on top of the liquid foam, exactly 4 minutes after mold extraction from the hot water bath. Then, UV-induced photo-polymerization was carried out for another 40 minutes (as described in **Chapter 2.2.1** and Experimental Section). Bulky hydrogel samples were produced instead by pouring the template solution (12 ml) inside the mold all at once. The mold (130 x 30 x 4 mm) was composed of an aluminum frame fitted in a rectangular base and of two glass slides. The first glass slide was glued to the back of the aluminum frame, while the front one was held in position with some screws so that it could be reversibly mounted and removed from the rest of the mold.

2.3.4 Uniaxial tensile mechanical tests

Uniaxial tensile tests were carried out on prismatic specimens (60 x 12 x 4 mm) die-cut from samples obtained as previously described. A 40 mm gauge length (L_0) was used so that 3D-FGH specimens could be clamped in the dedicated bulky regions. The tests were performed at 23° C and relative humidity of about 30 % on an INSTRON screw-driven dynamometer equipped with a load cell of 2 kN, at a displacement rate

of 6 mm min^{-1} (nominal strain rate, $\dot{\varepsilon}$ = 0.15 min^{-1}). A mechanical clamping system was adopted. All the tests have been carried out within 2 minutes from the removal of the specimen out of the deionized water. At least three specimens were tested for both the bulky and the functionally graded material. The nominal stress was evaluated as the ratio between the force (F) measured by the load cell and the undeformed specimen cross-section (A_0). The nominal strain (ε_n) was determined as the ratio between the crosshead displacement (ΔL), and the specimen gauge length (L_0).

2.3.5 Digital Image Correlation (DIC) analysis

DIC analysis was used to determine local deformations and to evaluate the non-homogeneous displacement field in strained samples. To this aim, each specimen was preliminarily painted with a black acrylic spray in order to obtain a randomly distributed spots pattern. The tests were video recorded with uEye camera and photographic lens Nikon AF Nikkor 28 - 105 mm at a rate of 1 fps. The software used for digital image correlation is Correlated Solutions Vic-2D. The area of interest (AOI) where DIC measurements were performed has a length of 30 mm: portions of specimen closer than 0.5 mm to the clamping system were not included in the analysis. A step size of 0.12 mm was used with a subset of 1.4 mm, corresponding to an overlap between subsets of about 90 %. An incremental correlation was chosen for all the analysis: in this way, any image is used as the reference one for the strain measurement performed using the following image. Data were analysed until a maximum nominal strain (ε_n) of 75 %, which is below the breakage threshold for both 3D-FGH (ε_n = 85 %) and bulky (ε_n = 125 %) samples.

2.3.5 Porosity evaluation

In order to measure the porosity (P%) and to evaluate its distribution in the 3D-FGH samples, from a specimen with the same geometry used for

uniaxial tensile tests, five prismatic specimens (8 x 12 x 4 mm) were cut along its gauge length. They were first conditioned in a thermostatic room at 23°C with a relative humidity of 30 % for at least 72 h. The volume of each conditioned specimen (V_{cond}) was measured and the relevant porosity was measured using a gas pycnometer. This measurement was performed in helium atmosphere, in accordance with ASTM D6226-15 [49]. The gas pycnometer is an instrument provided with a cylindrical chamber of known volume. A sample of known mass is placed in the chamber. Gaseous helium flows into the chamber until the volume is completely filled. From the knowledge of the chamber volume and the gas volume flown into the chamber, it is possible to evaluate the cell-wall material ($V_{cell\text{-}wall}$) volume as:

$$V_{cell-wall} = V_{cell} - V_{gas} \quad (2.1)$$

from which the porosity can be obtained as:

$$P\% = 100 * \frac{(V_{cond} - V_{cell-wall})}{V_{cond}} \quad (2.2)$$

2.3.6 Soft swimmers' assessment

The set-up for the underwater actuation consisted of a glass container filled with a 5 mM NaCl aqueous solution, two gold electrodes hold in a vertical position by plastic base support (distance = 70 mm), and two nylon wires as rails to guide the motion of the swimmer forward. A small float was inserted in the swimmers' bodies just before testing to allow proper floating. Electro-responsive hydrogel tails were actuated by applying 2.8 V/cm across the two gold electrodes. Swimming abilities were evaluated in terms of average speed on the horizontal direction at different frequencies (0.2, 0.3, 0.4, and 0.5 Hz) by using a video camera (Logitech) and a custom MatLab script capable of tracking the swimmer trajectory (**Figure S7**, Supporting Information). Results are shown as

mean and standard deviation of 4 different measurements for each frequency.

2.4 Supporting Information

Hydrogels' polymeric network characterization

The molded hydrogels (**Figure S1**) resulted in white-colored opaque materials, typical of hydrogel-based matrices presenting a globular structure. This can reasonably be ascribed to the presence of a large amount of the hydrophobic AN co-monomer included in the network. The materials also exhibited a considerable elongation ability and rubber-like properties in terms of toughness, as evaluated on a qualitative basis. These features derive from an empirical optimization of the hydrogel formulation (monomers and crosslinker type and relative molar concentrations), designed to obtain tough bulky hydrogels with Young's modulus in the order of the MPa range.

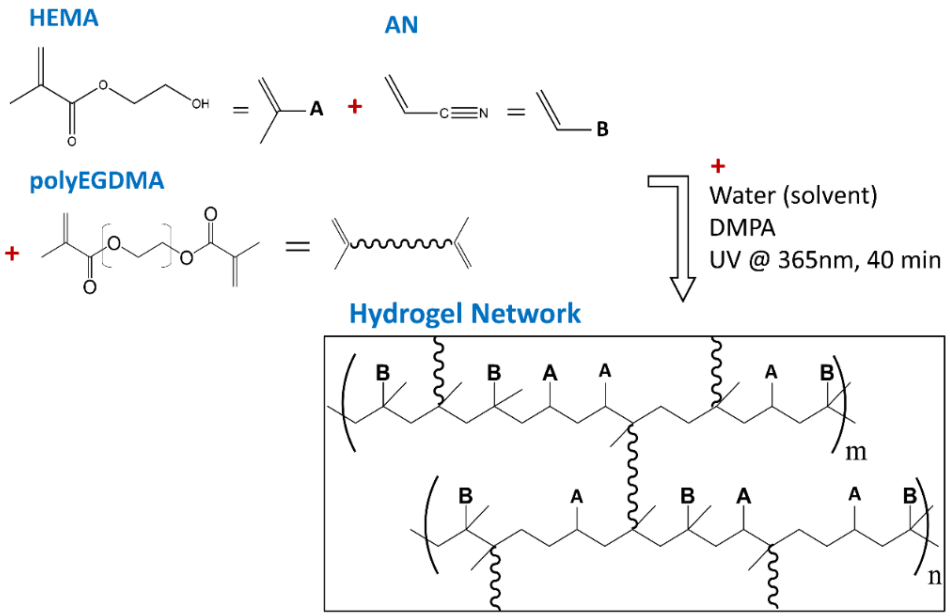

Figure S1: Schematic representation of the hydrogel network.

Attenuated total reflection (ATR)-FTIR spectroscopic studies were carried out using a PerkinElmer Frontier FTIR spectrophotometer (USA) equipped with Universal ATR (diamond/ZnSe crystal). FTIR spectra were recorded with Spectrum IR software (vers. 10.6) in the frequency range from 650 to 4000 cm^{-1} at a resolution of 1 cm^{-1}. The obtained FTIR spectra were then analyzed by using Igor Pro 8.
The Attenuated Total Reflection Fourier Transform Infrared (ATR-FTIR) spectra of reference samples, namely acrylonitrile, HEMA, and polyEGDMA are shown in **Figure S2** (upper panel), and of the synthesized gel (swelled and dry) in **Figure S2** (lower panel). Dashed vertical lines indicate the position of the main peaks, whose assignments are reported in **Table S1**.

Broadband in the range of 3300–3700 (cm^{-1})	**OH stretching**
2921	CH asym. stretching
2851	CH sym. stretching
2236	C≡N nitrile stretching
1712	C=O stretching
1640	C=C stretching
1454	CH bending
1414	C-H asym. deformation
1155	C-O stretching
1075	C-O stretching
960	CH_2 wagging

Table S1: IR peaks' assignments of the spectra shown in **Figure S2**.

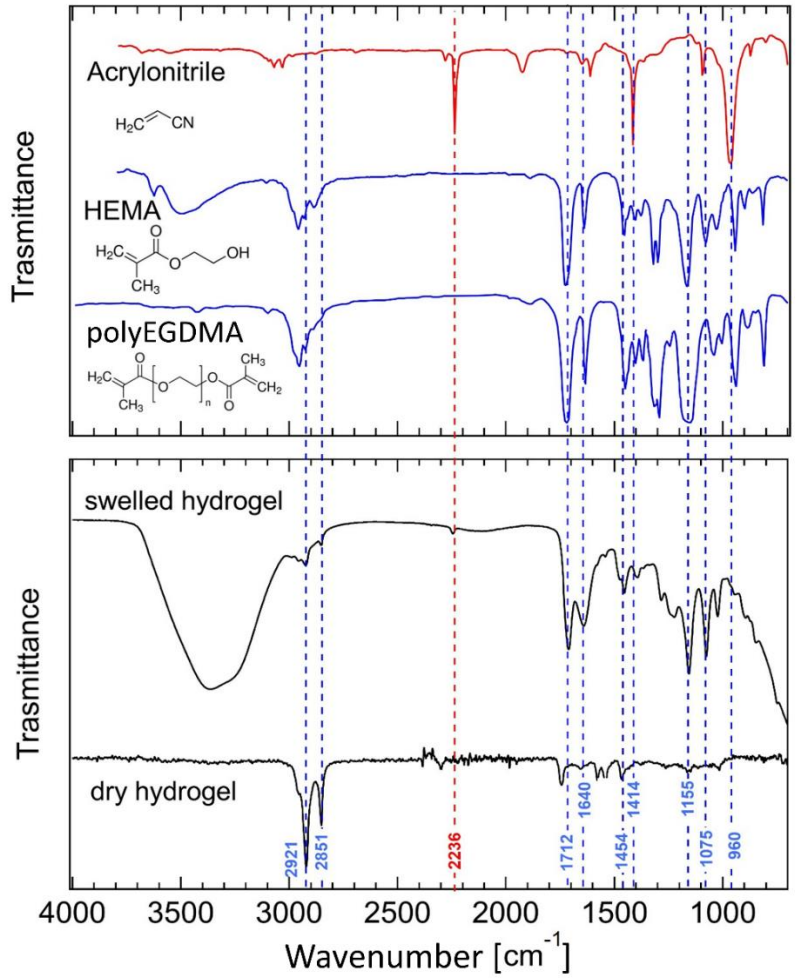

Figure S2: ATR - FTIR spectra. Upper panel: reference spectra of the components of the hydrogel. Lower panel: Spectra of the swelled and dry hydrogel. The red dashed line is associated with the nitrile group.

Template solution viscosity assessments

In order to understand at which curing time the template solution gained adequate viscosity to stabilize the liquid foam until the onset of gelation, we made several foaming experiments using template solutions with different degrees of crosslinking. In **Figure S3** are reported the most representative cases, which are template solutions cured zero, four, and seven minutes before starting the foaming process.

When the template solution was not cured, bubbles quickly rose to the top of the surface and easily escaped from the solution by winning the surface tension. Furthermore, since bubbles kept expanding, the vast majority of them collapsed on themself before the gel point was achieved. A liquid foam was not ever generated throughout the entire foaming time and the material resulted quite bulky with just a few little pores entrapped in its matrix.

By curing the template solution for four minutes, it was possible to overcome the after-mentioned problematics because the template solution gained a higher viscosity. This feature not only prevented bubbles to escape from the surface but also gave a wider window of stability to them, meaning that the foam can expand safely without collapsing until the onset of the gel point (ten minutes). Since the four minutes-cured solution gave the best results in terms of graded foams generation it was further used to produce all the samples reported in this work.

At seven minutes of curing the degree of crosslinking of the template solution still enabled bubbles expansion without collapsing but surfacing becomes hindered at a point that bubbles found preferential routes to travel favoring coarsening and coalescence phenomena instead. For such reason, at the gel point, the hydrogel displayed big holes or even channels along the entire length and a randomly porous material was generated.

The template solution viscosity (η) was measured with a custom cup viscometer using Poiseuille's law:

$$\eta = \frac{\pi r^4 \gamma t}{8V} \quad (2.3)$$

Where r is the diameter of the syringe nozzle, γ is the specific weight of the solution ($\gamma = \rho g$), t is the time that is required for the solution to flow out of the syringe and V is the solution volume. The zero minute-cured resulted to have a viscosity of 2.30 ± 0.01 mPa×s, the four minute-cured solution of 20.71 ± 4.13 mPa×s, and the seven minute-cured solution of 146.11 ± 20.53 mPa×s. Two technical replicates per condition were used.

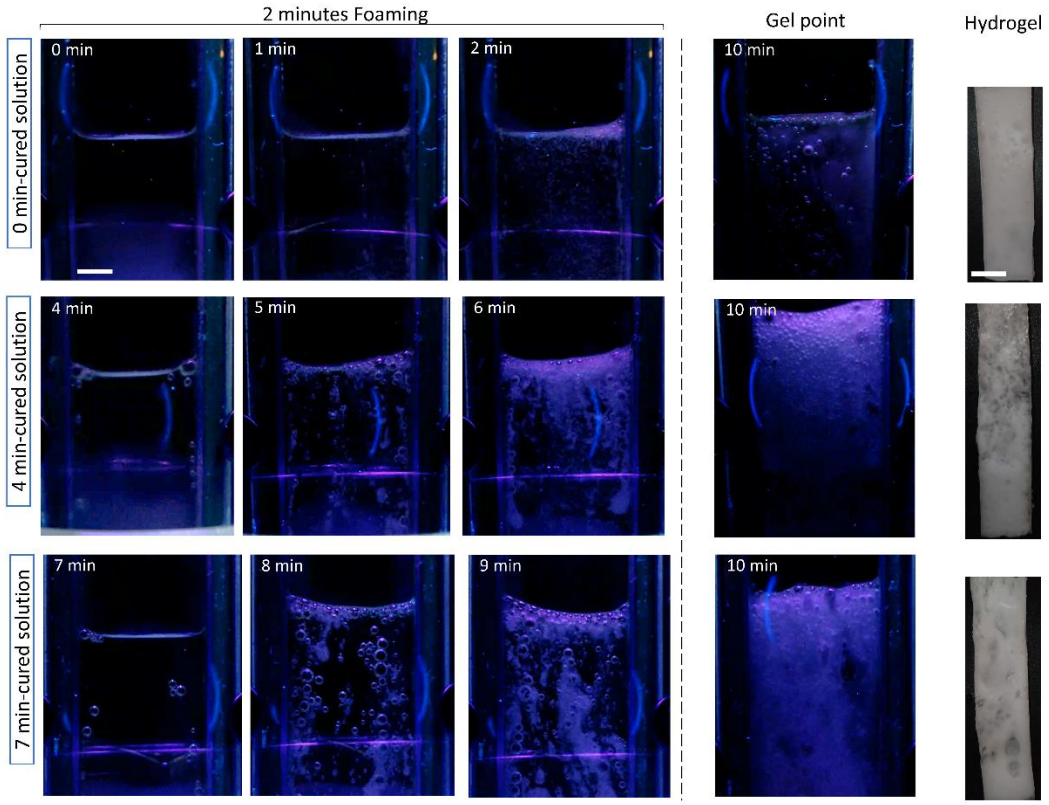

Figure S3: Impact of the template solution viscosity on the foam generation and stabilization. Zero minute-cured solution on the top row, four minute-cured solution in the middle row, and seven minute-cured solution at the bottom row. The first three columns from the left report photograms of the foaming process, the fourth the gel point of the template solution, and the fifth the completely cured hydrogel material. Scale bar is 10 mm.

Foam microstructure

The microstructure of the 3D functionally graded hydrogels was elucidated by using an optical microscope (**Figure S4**). To this purpose, a sample prepared as described in **Chapter 2.2.1**, was dissected transversally with respect to its gauge length in three different regions (bottom, middle and top). Then, since the hydrogel surface didn't reflect

light very much, it has been necessary to sputter the cut pieces with a thin layer of gold to obtain high-quality images.
Passing from panel A to C, the first difference that strikes one immediately is the progressive increment in pores' size. In the bottom region (**Figure S4A**) of the sample pores' diameter reaches 500 µm at the most, whereas in the top region (**Figure S4C**) they can go up to few millimeters. Also, the pore shape is quite different. In the bottom and middle (**Figure S4B**) sections there can be seen well rounded pores, due to the sustain of a thick bulky hydrogel matrix among them. On the other hand, pores appear less regular at the top portion, since their wall are much thinner and tended to collapse. Ultimately the 3D-FGHs can be considered a close cell foam in the less expanded region and, to a certain degree, an open-cell foam in the proximity of the highest porosity because here some pores resulted to be interconnected to each other.

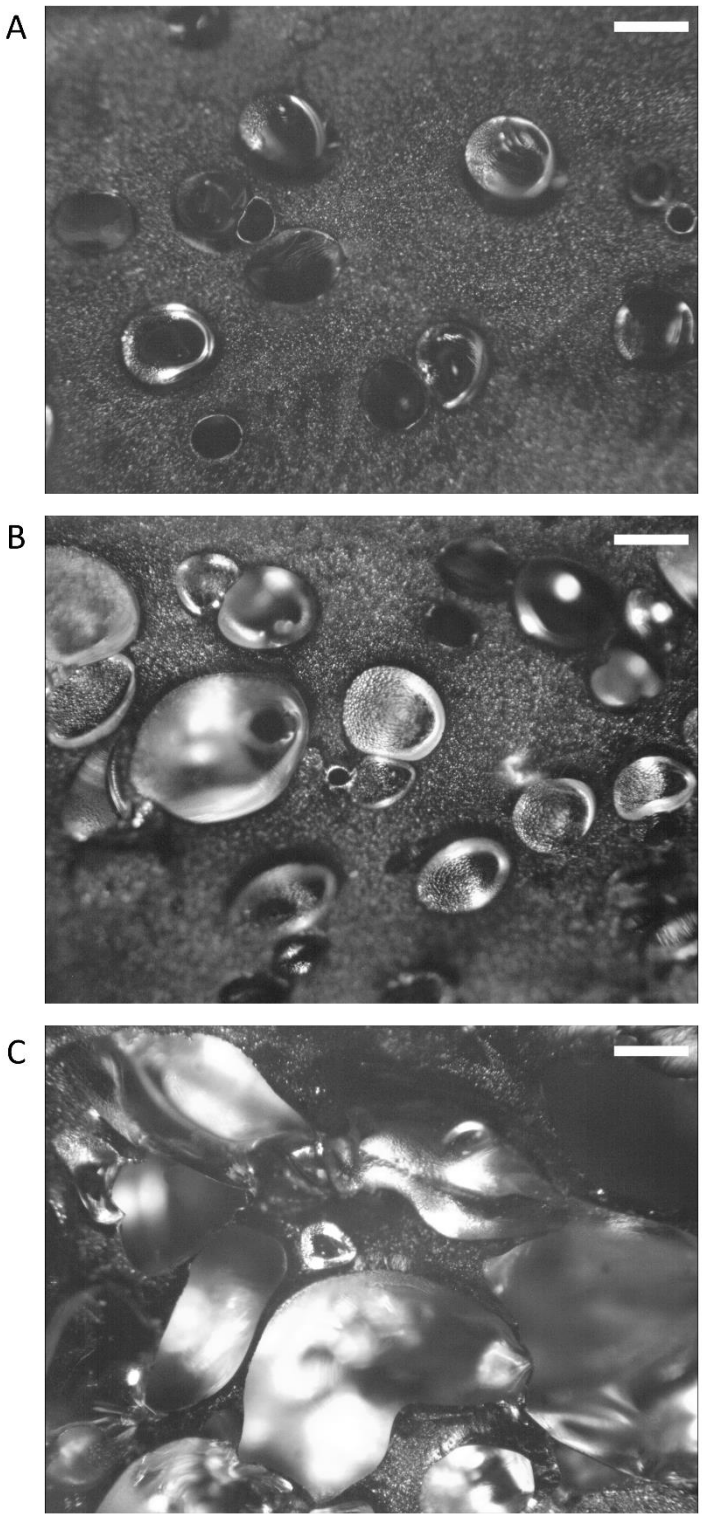
A
B
C

Figure S4: Images of the bottom (A), middle (B), and top (C) cross-sections of a 3D functionally graded hydrogel specimen. Porosity (P%) increases from panel A to C. Scale bar 500 μm.

Hydrogels' swelling degree assessment

Hydrogel samples were produced by pouring the pre-polymer solution between two glass slides separated by a silicone spacer (4 mm thick), and by exposing the mold to the UV source for 40 minutes. Cured samples were cut right after synthesis in a square shape of 10 mm side length and weighted ($W_{relaxed}$) before being equilibrated in a large excess of deionized water (MilliQ type) for 24 h at room temperature. Then, they were removed from the water, gently tapped onto filter paper, and weighed to determine their fully swollen weight (W_{swell}). After this, hydrogel samples were sequentially immersed in NaCl aqueous solutions of increasing ionic strength (IS) (from 75 to 500 мм) for 24 h at room temperature and weighted following the same procedure each time. At the end of all swelling measurements, samples were weighted to determine their dry weight (W_{dry}) after being re-equilibrated in deionized water and kept under vacuum overnight. The swelling capabilities of the hydrogel were expressed in terms of mass swelling ratio (Q%), calculated as:

$$Q\% = \frac{(W_{swell} - W_{dry})}{W_{dry}} \text{ x } 100 \quad (2.4)$$

Q% was also assessed for hydrogel straight after synthesis and demolding as:

$$Q\% = \frac{(W_{relaxed} - W_{dry})}{W_{dry}} \text{ x } 100 \quad (2.5)$$

Swelling tests showed that at equilibrium the hydrogel is capable of absorbing and retaining within its crosslinked structure a mass of deionized water (IS = 0 mM) that is about 52.6 % of its dry weight (i.e. $Q\%_0$ = 52.6 %). Interestingly, the hydrogel swelling ratio at equilibrium was essentially equal to that one registered in the relaxed state ($Q\%_{relaxed}$ = 52.2 %), i.e. straight after synthesis and de-molding. This dimensional stability between the relaxed and the equilibrated state is particularly handy when designing and molding soft components with tailored 2D or 3D geometries since significant size variations of the hydrogel will be avoided even after being immersed in water over a long time. We also monitored swelling degree variations in aqueous solutions of different ionic strength (**Figure S5**), in view of employing the hydrogel as the constituent material of a soft underwater vehicle's body. The ionic strength window chosen spanned from 75 mM to 500 mM, in order to mimic aqueous environments of possible practical interest, like surface water (IS ≈ 10^{-3} M), groundwaters (IS ≈ 10^{-2} M), physiological solutions (IS = 0.154 M) and seawaters (IS ≈ 10^{-1} M). No significative difference among swelling ratios was observed. For such reason, we can attest that the evaluated changes in ionic strength affected the hydrogel swelling behaviour very poorly, therefore allowing the material to preserve its structural integrity and mechanical properties in the proposed aqueous environments.

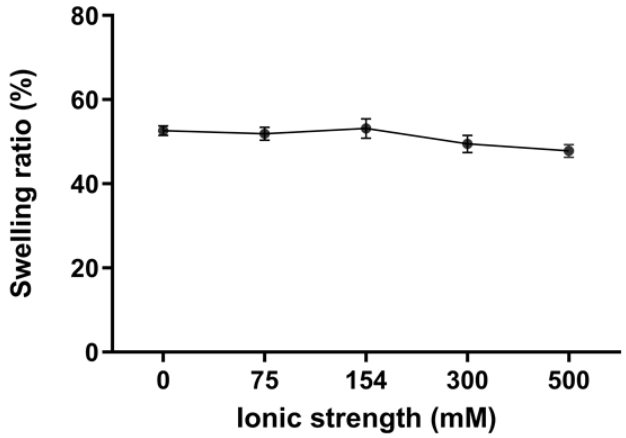

Figure S5: Swelling degree measurements at increasing ionic strength. 0 mM ($Q\%_0$ = 52.6 %), 75 mM ($Q\%_{75}$ = 51.9 %), 154 mM ($Q\%_{154}$ = 53.1 %), 300 mM ($Q\%_{300}$ = 49.5 %) and 500 mM ($Q\%_{500}$ = 47.8 %).

Bulky hydrogels' uniaxial tensile curves

In **Figure S6**, the nominal stress is plotted versus the mean deformation (ε_m) of bulky specimens. Data relevant to four specimens are reported. Data dispersion at high strain can be due to a different strain localization within the specimens. Bulky hydrogel Young's modulus was evaluated as the slope of the stress-strain curve at low strains and it resulted to be 0.37 ± 0.03 MPa.

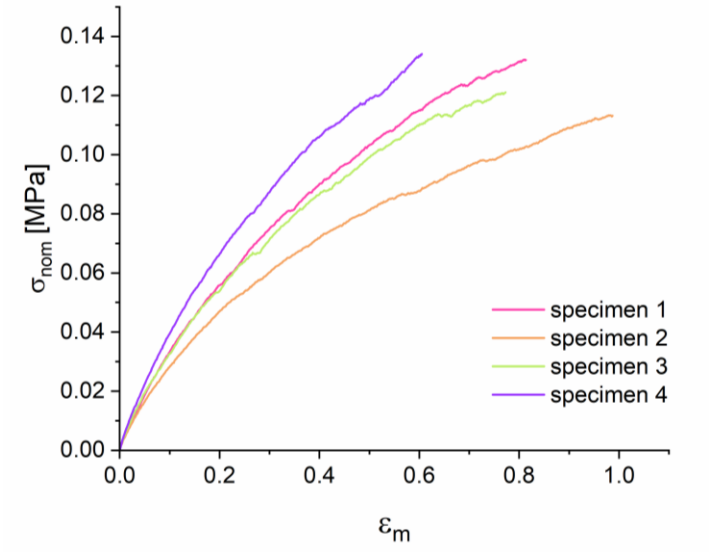

Figure S6: Nominal stress versus mean deformation (ε_m) of four relevant specimens.

Swimming velocities measurement

The motion of the two swimmers was filmed for four actuation frequencies (f) ranging from 0.2 to 0.5 Hz, over an actuation period of 50 s. The experiment was repeated four times for each frequency. Horizontal displacements were measured through video processing

using the Computer Vision Toolbox of MatLab. A circular black dot was marked on the white surface of the float and its displacement was tracked using the Object Tracking algorithm of the toolbox. The horizontal component of the displacement was extrapolated and plot in time, as depicted by **Figure S7A** for one test at f = 0.3 Hz. The actuation started after 10 s to show that the swimmer was standing still, and the subsequent motion was caused by the electro-active tail and not by floating effects. The horizontal displacement increased linearly in time with an oscillating pattern directly related to the tail oscillation. A calculation of the average speed was performed by considering the slope of the displacement linear interpolation after actuation had begun. **Figure S7B** depicts the mean value of the average speeds for the four tests, where the error bars correspond to the standard deviation.
An optimum was found at f = 0.3 Hz for both the functionally graded (FG) and the bulky swimmer. This trend is a consequence of the dynamic response of the electro-active tail. As expected, the FG swimmer achieved higher speeds at all frequencies tested due to the asymmetric stiffness of its structure.

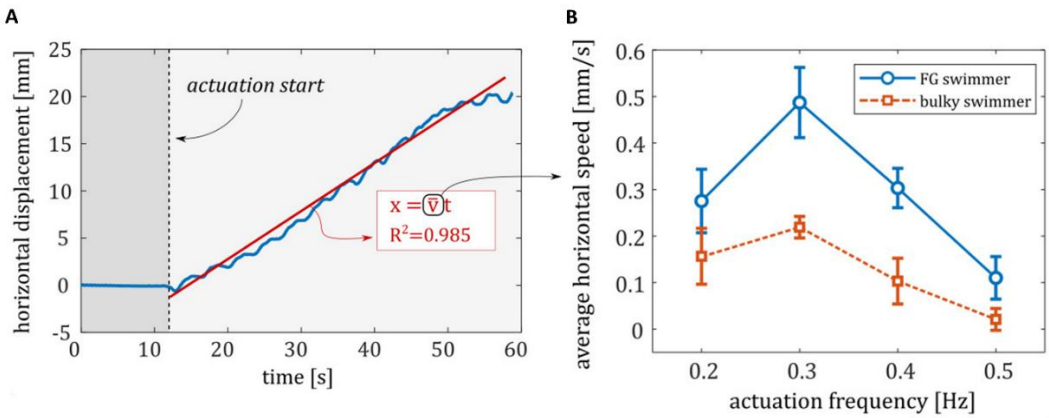

Figure S7: A) horizontal displacement for a functionally graded swimmer actuated at 0.3 Hz for 50 s. B) Actuation frequency vs average horizontal speed of both the functionally graded (blue) and bulky swimmers (orange). **Figure S5B** was already presented in **Chapter 2.2.4** and was reported here for better clarity.

Soft swimmer's simulation

In order to provide a solid basis for our conclusions, we calculated the natural frequencies of the swimmer geometry for the bulky and the FG configurations. As shown in J. Long et al. [48], fish tune their body stiffness to match their natural frequency and swim faster. To demonstrate that the higher speed of the FG swimmer does not depend solely on its softness but on the specific combination of materials and geometries, we added an extra case to the simulation of a bulky softer swimmer. The calculations are performed with a FEM analysis through the commercial software ABAQUS. The comparison is depicted in **Figure S8**. The FG swimmer gradient structure is approximated by a two-materials configuration, where the rear of the swimmer has the mechanical properties corresponding to the softer characteristic of the graded material (E = 0.09 MPa, rho = 0.44 g/cm^3) and the rest of the body to the more rigid characteristic (E = 0.37 MPa, rho = 0.88 g/cm^3). For the softer swimmer, we consider the whole swimmer body to be made of a bulky material but with the mechanical properties of the softer graded side. Using the linear perturbation analysis, we calculated both the natural frequencies and the rear and front displacement of the swimmer. Indeed, we find out that a natural frequency corresponding to the vibration mode of the electroactive tail is almost identical for the bulky and FG swimmer. The softer swimmer, on the contrary, has a lower natural frequency. Also, in terms of body displacements, the graded swimmer performs better than the bulky swimmers, because of the asymmetric distribution of stiffness. This can be deduced by calculating the difference between the rear and the front displacement, which is linked to the thrust generation. The FG swimmer outperforms both versions of the bulky swimmer, confirming our analysis made on the experimental results.

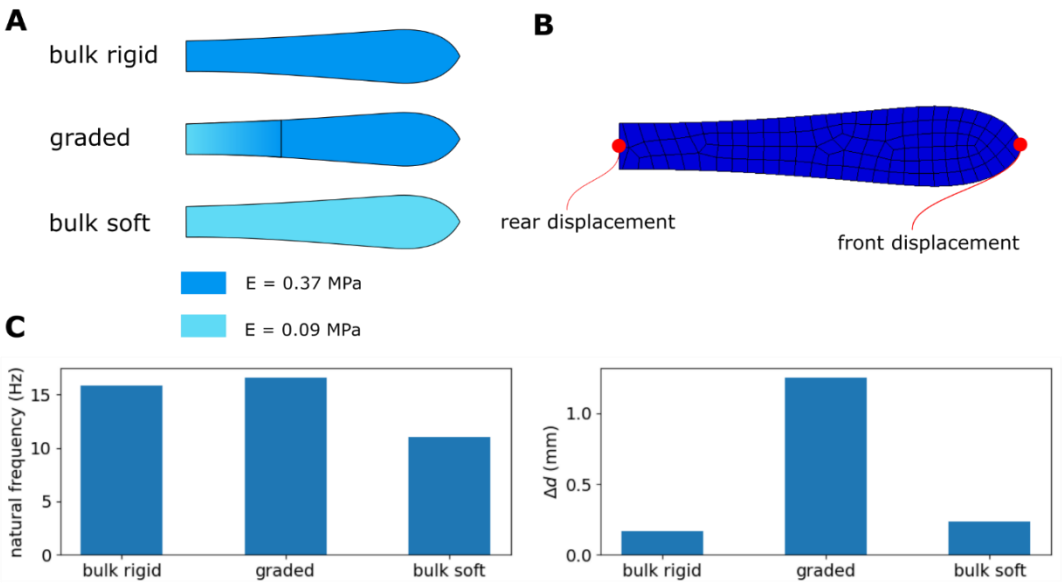

Figure S8: A) Mechanical scheme of the three swimmers simulated in ABAQUS. B) Swimmer mesh and location of the calculated displacements. C) Natural frequency (left) and differential displacement between the rear and the front (right) for the three simulated swimmers.

2.5 Publications

SOFT ROBOTICS
Volume 00, Number 00, 2021
© Mary Ann Liebert, Inc.
DOI: 10.1089/soro.2020.0137

SoRo
Soft Robotics

Monolithic Three-Dimensional Functionally Graded Hydrogels for Bioinspired Soft Robots Fabrication

Marco Piazzoni,[1,*] Elisa Piccoli,[2,*] Lorenzo Migliorini,[1] Edoardo Milana,[3] Federica Iberite,[4] Lorenzo Vannozzi,[4] Leonardo Ricotti,[4] Irini Gerges,[5] Paolo Milani,[1] Claudia Marano,[2] Cristina Lenardi,[1] and Tommaso Santaniello[1]

Abstract

Bioinspired soft robotics aims at reproducing the complex hierarchy and architecture of biological tissues within artificial systems to achieve the typical motility and adaptability of living organisms. The development of suitable fabrication approaches to produce monolithic bodies provided with embedded variable morphological and mechanical properties, typically encountered in nature, is still a technological challenge. Here we report on a novel manufacturing approach to produce three-dimensional functionally graded hydrogels (3D-FGHs) provided with a controlled porosity gradient conferring them variable stiffness. 3D-FGHs are fabricated by means of a custom-designed liquid foam templating (LFT) technique, which relies on the inclusion of air bubbles generated by a blowing agent into the monomer-based template solution during ultraviolet-induced photopolymerization. The 3D-FGHs' apparent Young's modulus ranges from 0.37 MPa (bulky hydrogel region) to 0.09 MPa (highest porosity region). A fish-shaped soft swimmer is fabricated to demonstrate the feasibility of the LFT technique to produce bioinspired robots. Mobility tests show a significant improvement in terms of swimming speed when the robot is provided with a graded body. The proposed manufacturing approach constitutes an enabling solution for the development of macroscopic functionally graded hydrogel-based structures usable in biomimetic underwater soft robotics applications.

Keywords: functionally graded hydrogels, 3D bioinspired structures, untethered soft robots, monolithic macrostructures

Introduction

Soft robotics is an interdisciplinary research area pursuing the development of robots featured with abilities typical of living organisms, as body compliance, adaptation to unstructured environments, and a large number of degrees of freedom.[1] To this regard, one of the 10 grand challenges pinpointed by Yang *et al.* in designing bioinspired soft robots is to reproduce the complex hierarchy and architecture of biological tissues into monolithic bodies using synthetic materials.[2] More specifically, it is possible to find in vertebrates tissues with Young moduli (E) spanning over seven orders of magnitude, but that can still be perfectly interfaced with each other.[3] This is made possible by the establishment of a compliancy gradient along the overall structure that enhances its mechanical performance minimizing stress concentration and improving interfacial bonding, and that besides also enables it with additional functional characteristics.[4] An astonishing but very common example of a naturally occurring rigidity gradient is the transition from muscle ($E = 10^5$ Pa) to bone ($E = 10^{10}$ Pa) tissue, which takes place continuously, thanks to a gradual variation in protein and cellular composition.[5] Another example, typical of marine life, can be regularly observed in fish anatomy, where body flexibility increases from head to tail, so to confer a greater swimming mobility.[6]

[1]CIMaINa, Department of Physics, Università degli Studi di Milano, Milan, Italy.
[2]Department of Chemistry, Materials and Chemical Engineering "Giulio Natta," Politecnico di Milano, Milan, Italy.
[3]Department of Mechanical Engineering, KU Leuven and Flanders Make, Leuven, Belgium.
[4]Department of Excellence in Robotics & AI, Scuola Superiore Sant'Anna, Pisa, Italy.
[5]Tensive S.r.l., Milan, Italy.
*Both these authors contributed equally to this work.

3.

All-Soft Bioreactor for Skeletal Muscle Tissue Engineering at the Macroscale

3.1 Scientific Background

3.1.1 3D vs 2D cell cultures

Bi-dimensional cells cultures

Cell culture is the most commonly used technique in many biomedical laboratories. The term cell culture refers to the practice of removing cells from an organism and their subsequent growth in an artificial controlled and favourable environment. As a matter of fact, every cell type requires specific culture conditions to be satisfied in order to be maintained alive *in vitro*: a solid substrate or a liquid medium to provides essential nutrients (i.e. amino acids, carbohydrates, vitamins, minerals), growth factors and hormones; a physicochemical environment to regulate levels of pH, osmotic pressure, temperature and gases (O_2, CO_2) partial pressure. Cells cultures can be classified as adherent when cells are attached to a substrate or in suspension when cells are free-floating in the medium.

Single cells are obtained from an explanted piece of tissue, which has been treated with enzymatic or mechanical disintegration tools. Cells are then placed in plastics containers (i.e. flasks or petri dishes) and are cultivated in the laboratory. At this stage, a cell culture is defined as primary, because it is directly derived from a tissue, and it has not been subcultured (passaged) yet. Primary cells are very representative of the *in vivo* situation because they usually maintained an unvaried phenotype, however, they have a finite life span and are composed of a heterogeneous population of cells.

As soon as cells are subcultured, a primary culture becomes known as a cell line (or a secondary culture). During further passages, just a predominant subpopulation of cells will be selected, building up a homogeneous population of cells called cell strain.

Normal cells usually divide only a limited number of times before losing their ability to proliferate and going into senescence. Based on the

proliferative capacity, cell lines and cell strain can be classified as finite or continuous. The finite cell line is formed by cells that can only make a limited number of divisions (approximately thirty), whereas a continuous cell line, is a culture whose cells proliferate indefinitely following changes in their genetic heritage, either spontaneously arose or induced with chemical or viral methods [50, 51].

Standard cell culture techniques are utilized in a wide variety of important biomedical fields, from basic research to diagnostic and therapy. To mention only a few examples, they are generally used as health and disease model systems, in drug development and drug testing, in tissue regeneration and transplantation, in genetic engineering and gene therapy, and in vaccine production [52]. Such broad applicability of cell cultures is due to the undeniable operational advantages that come from having a very well controlled and simple system: high reproducibility among experiments and laboratories, high throughput analysis, and relatively low-cost maintenance. Furthermore, cells can be quite easily stored in liquid nitrogen and thaw on demand.

Dimensions matter

It is well established that cells adapt to their surrounding environment by responding to local signals and cues, which in turn has consequences in their morphology, proliferation, differentiation, and general behaviour.

The growth of mammalian cells *in vitro* using traditional cell culture methods is far from reproducing the high complexity that cells encounter in native biological tissue. This is mainly due to the fact that cells are grown onto bi-dimensional polystyrene (i.e. plastics) substrates.

In this situation, cells cannot assume their natural 3D morphology but instead, they tend to remodel their cytoskeleton in a flat and spread conformation (**Figure 3.1.1**). Cell flattening may affect in turn nuclear shape, which can lead to alteration in gene expression and protein synthesis.

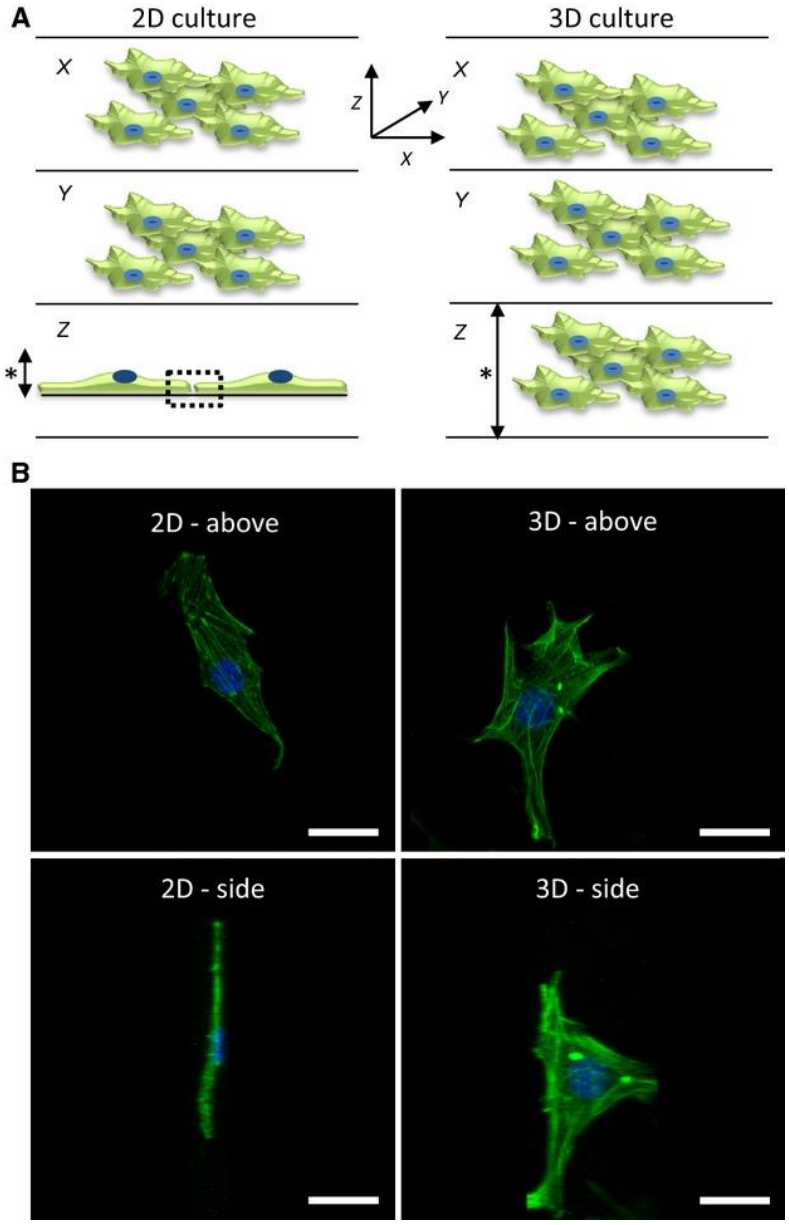

Figure 3.1.1: Impact of the physical environment on cell structure. A) Illustration of cells for each of the three dimensions (X, Y, Z); B) Confocal images of a single fibroblast grown in 2D or 3D culture. Scale bars: 10 µm. Adapted from [54].

Moreover, cells are confined to grow in 2D monolayers which forces them to establish limited cell-cell interactions compare to their real potential, since adhesion molecules and receptors are expressed all around the cell surface and not just on the bottom. This can produce unwanted effects, like enhancing proliferation and inhibiting differentiation, and loss of polarity [53, 54, 55].

In mammalian tissues, cells connect not only to each other but also to a support structure called the extracellular matrix (ECM). ECM is primarily composed of two types of macromolecules: fibrous proteins (i.e. collagens and elastin) that have the main function of defining the tissue stiffness, and glycoproteins (i.e. proteoglycans, fibronectin, and laminin) that cells use as anchorage points by mean of transmembrane receptors called integrins. Nonetheless, thinking about ECM just as merely physical support would be reductive. In fact. ECM actively participates in a whole ensemble of physiological processes that govern cell's life, like proliferation, differentiation, migration, expression of genes and proteins and so on [56].

Given this complex mechanical and biochemical interplay between a cell and its surrounding microenvironment, it is perhaps no surprise that researchers will miss biological subtleties if the cells they are studying are grown onto flat rigid plastic layers. These hints led scientists to the conclusion that cultivating cells in a three-dimensional system would be a better model for recapitulating *in vitro* a high-fidelity tissue condition [55]. A list comparing 2D and 3D cell culture features can be found in **Table 3.1.1**.

Three-dimensional cell cultures

With the term three-dimensional cell culture, it is commonly referred to cell culture platforms where the third dimension (height) is not neglected compared to the other two (length and width).

An actual 3D system help overcoming the inconsistency between cell-based assays and what is actually seen *in vivo* by: (i) allowing individual cells to maintain their normal 3D shape and structure; (ii) encouraging cells to form complex interactions with adjacent cells and the matrix;

(iii) establishing a more natural environment, for different cell types, so to foster the creation of native tissue architecture.

Using 3D cell culture technologies, scientists managed to design cell and tissue models bearing incredible similarity with an *in vivo* real situation. For example, 3D *in vitro* models of cancer epithelial cells were reported to be altered in shape and with loss of polarity, exactly like *in vivo* tumor progression [57]. Developmental biologists discovered that fibroblasts (collagen-secreting cells), in a 3D cell culture, moved and divided more quickly, and assumed the characteristic asymmetric shape that have in living tissues [58]. Outstanding step forwards were made also in biomedical fields like tissue engineering, gene therapy, and drug testing. To mention a few of them, Pradhan-Bhatt *et* al. obtained an organized human salivary gland with active protein secretion pathways *in vitro* which can potentially be used to restore salivation in patients damaged by radiation treatments [59]. Instead, researchers led by Michael Korn of the University of California, realised that only when in a 3D conformation malignant breast cells could be efficiently targeted by adenoviruses to introduce therapeutic genes [60].

It is possible to find hundreds of thousands of papers attesting the undeniable advantages of using 3D cell cultures, but despite all of these merits, traditional 2D cell culture models are still the first option that scientists turn to obtain at least preliminary results. Much work is still needed to be done indeed to make 3D cell cultures common laboratory routine practice. The reason is essentially related to all of the practical difficulties that come with the handling of such complex systems. Optimizing 3D cell cultures in terms of practicality, reproducibility, automatization, and processability will make them finally reach the highest step of the podium of cell culture techniques.

Features	2D cultures	3D cultures
Time of culture formation	Within minutes to a few hours	From a few hours to a few days
Culture quality	High performance, reproducibility, long-term culture, easy to interpret, simplicity of culture	Worse performance and reproducibility, difficult to interpret, cultures more difficult to carry out
In vivo imitation	Do not mimic the natural structure of the tissue or tumor mass	In vivo tissues and organs are in 3D form
Cells interactions	Deprived of cell-cell and cell-extracellular environment interactions, no in vivo-like microenvironment and no "niches"	Proper interactions of cell-cell and cell-extracellular environment, environmental "niches" are created
Characteristics of cells	Changed morphology and way of divisions; loss of diverse phenotype and polarity	Preserved morphology and way of divisions, diverse phenotype and polarity
Access to essential compounds	Unlimited access to oxygen, nutrients, metabolites and signalling molecules	Variable access to oxygen, nutrients, metabolites and signalling molecules
Molecular mechanisms	Changes in gene expression, mRNA splicing, topology and biochemistry of cells	Expression of genes, splicing, topology and biochemistry of cells as in vivo
Cost of maintaining a culture	Cheap, commercially available tests and the media	More expensive, more time-consuming, fewer commercially available tests

Table 3.1.1: Comparison of 2D and 3D cell cultures. Adapted from [53]

3.1.2 Scaffold-based 3D cell cultures

It is possible to distinguish two main strategies for three-dimensional cell cultures development: scaffold-based and scaffold-free methods. Since scaffold-free methods are beyond the purpose of this elaborate they will not be discussed further [61].

The word scaffold it is usually refers to materials engineered in order to provide three-dimensional physical support for cells in culture, that may resemble, as much as possible, the architecture of a specific native tissue. A scaffold is particularly required when 3D biological constructs become large in size and with complex spatial organization.
Numerous scaffold types have been produced using different materials and fabrication techniques. Typically, most scaffolds consist of polymers, ceramics, metals, or a combination of them. Considering polymers, which are by far the most used materials for this purpose, we can classify them into two big categories based on their chemical composition: those derivates from a natural source and those human-made. Among natural polymers, there are proteins (e.g. collagen and derivates, keratin, fibrinogen, silk), polysaccharides (e.g. alginate, chitosan), and glycosaminoglycans (e.g. hyaluronate). Also, synthetic polymers include a wide spectrum of candidates, like poly(ε-caprolactone) (PCL), poly(lactic acid) (PLA), poly(vinyl alcohol) (PVA), poly(glycolic acid) (PGA), and polyurethanes (PUs) [62].
Each material is characterized by positive and negative aspects. In general, natural polymers possess good biological compatibility, meaning that the engineered structure does not have a cytotoxic effect on cells, and low immunogenicity. This last point is fundamental in those applications where the scaffold has to be implanted in a host body since it must prevent the onset of a severe inflammatory response. Natural polymers are often easily biodegraded by enzymes. However, despite being a desired effect in certain situations, it might be counterproductive to have a quick degradation rate because scaffold structure will be irreversibly compromised too soon. On the other hand, the strength of synthetic polymers relies exactly on their mechanical stability. Generally, the scaffold has to reproduce the same stiffness of the native tissue and synthetic polymers can be properly tuned to meet and maintain this basic but crucial requirement over a long period of time. Unfortunately, these polymers usually lack bio-adhesiveness capabilities. Cells adhesion on the scaffold is the preliminary step enabling any further cellular function, from growth to migration, differentiation and so on, therefore, it is mandatory to improve synthetic scaffold bio-adhesiveness before their usage [63].

The last essential parameter to be severely controlled during scaffold design is its architecture. Entirely functional scaffolds should address the local cellular environment at two levels: (i) a microscale level that contains suitable cues for cell adhesion, survival, and functionality; (ii) a macroscale level that permits tissue 3D reconstruction and guarantee an adequate transport of oxygen and nutrients. Regarding this last point, there are several techniques for manufacturing 3D scaffolds with different shapes and morphologies. It is possible to subdivide them into conventional methods and rapid prototyping methods. The first class includes solvent casting, freeze-drying, and gas foaming, mainly for the production of porous scaffolds (**Figure 3.1.2A**), and electrospinning for that one of fibrous scaffolds. Whereas in the rapid prototyping category reside all the 3D printing technologies available on the market (e.g. SLA, FDM, bioprinting). This kind of methods provide the user with excellent control over design, opening the possibility to produce customized and patient-specific scaffolds. In this context, hydrogels are largely employed because of their elastic behavior and swelling capability, which makes them desired as injectable materials (**Figure 3.1.2B**) [64].

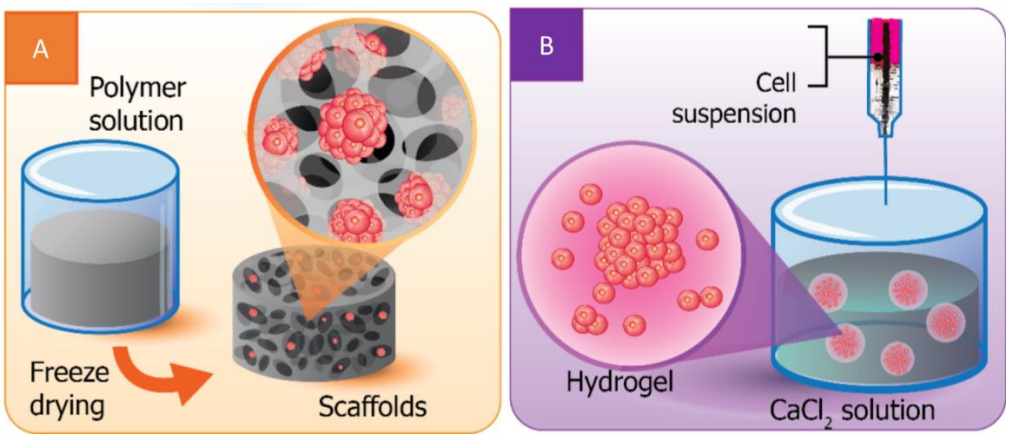

Figure 3.1.2: Scaffold-based 3D culture illustrative examples. A) A porous polymeric scaffold made by freeze-drying. B) A hydrogel scaffold made with a bioprinting machine. Adapted from [57].

3.1.3 Scaffold functionalization methods

As state in the previous chapter, often synthetic polymers are completely lacking bio-adhesiveness properties. This is due to the fact that such materials may not present recognisable moieties on their surface capable to prompt cells anchorage. Cell-substrate interactions are governed by lots of factors such as surface energy, chemical composition, stiffness, as well as roughness, and topography. Concerning just the chemistry of a material, cells generally favour adherence to surfaces that are hydrophilic or that contain functional groups such as $-NH_2$ or $-COOH$ [65].

Over the years, scientists have developed many strategies for the activation of polymer surfaces, in particular for the introduction of functional groups that can behave directly as cell recognition sites or that can be subsequently used to link bioactive macromolecules of interest. It is possible to summarise them in two main categories: bulk and surface functionalization approaches [66].

With bulk functionalization, it is referred to changes in the entire biomaterial backbone, therefore even those parts not directly exposed to cells contact. It is done by blending with the inert pre-polymer solution different monomer types bearing hydrophilic functional groups (e.g. –OH; –COOH; $–NH_2$; –SH) [67].

Surface functionalization instead, focuses on introducing functional groups only on the material surface, thus allowing to maintain unchanged its backbone. It can be further subdivided into dry and wet methods (**Figure 3.1.3**). Dry methods include physical techniques like plasma treatment and UV-ray exposure, which creates oxygen reactive species capable of interact and change surface chemistry of a polymer. Modification by physical methods is relatively simple, cost-effective, and scalable. It is also eco-friendly as it does not require the use of any additional chemicals. However, a consistent limitation of such techniques is that only surfaces directly exposed to the treatment will be efficiently activated. By consequence, for scaffolds with complex architectures (e.g. porous scaffolds or free-form scaffolds), it will be highly unlikely to uniformly activate all the surfaces, especially those shielded or hidden on the inside. Furthermore, if the treatment is

prolonged too much over time, it will compromise scaffold mechanical properties by disrupting irreparably the polymer matrix [68].

Wet methods for surface modifications involve chemical procedures where the polymer is dipped or coated/sprayed with a chemical to enhance its surface properties. The most commonly used techniques are hydrolysis and aminolysis, reactions involving the rupture of an ester bond with the formation of one hydroxy group and a carboxy or an amine group respectively. Recently, a new biomimetic strategy inspired by the mussel adhesive mechanism has also been developed (it will be deeper discussed later in the chapter). Wet methods become particularly useful in situations where conventional physical methods are ineffective, due to deep penetration of the solvent into the scaffold pores. Moreover, wet methods allow selective treatment of materials depending on their chemical composition. Drawbacks of these techniques are the requirements of additional procedures such as rinsing, washing, and drying, before further processing of the polymer, which invariably increases the amount of hazardous waste generated [66].

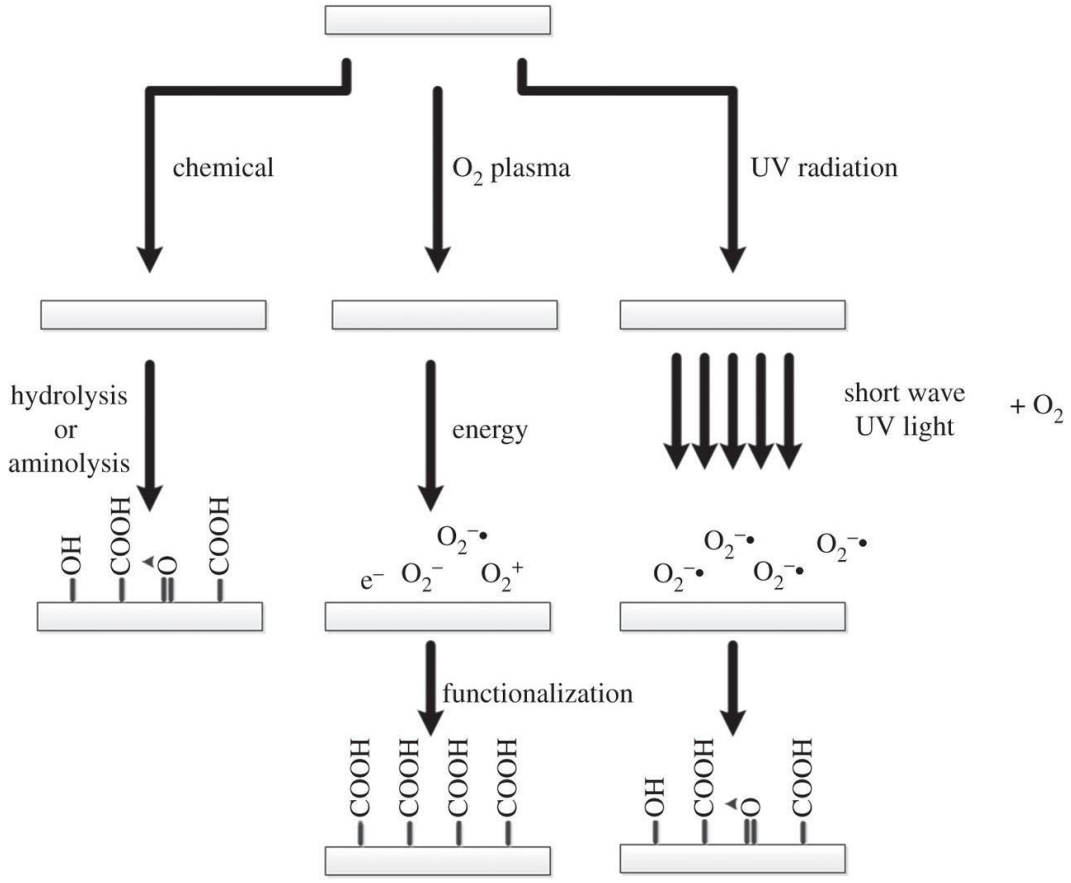

Figure 3.1.3: Schematic diagram of wet (hydrolysis and aminolysis) and dry (plasma oxygen and UV radiation) surface functionalization methods. Adapted from [65].

Usually surface chemical treatments are performed to introduce functional groups on the scaffold surface for subsequent conjugation with biomolecules carefully chosen depending on what microenvironment is being engineered in vitro. Among them there have been used several proteins (e.g. collagen, fibronectin, laminin, gelatin), short sequences of peptides (Arg-Gly-Asp - RGD sequences), polysaccharides and growth factors. These biomolecules can be linked to the scaffold surface by non-covalent (i.e. physical absorption) or covalent bonds (**Figure 3.1.4**). Non-covalent incorporation exploits the

onset of weak interactions between the biomolecules and the functional groups present o the polymer surface (i.e. electrostatic forces, hydrophobic interactions, and hydrogen bonds). It can be applied having the disadvantage of generating a short-term stability coating. Covalent incorporation, instead, results in an efficient coating, with biomolecules being retained over a longer period of time when compared with physical adsorption. However, it always requires prior activation of functional groups on both polymer surface and on biomolecules and, quite often, the usage of linker molecules.

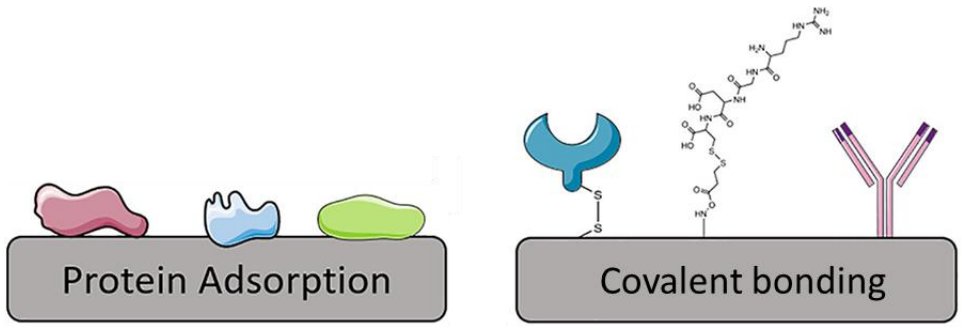

Figure 3.1.4: Illustration of molecules adsorbed (left) and covalently bounded (right) to a substrate surface. Adapted from [67].

Polydopamine coating: a mussels-inspired adhesiveness

Mussels, bivalve molluscs from saltwater, possess an outstanding capability of staying attached to virtually all types of inorganic and organic surfaces. Studies demonstrated that this may lie in the amino acid composition of proteins found near the plaque-substrate interface, which are rich in 3,4-dihydroxy-L-phenylalanine (DOPA) and lysine amino acids.

By taking inspiration from mussels' adhesive mechanism, in 2007, Lee and co-workers developed a brilliant and easy wet functionalization method to activate the surface of a wide variety of polymers, independently from their chemical composition [69].

These researchers identify dopamine, a well-known catecholamine present in the human body, as a readily available small molecule

possessing both of the functional moieties (DOPA and lysine) present in the mussel adhesive proteins. They discovered that by simply submerging a substrate in an aqueous solution of dopamine, buffered to a pH typical of marine environments (10 mM Tris, pH 8.5), it resulted in the deposition of a thin black-coloured polydopamine layer all over the surface (**Figure 3.1.5A**). The strong binding affinity between the newly formed layer and the polymeric surfaces is expected to be governed by weak interactions among different functional groups present on both chemical species, but the exact adhesive molecular mechanism still remains to be elucidated [70].

A polydopamine coat is already by itself capable of largely improving surface hydrophilicity and this is, in theory, and in practice, already enough to favour cell adherence. Nevertheless, to create a more refined cellular environment, polydopamine layer can be further used as a starting point for secondary conjugations with other active biomolecules, since it contains extremely reactive catechol groups. Molecules bearing nucleophilic functional groups, such as amines and thiols, were shown to react with catechols through Michael addition or Schiff base reactions.[71]. For this reason, polydopamine has been extensively utilised basically as a "double-sided adhesive tape" to link onto substrate surfaces lots of different ECM molecules, such as collagen, fibronectin, laminin, heparin sulphate, and hyaluronic acid (**Figure 3.1.5B**) [70].

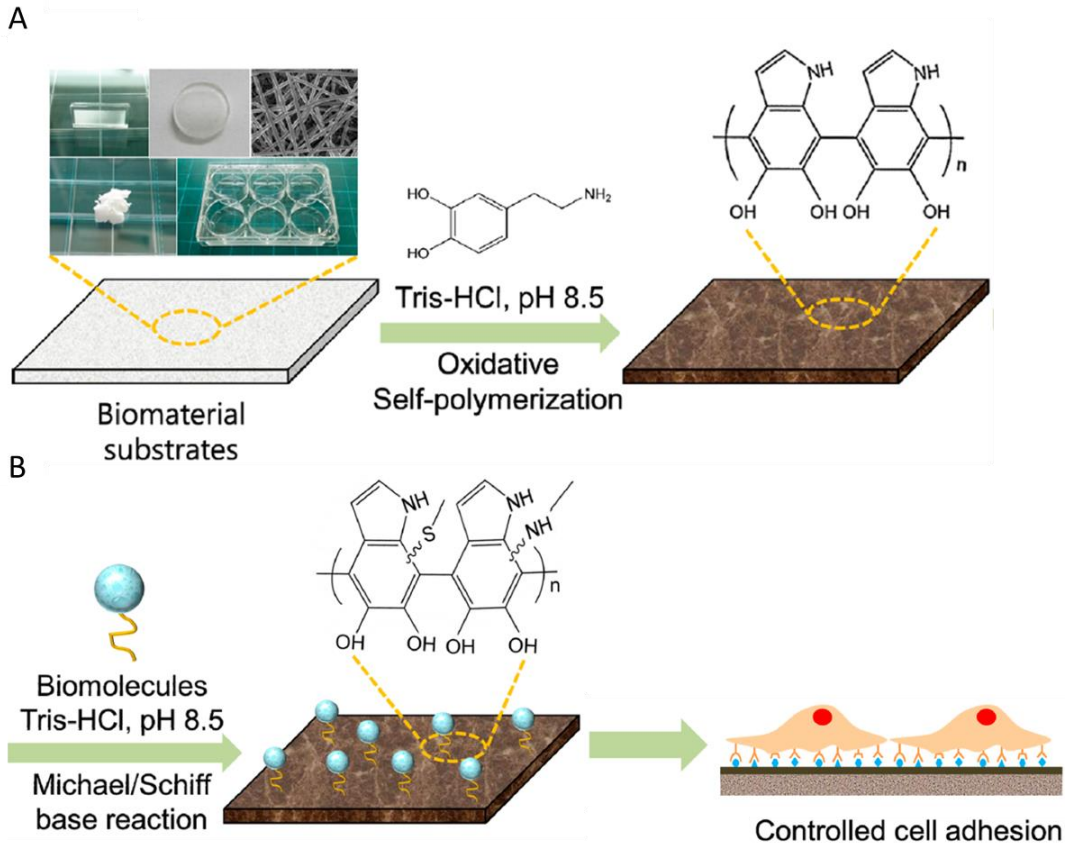

Figure 3.1.5: Schematic representation of polydopamine coating protocol. A) Several different substrates can be coated with polydopamine through self-polymerization of dopamine, using a slightly basic (pH = 8.5) buffer (Tris-HCl); B) Biomolecules can then be covalently immobilized onto these surfaces enabling cells adhesion. Adapted from [70]

3.1.4 Increasing mass transport into scaffolds

Once designed, synthesized and properly functionalized, a scaffold is ready to be used to host a desired *in vitro* 3D cell culture. However, to seed the living component of the culture (i.e. cells) and to maintain it alive in a 3D scaffold, it is necessary to made use of an external mechatronic apparatus, namely a bioreactor. With the term bioreactor, in tissue engineering, it is generally referred to powerful technical tools to

support and direct the *in vitro* development of living, functional tissues, under closely monitored and tightly controlled environmental and operating conditions [72].

A high initial cell number is always desirable to successfully mimic *in vivo* tissue cellular density (which in the human body is in the order of 10^9 cells/ml). [73]. Seeding cells into a scaffold at high initial densities it has been associated with enhanced tissue formation, including higher rates of cartilage matrix production, increased bone mineralization, and enhanced cardiac tissue structure [74]. Traditionally, the delivery of a cell suspension over a 2D flat substrate (like a petri dish or a flask) is manually performed by means of pipettes. Cells spreading and settlement on the bottom of the container just relies on gravity and mixing as propagating forces. This "static" seeding method, besides being intrinsically scarcely reproducible due to marked intra- and inter-operator variability, usually yields inhomogeneous and poor coverage of 3D scaffold surfaces. The reason is that gravity is not sufficient by itself for cells to penetrate throughout the entire scaffold architecture, most evidently in those with particularly tortuous morphologies (e.g. porous scaffolds), and because mixing it is simply not possible to be performed [72], [75].

Significantly higher efficiencies and uniformities can be obtained by automatically flowing a cell suspension directly through scaffold pores and walls, utilizing perfusion bioreactors. A common perfusion bioreactor it is composed of a fluidic pump for pushing the medium from a reservoir through the scaffold and a computer that enables the user to configure fluidic parameters like the flow rate, the volume to be dispensed, the directionality of the flow, and many other. Sometimes the cultivation chamber is also provided with microsensors (e.g. oxygen sensors) that not only allow real-time monitoring but also activate feedback loops to adjust culture values dropping out of a determined physiological range (**Figure 3.1.6**) [76].

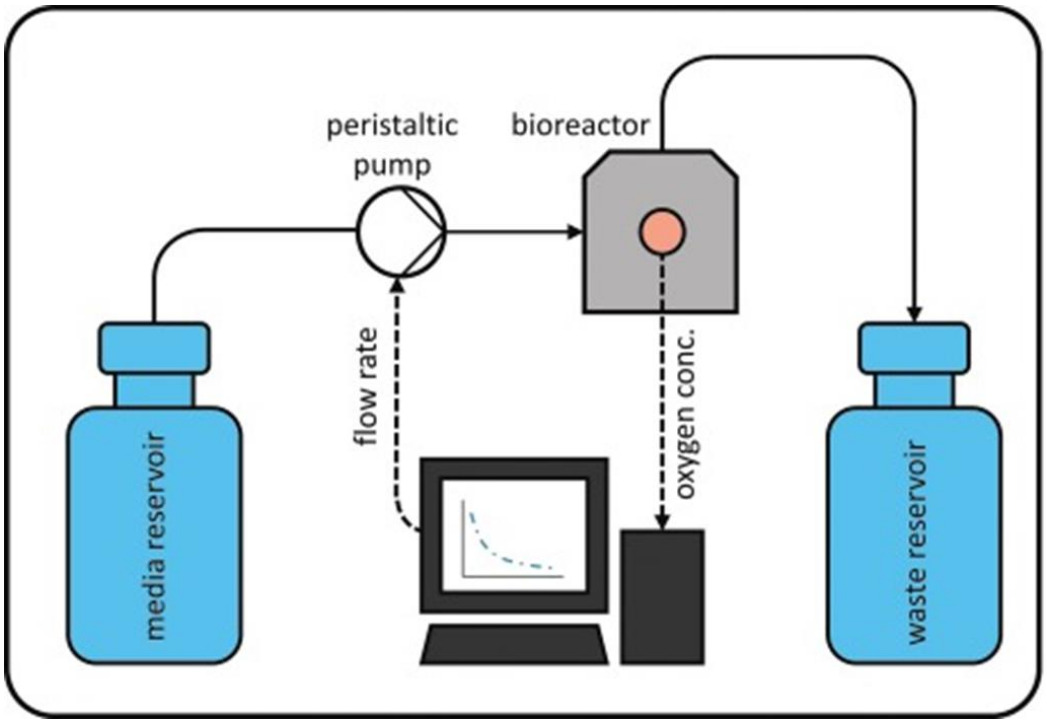

Figure 3.1.6: Process flow diagram of a common perfusion bioreactor. Adapted from [76]

An efficient cell seeding is just the first step in establishing a 3D culture, the hardest part is actually to keep cells alive for its entire duration. As a matter of fact, the supply of oxygen and of soluble nutrients becomes critically limiting in culturing 3D tissues. In bi-dimensional cell cultures, oxygen and nutrients dissolved in the medium arrive at the cell bed just by diffusional transport. This is compatible with cells life because the time required by the molecules to travel the length scale into play, that is the height of the medium layer (usually just one or two mm thick) above the single 2D cell sheet, is short enough. In other words, oxygen and nutrients are being delivered at a rate faster than their consumption [74]. Unfortunately, this condition does not hold true in 3D tissues because of dimensional scale-up, and diffusion by itself is not anymore a sufficiently fast transport method to sustain cells' life. As a matter of fact, it has been well proven that, in static conditions, in cell constructs

higher than 100 μm only the outer layer of the tissue construct remains completely viable, whereas the interior becomes necrotic because of hypoxia [77].
Nature has addressed the problem by establishing a complex vascular network within which blood full of oxygen and nutrients circulates and arrive all over the body. It is quite outstanding thinking that the maximum distance *in vivo* of a cell from its nearest capillary rarely exceeds 200 μm and is usually less than 100 μm [78]. It is therefore not surprising that an alternative solution needs to be found if we want to make cells seeded in a macroscopic construct to feel physiological oxygen concentration levels for the entire culture duration. Once again, perfusion bioreactors can be readily used to full fill such need, by directing medium perfusion throughout the culture. With an active flow transport it is indeed possible to overcome diffusional transport limitations and to supply cells of oxygen and metabolites within a life-compatible time window [79].

3.1.5 Anatomy and physiology of the skeletal muscle tissue

The skeletal muscle, along with cardiac and smooth muscle, is responsible for motion generation within organs, blood, and of the body as a whole. It is primarily composed of cells, called muscle fibers, which are specialised in doing one specific job: contraction.
Muscles fibers are cylindrical multinucleated cells with diameters of 10-100 μm and long even a few centimetres. They originate from mesenchymal cells called myoblasts that start to align and fuse together to form myotubes. Myotubes then, continue differentiating into functional muscle fibers by synthesizing the proteins necessary to make up the contractile apparatus and by displacing their nuclei against the sarcolemma (**Figure 3.1.7A**).
When longitudinally sectioned, fully mature myofibers show striations of alternating light and dark bands. Their sarcoplasm is indeed highly organized in long cylindrical filament bundles called myofibrils that run parallel to the long axis of the cell. The repetitive arrangement of

myofibrils structure is the minimal functional unit of the contractile apparatus, and it is called sarcomere. The sarcomere is composed mainly of two types of myofilaments, actin (the thin filament) and myosin (the thick filament) (**Figure 3.1.7B**) [80].

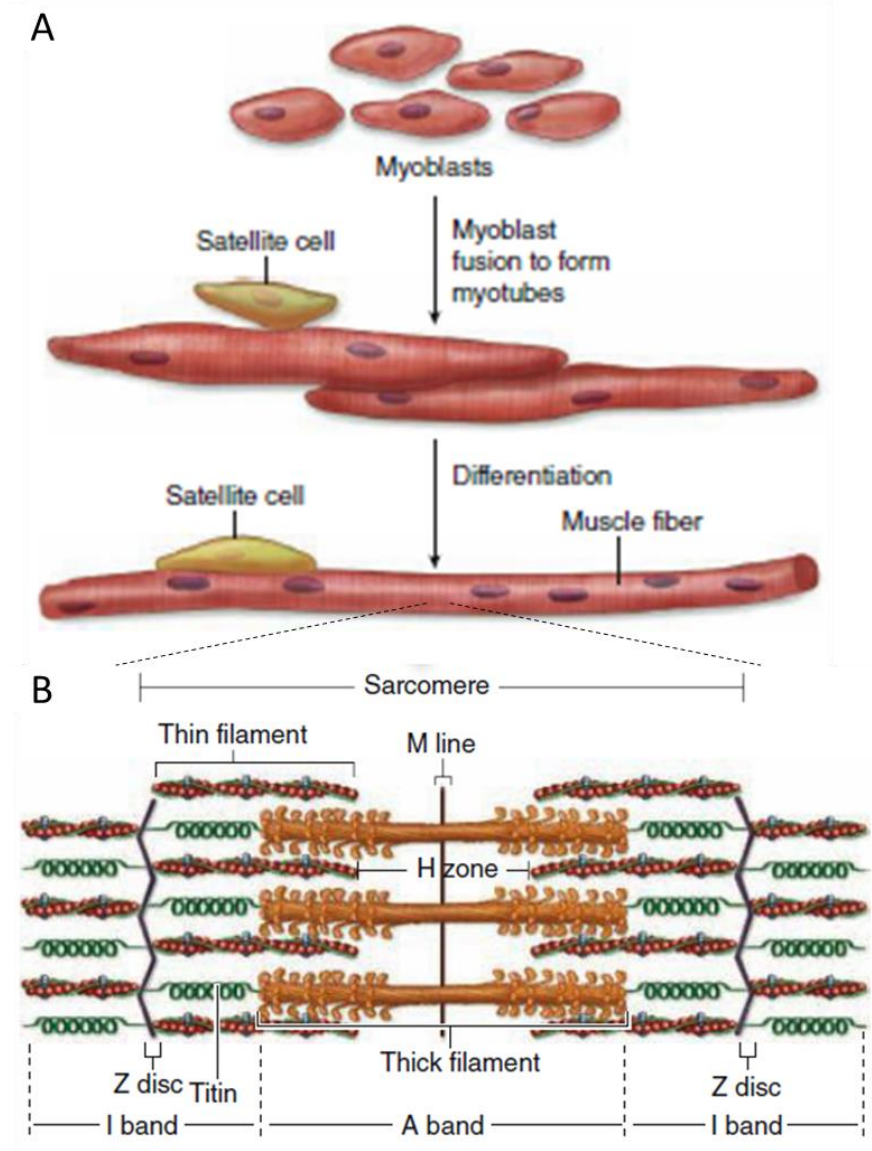

Figure 3.1.7: A) Skeletal muscle begins to differentiate when mesenchymal cells, called myoblasts, align and fuse together to make longer, multinucleated tubes called myotubes; B) Thin filaments are actin filaments with one end bound to

α-actinin in the Z disc. Thick filaments are bundles of myosin, which span the entire A band and are bound to proteins of the M line and to the Z disc across the I bands by a very large protein called titin, which has springlike domains. Adapted from [80].

The skeletal muscle niche

Part of the myoblast population does not fuse and differentiate, but instead remains as a group of mesenchymal cells called muscle satellite cells located on the external surface of muscle fibers inside the developing external lamina. Satellite cells are now considered the most important myogenic progenitors and are involved in the postnatal growth and regeneration of muscle fibers, but they have poor migratory capabilities and do not possess the ability to cross the endothelial cells of the blood vessels. More recently two new sources of myogenic precursors have been discovered: mesangioblasts and pericytes. These two cell populations are multipotent staminal cells associated with blood vessels, which can differentiate into myoblasts or satellite cells, can supply pro-angiogenic factors for new blood vessels formation, and have also good capacity to cross the endothelial [81].

The skeletal muscle ECM has a hierarchical organization and enwrap smaller and smaller portions of the muscle moving radially from the outside to the inside: (i) the epimysium surrounds the whole muscle carrying large nerves, blood, and lymphatic vessels; (ii) the perimysium surrounds groups of muscle cells (i.e. fascicle) that makes up a functional unit in which the muscle fibers work together; (iii) the endomysium surrounds the external lamina of individual muscle fibers and is rich of little nerve fibers and capillaries (**Figure 3.1.8**) [82].

As for the vast majority of cell types and tissues, the inner ECM coating, directly in contact with the muscle fibers sarcolemma, is the basal lamina (BL). The BL composition generally comprises non-fibrillar collagen, glycoproteins, and proteoglycans with percentages that vary from tissue to tissue. Specifically, the skeletal muscle BL is rich in collagen IV and laminin to provides significant tensile strength and stress resistance to the entire muscle tissue. Laminin is also important to activate survival signaling critical for myoblasts proliferation, to stimulate their motility,

and to make them assume the bipolar shape characteristic of fusing cells. In contrast, fibronectin, which can also be found abundantly in skeletal muscle BL, selectively promotes dedifferentiation of myoblasts [83].

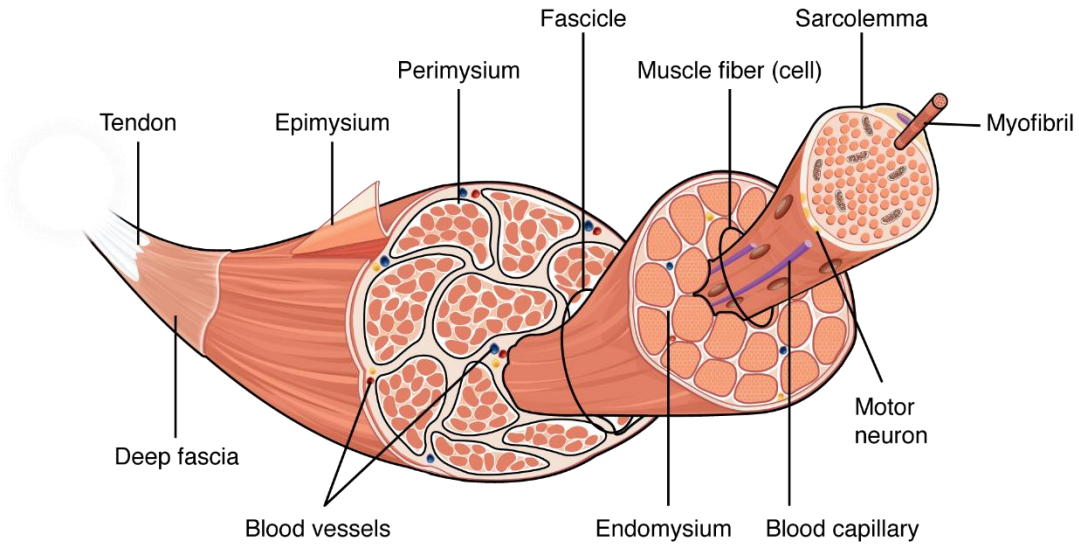

Figure 3.1.8: Illustration of the skeletal muscle tissue architecture.

Contraction mechanism

Excitation-contraction coupling is the coordination of two processes that are required for the generation of muscle force.

The initial stimulus is an action potential coming from a motor neuron axon through a particular synapse called the neuromuscular junction (NMJ) that terminates in the proximity of a muscle fiber (**Figure 3.1.9**). When the action potential reaches the NMJ it triggers the release of a neurotransmitter, acetylcholine, which binds its specific receptor present on the sarcolemma of the muscle fiber. This ligand-receptor interaction generates a second action potential that, this time, propagates towards a system of membranous tubes, called transverse tubules, until it reaches the terminal cisternae of the sarcoplasmic reticulum. Here, voltage-dependent receptors open up and allow an intra-cytoplasmatic current of calcium. Finally, Ca^{2+} ions release in the sarcoplasm prompts the activation of the molecular contractile machinery, by enabling actin and

myosin myofilaments to slide past one another, causing sarcomere shortening [84].
Muscle contraction is therefore the result of a series of coordinated intracellular modifications that leads to a concerted movement of all the muscle fibers and, consequently, of the whole muscle.

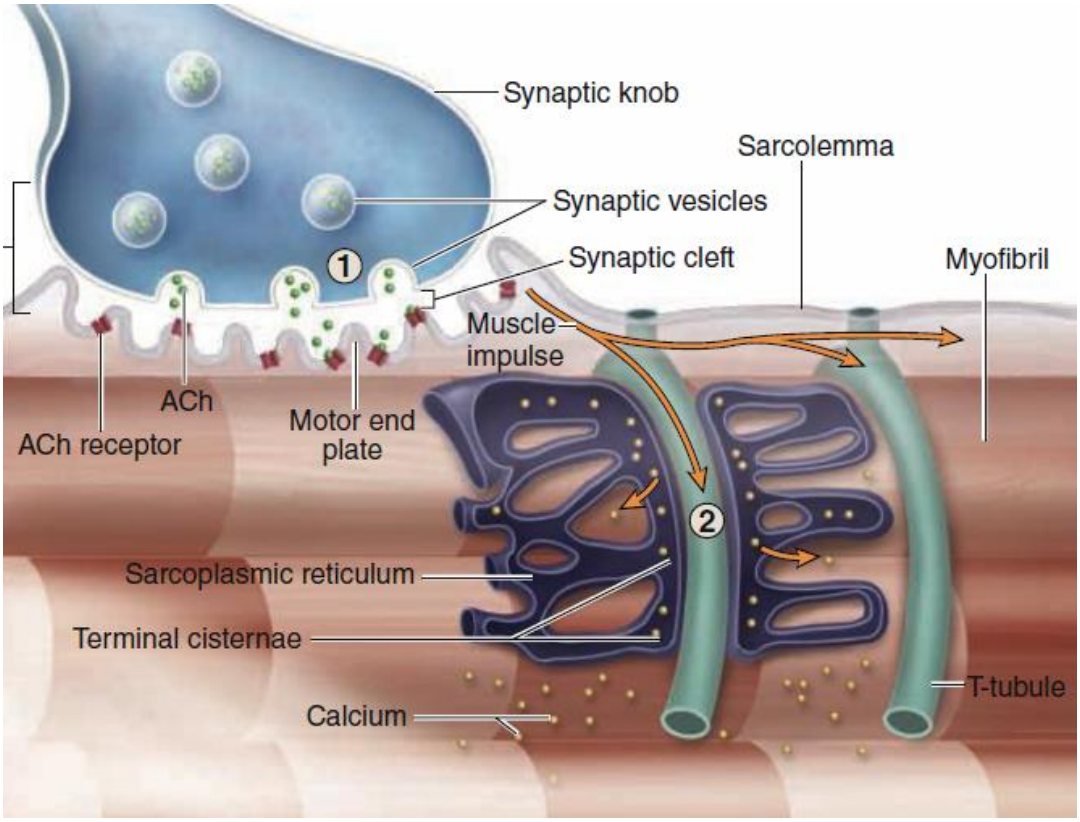

Figure 3.1.9: Illustration of the neuromuscular junction. Adapted from [80].

3.1.6 Skeletal muscle 3D constructs

Skeletal muscle Tissue engineering

Tissue engineering is a discipline that uses a combination of cells, materials and engineering methods, to restore, maintain, and replace a

biological tissue *in vitro* (**Figure 3.1.10**). The branch of tissue engineering dealing with skeletal muscle reconstruction is called: skeletal muscle tissue engineering (SMTE).

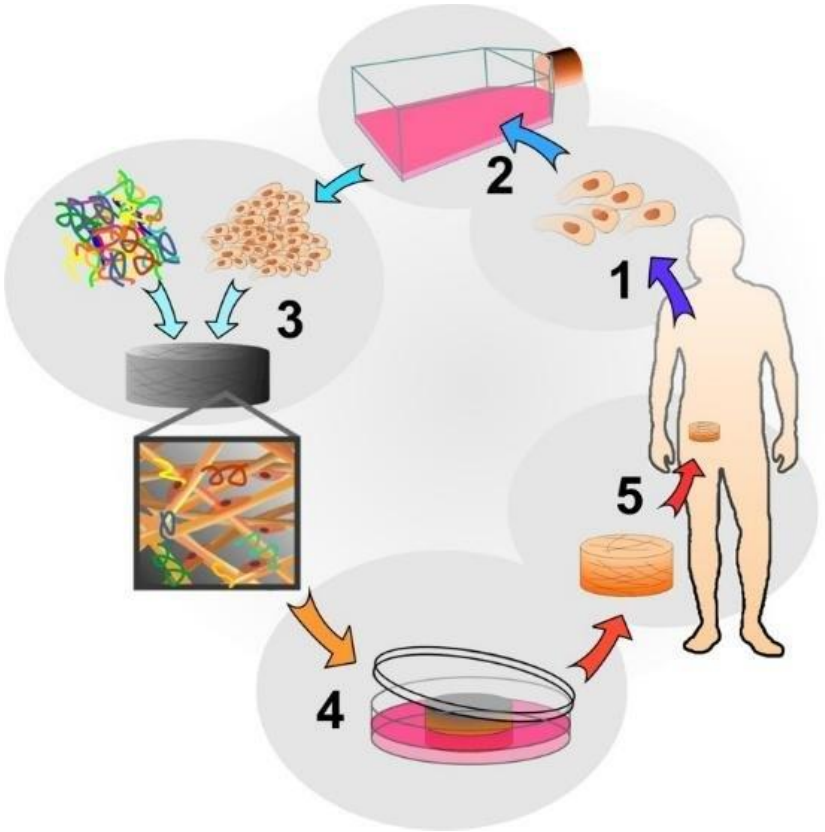

Figure 3.1.10: The classical Tissue Engineering paradigm: 1. Identification and harvesting of cells from the patient; 2. Cellular proliferation in vitro; 3. Association of the cells to a scaffold as well as addition of suitable growth factors; 4. Expansion of the 3D construct with the potential help of a bioreactor system; 5. Implantation of the functional biological construct into the patient.

Lesions so extensive that strongly impair muscle functionality are commonly referred to as volumetric muscle losses (VMLs). The main causes of VMLs are due to traumatic injury and surgical resection of tumors. SMTE has seen a rapid development in the last decade, facilitated by the growing understanding of the processes underlying the

regeneration of this tissue, and for this reason, bear the potential of becoming the gold standard therapeutic approach to restore considerable muscle loss in patients. However, as of now, SMTE constructs are either intended as *in vitro* skeletal muscle disease models or as *in vivo* pre-clinical research tools and numerous hurdles have to be overcome before they will have an actual use in clinical settings [85].

The reality is that the skeletal muscle is a highly complex tissue, in terms of cellular population, spatial organization, and physiology, and despite our knowledge on reproducing a mature three-dimensional skeletal muscle tissue *in vitro* is continuously rising by the day, several variables remain to be uncovered. In this chapter, will be highlighted some of the main challenges, as well as missing pieces, that scientists commonly encounter in dealing with SMTE.

Supplies and neighbourhood

The skeletal muscle tissue is one of the most high-demanding tissue in terms of oxygen and metabolites rate supply, a condition that is even further aggravated under physical exercise [86]. As already stated, the human body relies on blood active transport to sustain muscle fibers' life and activity. Therefore, in *in vitro* 3D cultures, is mandatory to find a substitute pumping system to have a full health and non-hypoxic macroscopic construct. In the context of SMTE, one deeply explored strategy is the usage of perfusion bioreactors in concomitance with porous scaffolds, and in particular of porous polyurethane (PU) scaffolds [87].

PUs are a class of polymeric materials that represent an optimal candidate for the fabrication of a muscle-like architecture and microenvironment, because of the possibility of tuning several features like porosity, stiffness, and surface chemistry. In fact, a high porosity degree ensures an optimal perfusion ability through the whole scaffold, which in turn guarantees an efficient distribution of oxygen and nutrients, as well as waste products removal. PU foams can also be engineered to have a stiffness comparable to that one of the native muscle tissue (around 10 kPa). Such property is important to avoid generating substrate-induced stress on the cultured myofibers. Finally,

porous PUs can even be functionalized with chemical methods to graft on their surface ECM proteins typical of those found in the muscle basal lamina (e.g. collagen IV, laminin, fibronectin), thus greatly enhancing the bioadhesiveness of the scaffold [88].

In the human body, there is not a single tissue composed of just one cell type. This holds true also for the skeletal muscle tissue which possesses a very heterogeneous population of cells, including fibroblasts, endothelial cells, neurons, stem cells, each one with a specific irreplaceable function (**Figure 3.1.11**). Despite this fact, most of the muscle 3D cultures reported in the literature are almost always made of just myocytes (either cell lines or primary cultures), which strongly unpair cell heterotypic communication saw *in vivo*. Few studies, however, have shown that a higher degree of muscle cells differentiation and myotubes maturation is obtained when myocytes are co-cultured with their native neighbor cells [89].

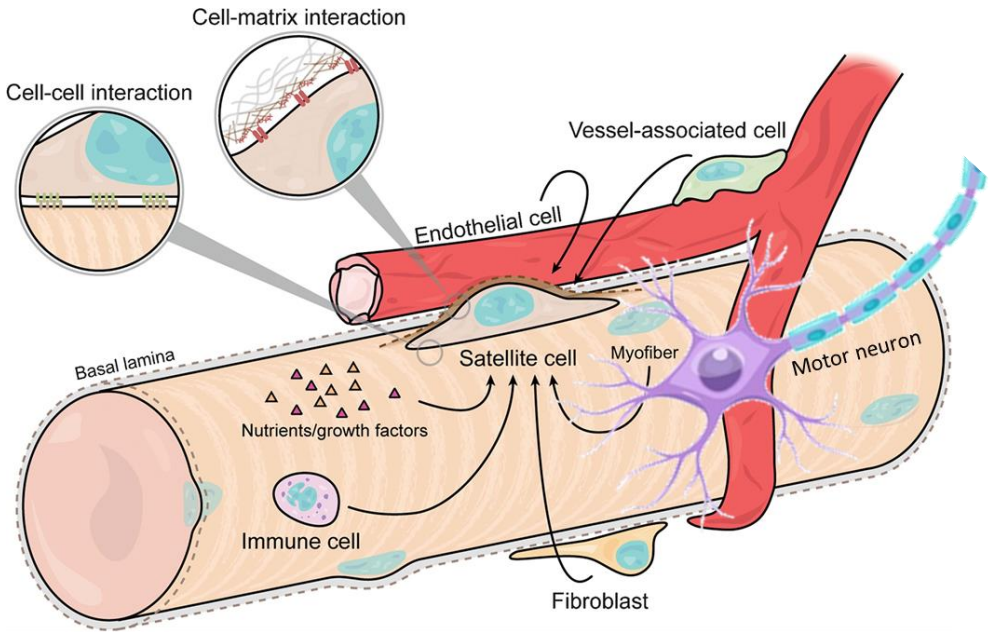

Figure 3.1.11: Representation of the skeletal muscle cell niche. Adapted from [90].

Fostering myoblast differentiation *in vitro*

Myofibers of a physiological skeletal muscle are always perfectly aligned in one direction, they are thick and long and, most importantly, well-differentiated. Their differentiation *in vivo* is achieved by the activation of complex transcriptional regulatory networks, that ultimately result in the expression of genes required to generate the contractile machinery proteins structured into sarcomeres [81]. To reach the same level of organization and performance *in vitro*, 3D muscle cell constructs have to be conditioned with several external stimuli. It is possible to summarize them in three main categories: (i) biochemical; (ii) mechanical; (iii) electrical. [91]

Biochemical stimuli include growth factors and chemicals that are provided to muscle cell cultures through their growth medium. For instance, fetal bovine serum (FBS) contains numerous components, including proteins, lipids, hormones, and enzymes, that allow myoblasts' efficient proliferation. Myogenic differentiation can be initiated employing a growth medium characterized by a lower serum percentage or by a serum with fewer growth factors, like horse serum (HS). The reduced number of serum-derived mitogens permits myoblasts to permanently exit from the cell cycle and eventually differentiate and fuse to form multinucleated myotubes [92].

Controlling myotubes' alignment and distribution in a specific direction is fundamental to form a compact tissue and to produce a directional contractile force. During the years, lots of different custom-made mechanical stimulators and stimulation protocols (including static, cyclic and ramp strain stretching) for muscle cells have been developed (**Figure 3.1.12**). Uniaxial mechanical strain has been demonstrated to help in the formation of dense and oriented muscle fibers, most probably because it mimics the physiological tensions that bones applied to muscles during longitudinal growth [93]. However, more efficient results were obtained with cyclic stimulation. Studies applying stretching between 6.7 and 20%, with frequencies of 0.1-1 Hz and for a duration between 30 minutes and 10 days, manifested an increase in myofibers length diameter, protein expression, and contractility when compared to the static control [91, 94.]

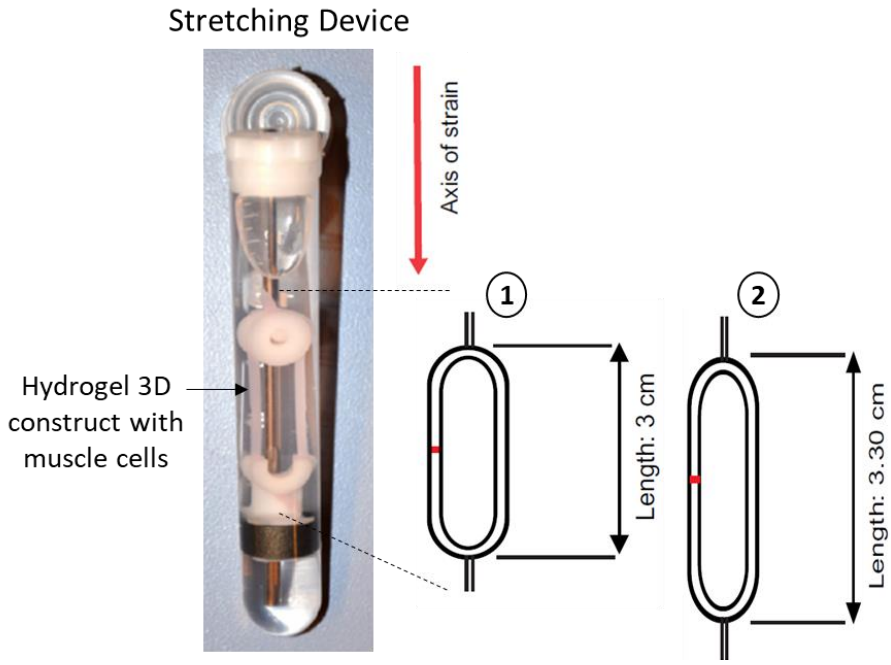

Figure 3.1.12: A custom-made stretcher device capable of elongating a 3D hydrogel-based muscle cell construct. Adapted from [93].

Electrical impulse stimulation from the central nervous system via the motor neurons is the most important physical cue for skeletal muscle development and maturation *in vivo*. Denervation of mature skeletal muscle results in fact in gradual loss of tissue mass (atrophy) and impairment of functional properties. External electrical stimuli used in skeletal muscle 3D constructs aim to reproduce the process of innervation realized by the motor neurons. Usually, to this purpose, two configurations are used in the laboratory: direct current (DC), which favour cell orientation, alters cell morphology, and directs cell migration, and alternating current (AC) fields that, on the other hand, enhances cell differentiation and increases tissue functionality. AC devices can be either capacitively coupled (electrodes not in direct contact with medium) or directly coupled (electrodes in direct contact with medium) (**Figure 3.1.13**) [95]. The physiological range for the applied current is between nA and mA and between mV and V for the electrical

potential [91]. Works on myoblast electrical stimulation-induced differentiation have been published abundantly and demonstrated the possibility to improve myogenic differentiation, increase protein expression and contractile properties compared to unstimulated controls [96 97].

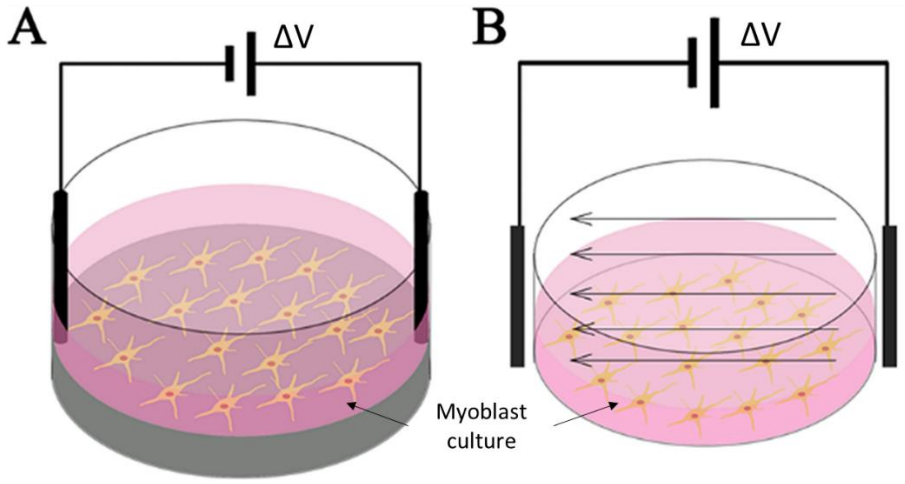

Figure 3.1.13: Two ways to deliver electrical stimulation: A) Direct coupling set-up. Electrodes are placed inside the cell chamber and are in contact with cell medium; B) Capacitively coupled set-up. Electrodes generate an electric field in-between without direct contact with the cell culture. Adapted from [98].

Muscle cells-actuated devices

In the last two decades, researchers have turned specific attention to SMTE not only because of its obvious impact in modern regenerative medicine but also because of its close implication with another promising emerging field: bio-hybrid soft robotics.

Bio-hybrid soft robots are composed of living matter capable of producing any sort of force (e.g. skeletal muscle cells, cardiomyocytes, flagellated bacteria, cilia) and soft synthetic matter as supporting structures [99]. In this elaborate, reference will be made only to bio-hybrid machines directly powered by muscle cells.

Muscle cell-based bio-hybrid actuators can be developed through a top-down or a bottom-up engineering approach in order to integrate muscle

cells within the synthetic substrate. In the case of a top-down approach, explanted mature muscles are directly coupled with the robot body. The first example of such devices was reported in 2004. Hugh Herr and Robert Dennis develop a swimming robot actuated by two explanted frog semitendinosus muscles able to perform basic swimming maneuvers such as starting, stopping, turning, and straight-line swimming for a total of almost five hours (**Figure 3.1.14**) [100]. After this pioneering work, many studies have been conducted using explanted muscles, to mimic other actuation mechanisms like walking and pumping [101].

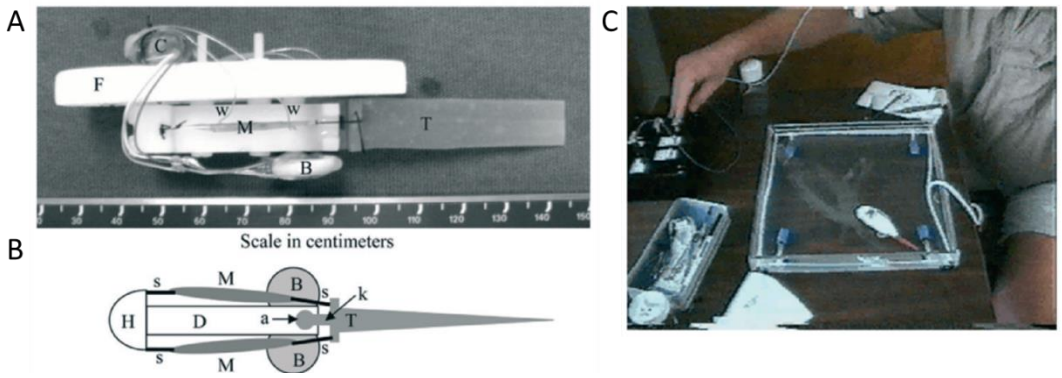

Figure 3.1.14: First-ever designed bio-hybrid robot: A) Photograph of the device (side view). B) Schematic illustration of the device (top view). Main components of the system: semitendinosus muscles (M), suture attachments (S), styrofoam float (F), electrode wires (w), silicone tail (T), lithium batteries (B), encapsulated microcontroller, infra-red sensor, and stimulator unit (C). C) Test swimming platform. Adapted from [100]

However, the issue of maintaining muscle fibers functionality *ex vivo*, constraints in actuator dimensioning and design, along with the controversial ethics of sacrificing animals to this purpose, were too much of detrimental drawbacks, such that, nowadays, this top-down approach has been completely abandoned.

The need of finding a new strategy in designing bio-hybrid robots paved the way to a series of studies where such machines were built by using a bottom-up approach (**Figure 3.1.15**). In this case, single muscle cells,

derived from commercially available cell lines or primary cell cultures, are assembled in a higher-order structure on the basis of the robot shape and purpose. With this more versatile methodology, in the last years, many outstanding muscle-cell-powered robots were produced, including walking robots [102], jellyfish-like [103] and ray-like swimmers [104], biomimetic grippers [105].

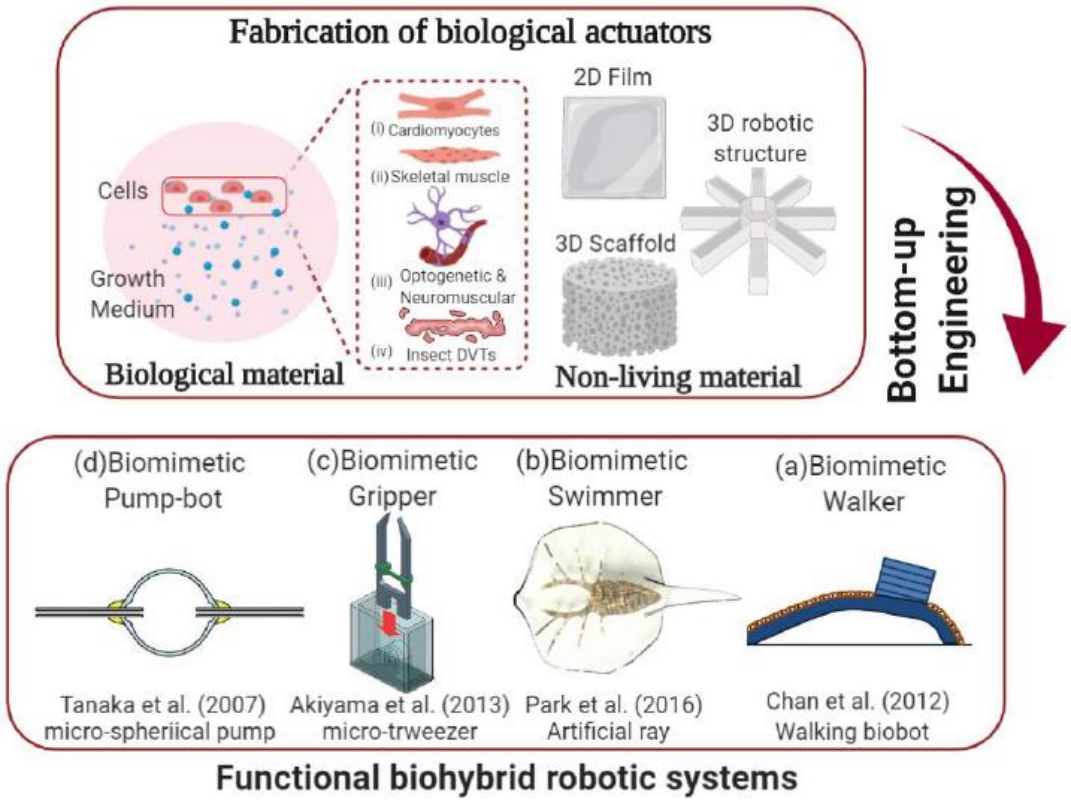

Figure 3.1.15: Bottom-up fabrication approach of bio-hybrid actuators powered by muscles cells with functional examples. Adapted from [101]

Among the innumerable advantages deriving from adopting a bio-hybrid soft robot compared to artificial micro-actuators, there are: (i) high power/weight ratio (i.e. engine's power output divided by the total mass of the machine) since no heavy external energy source is required; (ii) high transduction efficiency (i.e. effectiveness of a machine in

transforming the input energy into output energy); (iii) environmental compatibility of the fuel-work conversion products (i.e. CO_2 and metabolites); (iv) softness degree comparable with that one of soft biological tissues (Young's moduli between 10^4 and10^9 Pa); (v) self-healing capability (the muscle potential lifespan *in vivo* is of many decades) [106].

Having this said, it is quite clear why researchers are employing so many efforts and resources in improving this kind of technology. Possible concrete mid-term applications of bio-hybrid actuators are specialized platforms for investigating agonistic-antagonistic muscle contractions, proof of concepts of miniaturized therapeutic robots and implantable, reconfigurable bio-hybrid medical devices [99]. However, current bio-hybrid solutions are not really competitive with artificial actuators and are rather far from natural muscle, in terms of overall performance. As a matter of fact, engineering mature skeletal muscle fibers starting from myoblasts is a challenging task and the same problematics encountered in SMTE are in fact translated straightforward also when it comes to engineer muscle cell-based machines. It is noted especially about: maximizing cell adhesion on the synthetic scaffold of choice, providing sufficient concentration of oxygen and metabolites to cells, fostering myoblasts differentiation into muscle fibers.

Furthermore, there are other supplementary issues related just to the field of bio-hybrid soft robotics that still need to be addressed or, at least, properly ameliorated. First of all, force amplitude output. The contractile capacity of the engineer skeletal muscle tissue needs to be strong enough to displace the robot body in accordance with its task (e.g. swim, grip, walk, push, press, stretch). In other words, the elastic force necessary for substrate deformation must be calculated and designed appropriately to be less than the contractile force of muscles and this is a challenging task if we think that most of these bio-machines generate forces in the order of μN. Secondly, mammalian muscle cells typically remain viable and functional only for a few hours outside of a biological incubator, because they are subjected to varying temperature, CO_2, and pH levels, as well as to possible contaminations by microbial agents, that inevitably shorten their life. This paves the question of building a life-sustaining system for the living component of the bio-hybrid robots without

hampering the overall actuator contraction efficiency. Unfortunately, no papers on this topic have been described so far. Lastly, there is the issue of controllability of the actuator. Contraction of most bio-hybrid actuators is controlled using electrical pulses or with more sophisticated light-based stimulation systems (i.e. optogenetics) that are capable of depolarizing myotubes membrane and starting the action potential. In either case, an external power source (such as a battery) to generate triggering signals is required and although this is acceptable for application at large scales, the same does not apply for smaller and autonomous bio-actuators where dimensions are required to be constrained at the submillimeter scale [77, 107].

3.2 Aim of the Project

This research project takes place in ongoing collaboration among CIMaINa (Interdisciplinary Centre for Nanostructured Materials and Interfaces; University of Milano), The BioRobotics Institute (Sant'Anna School of Advanced Studies; Pisa), and Tensive (s.r.l. – Milan).
The aim of the project foresees the development of a macroscopic three-dimensional skeletal muscle tissue construct, in a completely all-soft and self-standing polymeric device. The synthetic matter is composed of two silicon tendon-like structures connected to a macroporous polyurethane (PU) wrapped in a thin and transparent silicone membrane (namely shell). This device was designed to mimic the morphology of a tendon-muscle-tendon (TMT) system.

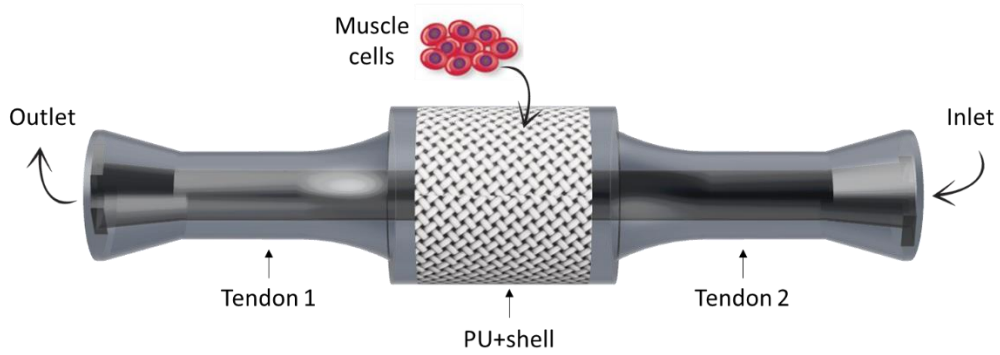

Figure 3.2.1: TMT device illustration.

3.3 Results & Discussions

3.3.1 Polyurethane scaffold characterization

Physico-chemical properties

The polyurethane scaffold is the core of the TMT device as it is intended to host skeletal muscle cells inside its structure (**Figure 3.3.1A**). Using a combination of scanning electron microscopy (SEM) and micro-computed tomography (μCT) techniques it has been possible to elucidate in detail foam architecture at both qualitative and quantitative level. In particular, from SEM images (**Figure 3.3.1C**), a clear distinction between cavities and pores was observed. Cavities are larger sub-structures with diameters of few millimetres whose surface is stud with smaller holes, the pores. The internal walls of cavities (i.e. trabeculae) appear very smooth and neat (**Figure 3.3.1D**) and provide a wide area that cells can exploit for adhesion on the scaffold. Pores, on the other hand, enables fluid perfusion throughout the whole structure. In this context, microtomography analysis (**Figure 3.3.1B**) gave valuable information on overall porosity (93.5 %) and pore's diameter (637.0 ± 188.7 μm), parameters particularly important to know in view of cell suspension administration in the scaffold during the seeding procedure and also to predict medium flow velocity and distribution during dynamic cell culturing.

Other data further elucidating scaffold morphology extracted from the μCT files are summarized in **Table 3.3.1**.

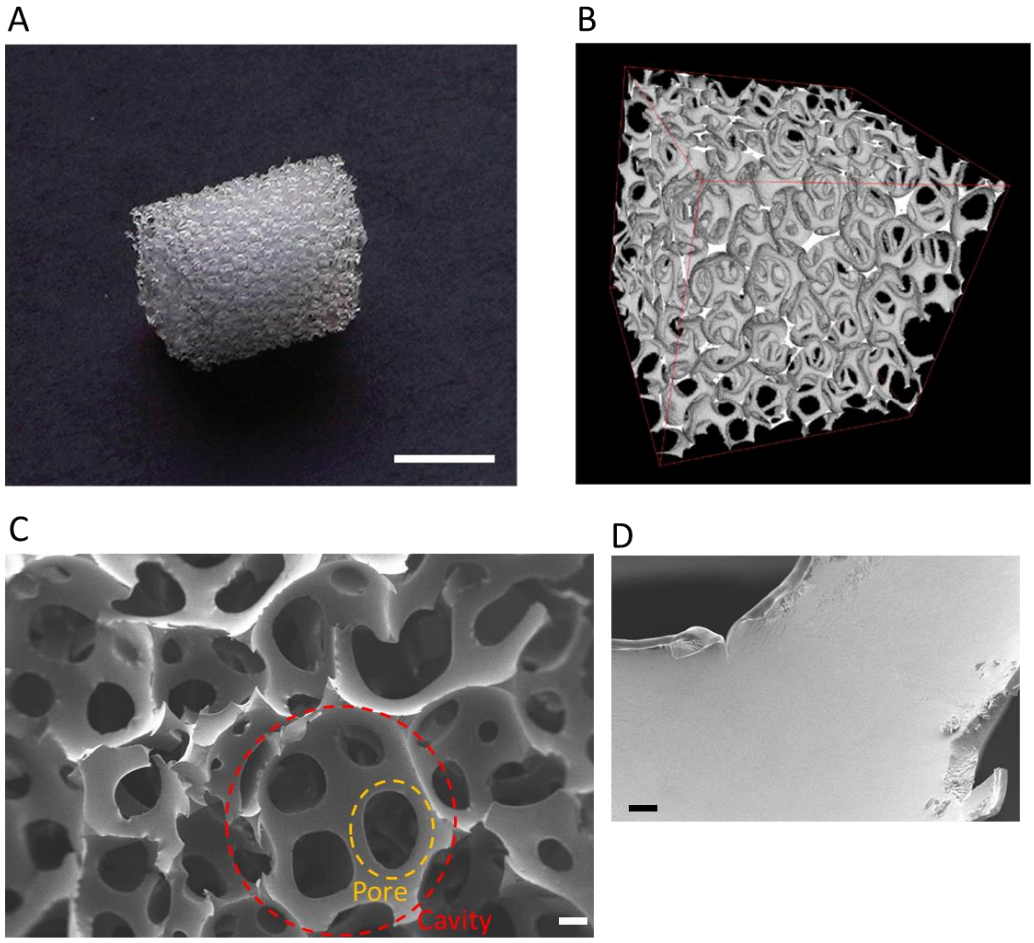

Figure 3.3.1: A) Polyurethane scaffold picture; B) µCT image of a PU sample. Square side length is 8 mm; C and D) SEM images of a PU scaffold. Scale bar are 0.5 cm in A, 200 µm in C and 20 µm in D.

Porosity (%)	**Trabeculae thickness (µm)**	**Pores diameters (µm)**	**Anisotropy degree**	**Surface (cm^{-2})**	**Connection density (μm^{-3})**
93.5	121.1 ± 55.1 Max 332.6	637.0 ± 188.7 Max 1212.2	0.3	11.82	5×10^{-9}

Table 3.3.1: PU scaffold parameters extracted from μCT analysis. The anisotropy degree specifies the tendency of the pore to be spherical (0 = completely spherical, 1 = maximum anisotropy), while the connection density indicates how much the structures are interconnected with each other.

These macroporous materials were developed by our collaborators at Tensive (s.r.l., Milan). More details on physicochemical characterization of the macroporous polyurethane can be found in the literature [87, 108].

Mechanical properties

Resembling Young's modulus of the skeletal muscle (E ≈ 10 kPa) is of paramount concern when designing a biomaterial with the function of reproducing tissue native mechanical properties.

For this reason, uniaxial compressive tests were performed on dry and wet PU scaffolds (i.e. after immersion in PBS for 24 h at 37°C). The two conditions share a very similar stress-strain curve (**Figure 3.3.2A**), with an initial linear regime followed by a plastic deformation until rupture, a behaviour typical of elastomeric materials. Wet samples manifested a more pronounced stress increase and a slightly higher Young's modulus (5.9 ± 1.01 kPa) compared to dry samples (3.56 ± 1.05 kPa) (**Figure 3.3.2B**). Nevertheless, Young's modules obtained perfectly fell in the desired range in both cases. Testing PU materials in wet conditions was done in order to verify to what extent liquid absorption can change scaffold elasticity. As a matter of fact, size comparison demonstrated an increment in diameter of roughly 2 mm (**Figure 3.3.2C**) when the scaffold was imbibed with PBS solution. This effect might have been reflected markedly on mechanical properties, but Young's modulus increased instead of just a few kPa. Therefore, it is possible to attest that muscle cells will feel a physiological substrate tension even when cultured on wet scaffolds.

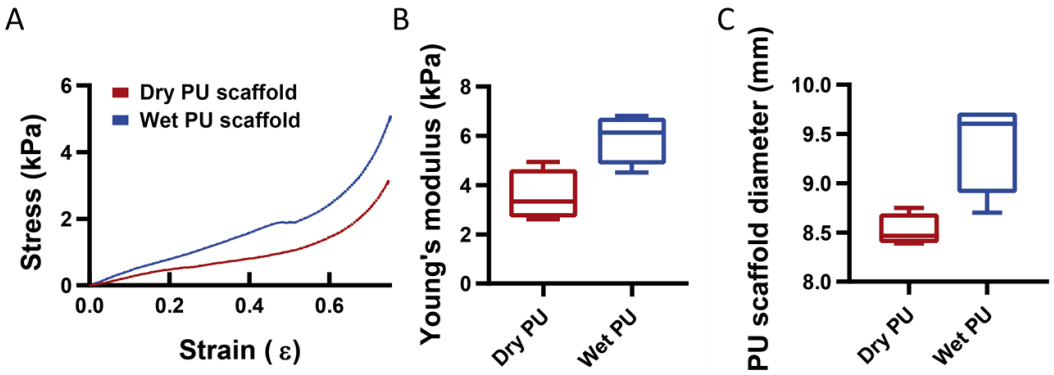

Figure 3.3.2: A) A representative stress-strain curve of a dry and wet PU sample; B) Young's modulus distributions of wet and dry PU samples; C) PU scaffold diameter distributions before and after immersion in cell medium.

Biodegradability

Scaffold stability over time is important for all long-term applications as SMTE and bio-hybrid robotics. After two months of being in its culture environment (i.e. immersed in DMEM at 37°C, 100 % of humidity, and 5 % CO_2) the PU scaffolds resulted to have non-significant variation in terms of weight variation (**Figure 3.3.3A**), attesting that no macroscopic and massive material degradation was occurring. On the other hand, the elastic modulus dropped by nearly 25 % after 60 days probably due to phenomena like polymer chains relaxation or matrix degradation at a molecular level (**Figure 3.3.3B**). Despite these mechanical changes, scaffold elasticity (E = 3.75 ± 1.0 kPa) was still abundantly within the range of the native skeletal muscle tissue, making such material an optimal candidate also for long-term culture systems.

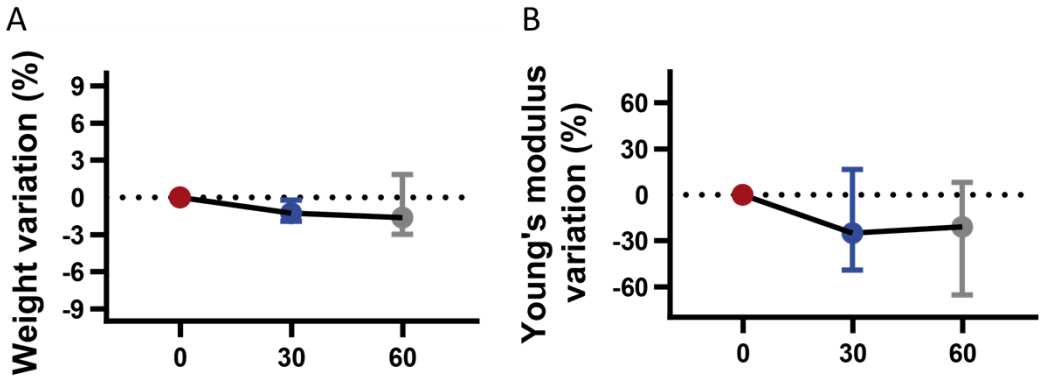

Figure 3.3.3: Biodegradation studies after 30 and 60 days. A) weight variation distributions; B) Young's modulus variation distributions.

3.3.2 PDMS shell characterization

The PDMS shell mechanical properties

The PDMS shell was designed to be a cylindrical film of PDMS with a length et least equal to the PU sample (1 cm) and a diameter of 9 millimetres, so to lightly squeeze the scaffold once inserted on its inside (from now on referred to as PU+shell) (**Figure 3.3.4D**). The purpose of such component was to confine cell culture medium and other solutions on the PU scaffold and to isolate muscle cells from the external environment, while, at the same time, guaranteeing high deformability to the whole device. This last point was the subject of several studies in order to develop a dip-moulding procedure that would produce shells with a homogeneous thickness in the order of few hundred µm, for at least 1 cm of their length. PDMS shell produced as described in **Chapter 3.5.2** resulted to be nearly 100 µm thick for at least 1 cm in the bottom portion (**Figure 3.3.4A, C**). Compressive uniaxial tests demonstrate that the implementation of the PDMS shell component had a minimal impact on PU Young's modulus (12.59 ± 1.38 kPa) (**Figure 3.3.4B**), thus preserving its elastic properties.

In conclusion, it is possible to attest that the PDMS shell was flexible enough to not prevail on the polyurethane Young's modulus, but, at the same time, sufficiently thick to do not break upon compressive deformation. Moreover, the PDMS shell surface was extremely transparent, due to the polished cavities of the aluminium mould, enabling to see inside the device by naked eyes and also by optical microscope.

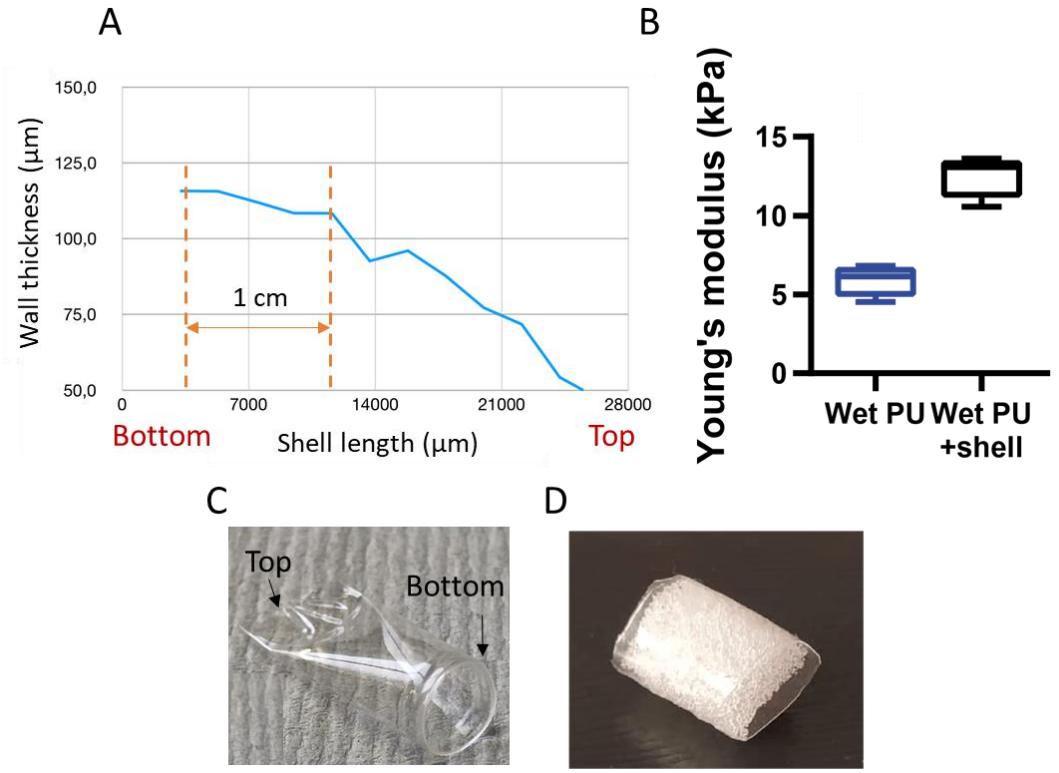

Figure 3.3.4: A) Thickness of the PDMS shell wall along its entire length (from bottom to top) measured at the microscope. Dashed lines highlight the PDMS shell portion used to envelop the PU scaffold; B) Young's modulus distributions of wet PU and wet PU+shell; C) Picture of a PDMS shell; D) Picture of a PU scaffold inserted in a PDMS shell.

At this point, there were enough information about mechanical properties to try predicting whether a fully mature skeletal muscle tissue cultured inside the scaffold would have been strong enough to squeeze the entire device upon contraction. This is particularly interesting in using such system as a bio-hybrid actuator.
By simulating a mature myotube cell culture of C2C12 (very common muscle cell line) inside the PU+shell system capable of emanating a contractile force of 1 µN, the PU structure is shortened by 1.84 % compared to its initial length (**Figure 3.3.5**). This would be already a good result by itself, but if the input force were increased by one order of magnitude (i.e. 10 µN) the displacement would rise to 16 %. This last result can be obtained by using a primary muscle cell culture intrinsically capable of larger self-contraction compared to commercial muscle cell lines.

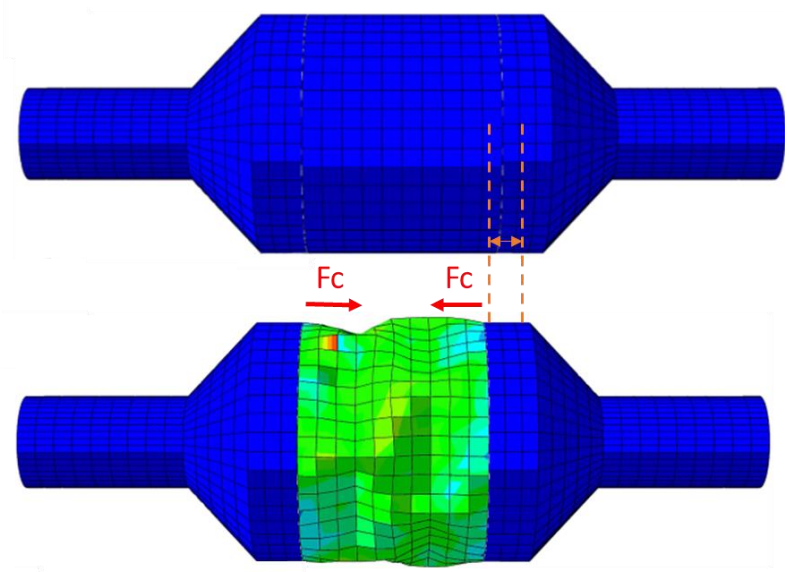

Figure 3.3.5: Simulation of device deformation upon skeletal muscle tissue contraction using as input force of 1 µN.

Resistance to cyclic compression

Cyclic dynamic compression tests were done in order to evaluate to which extent the PU scaffold enveloped inside a PDMS shell can withstand repeated mechanical deformation over time in wet conditions. We decide to test samples for a total displacement value of 5% and 10% since simulations on myotubes contractile force will in theory generate an overall shortening of the PU+shell scaffold that, in the best-case scenario, will lie around this threshold.

As can be seen at first sight from graphs in **Figure 3.3.6 A** and **B**, the mechanical stability of the PU+shell system resulted quite unperturbed at the end of tests. In fact, after an adjustment phase at the beginning of loading (usually within the first 10 cycles) where stress slightly increased, a steady plateau level was quickly reached. This behaviour is generally due to the internal friction of polymeric chains, having difficulties in flowing past one another when an incoming force is applied to the material. Differences between the stress registered at the first and at the last loading cycle were then quantitatively assessed by measuring the softening/hardening degree (SD) (**Figure 3.3.6C**). In both conditions, a minimal hardening effect was observed (4.44 % for 5% deformation and 0.25 % for 10 % deformation) demonstrating the ability of the PU+shell system to withstand a large number of actuation cycles.

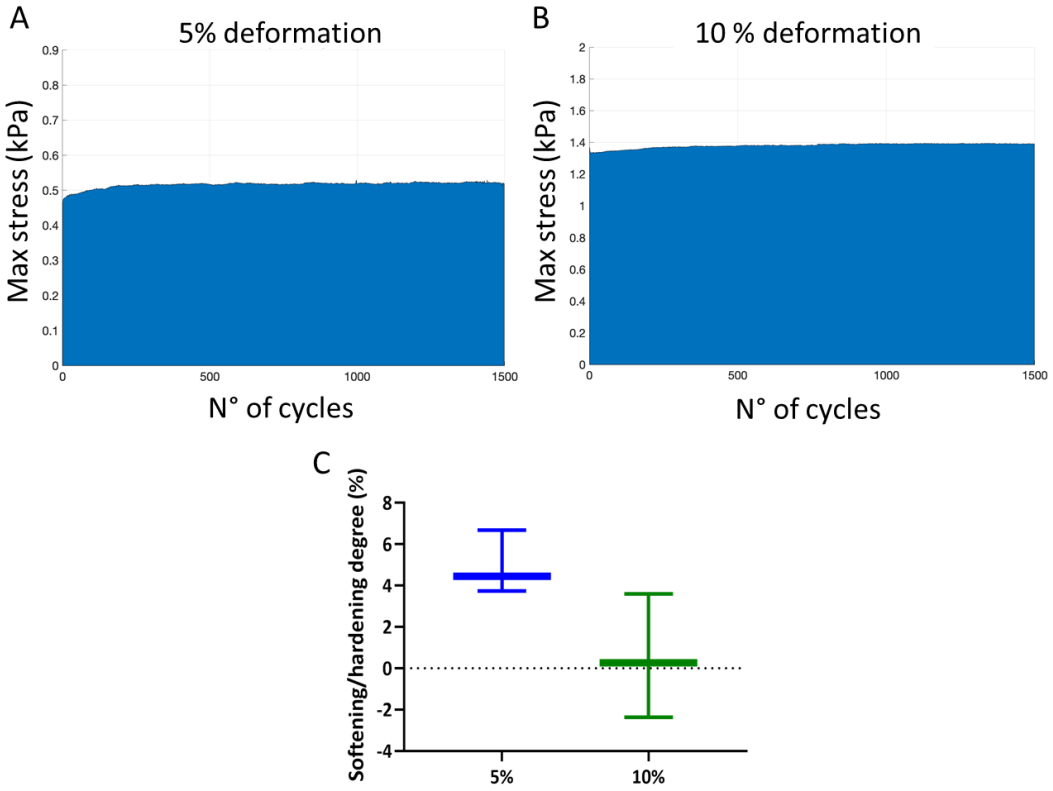

Figure 3.3.6: A) Cyclic compression plot at 5 % of deformation; B) Cyclic compression plot at10 % of deformation; C) Softening/hardening degree distributions at 5 and 10 % of deformation.

3.3.3 TMT device characterization

Resistance to cyclic extension

A picture of the assembled TMT device can be seen in **Figure 3.3.7**.

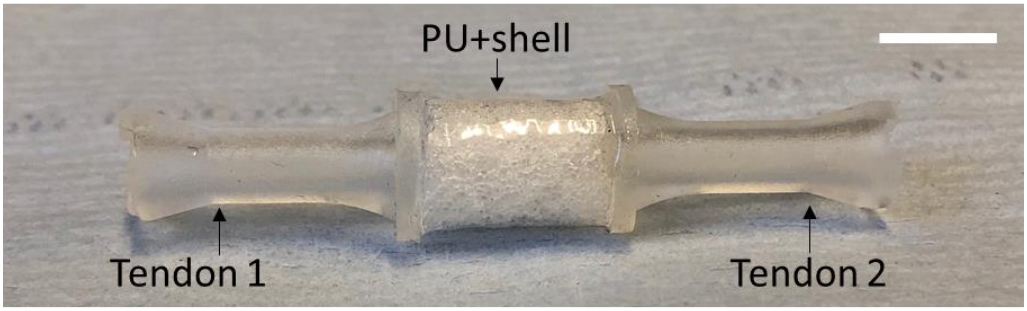

Figure 3.3.7: TMT device. Scale bar is 1 cm.

The two tendinous structures physically interpenetrated with the PU macropores have the fundamental function to transfer a force applied to the device to the central PU scaffold (e.g. during mechanical stimulation), or being produced by the muscle cells to any external apparatus (e.g. bio-hybrid actuation). For this reason, it was essential to perfectly bond together all the pieces of the TMT. Additionally, since the device will be constantly perfused with liquid (i.e. cellular medium) to provide cells with oxygen and nutrients, the bonding interface must be completely sealed.

To address TMT integrity, cycles of repeated extensions were performed as described in **Chapter 3.5.7**. No medium leak was ever detected in any of the integrity checkpoints and, at the end of the mechanical tests, it was still possible to pipet a liquid from one end to the other of the device (**Figure 3.3.8A**). From a mechanical stability point of view, there was a very unperceivable hardening effect (SD = 0.85 %) (**Figure 3.3.8B, C**) that further confirmed the resistance to fatigue of the TMT.

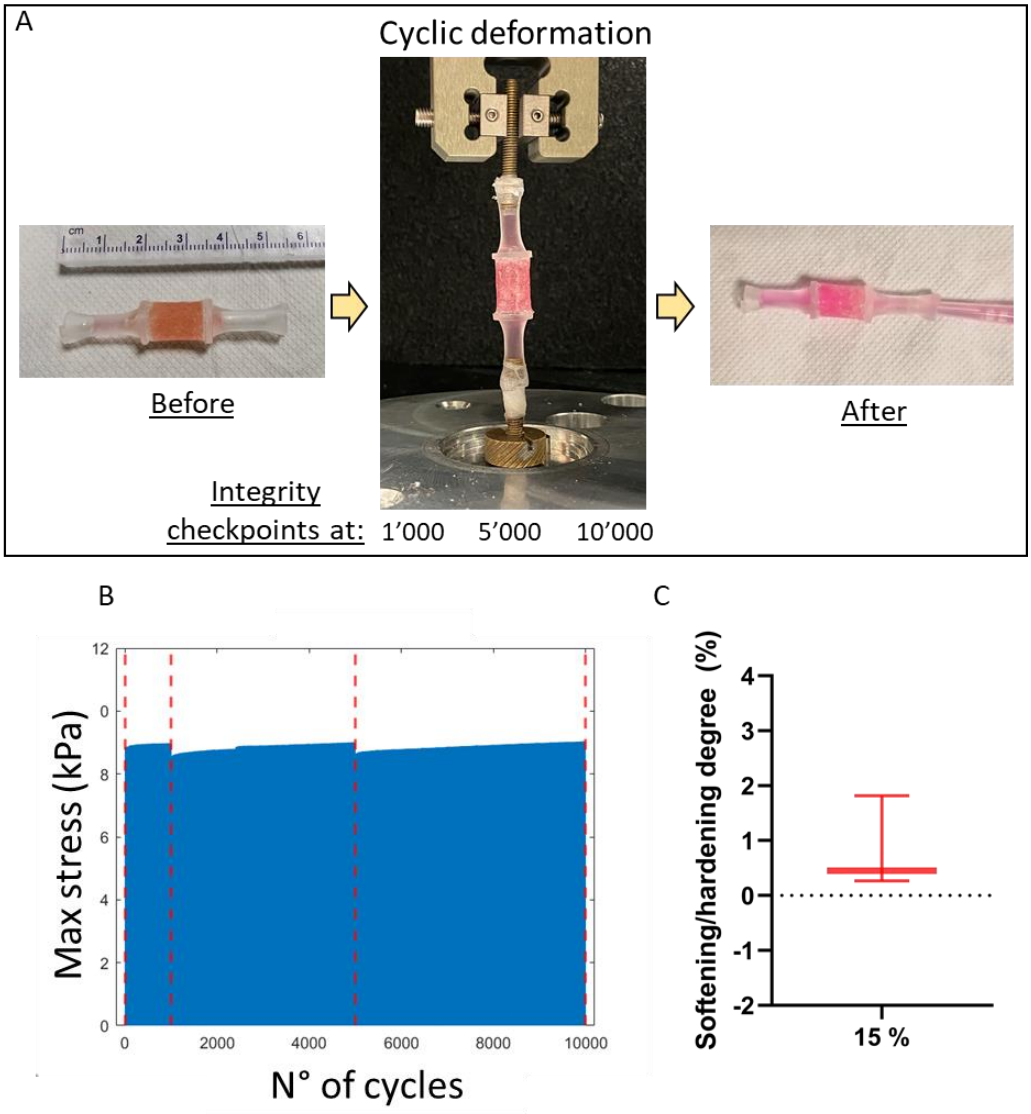

Figure 3.3.8: A) Schematic representation of cyclic extension analysis. TMT was filled with DMEM and sealed with parafilm to the Instron machine's clamps; B) Cyclic compression plot at 15 % of deformation. Red dashed lines represent integrity checkpoints; C) Softening/hardening degree distribution at 15 % of deformation.

Modelling fluid flow inside the TMT

Scaffold permeability is directly linked to its architecture (e.g. porosity, pore size, and pore interconnectivity) and strongly influences mass transport properties independently from the fluid permeating the material [109].

The average PU scaffold intrinsic permeability obtained through experimental tests was 1.71×10^{-9} m^2 (median value). This value resulted slightly larger than values found in the literature for porous 3D scaffolds [110, 111], but is coherent with the material's high porosity and large pores' diameter. Most importantly, the permeability value was in the same range as that one obtained through fluidic simulations. Such match confirmed the reliability of our fluidic model and pave the possibility for subsequent computational analysis, in particular of local wall-shear stress (WSS) and velocity distributions within the scaffold.

Local WSS was computed through representative volume elements (RVE) as described in **Chapter 3.5.10**, for flow rates of three different orders of magnitude (0.022, 0.22, and 2.2 ml/min) (**Figure 3.3.9A**). The critical shear stress for cell detachment to occur depends on the material on which they are cultured and on the cell type, but it has been found between 1 and 3 Pa [112]. From fluidic simulations, the average WSS value was always found below this threshold for every condition (**Figure 3.3.9B, C**). A higher shear stress level (WSS_{MAX}) was registered only in few points of the scaffold when the maximum level of flow inlet (i.e. 2.2 ml/min) was imposed.

A

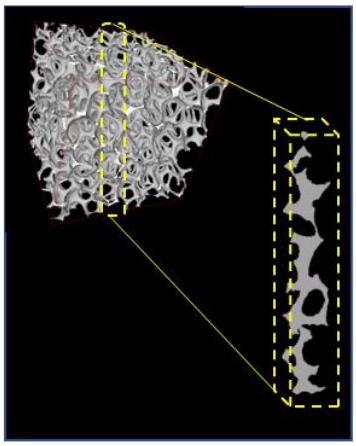

B

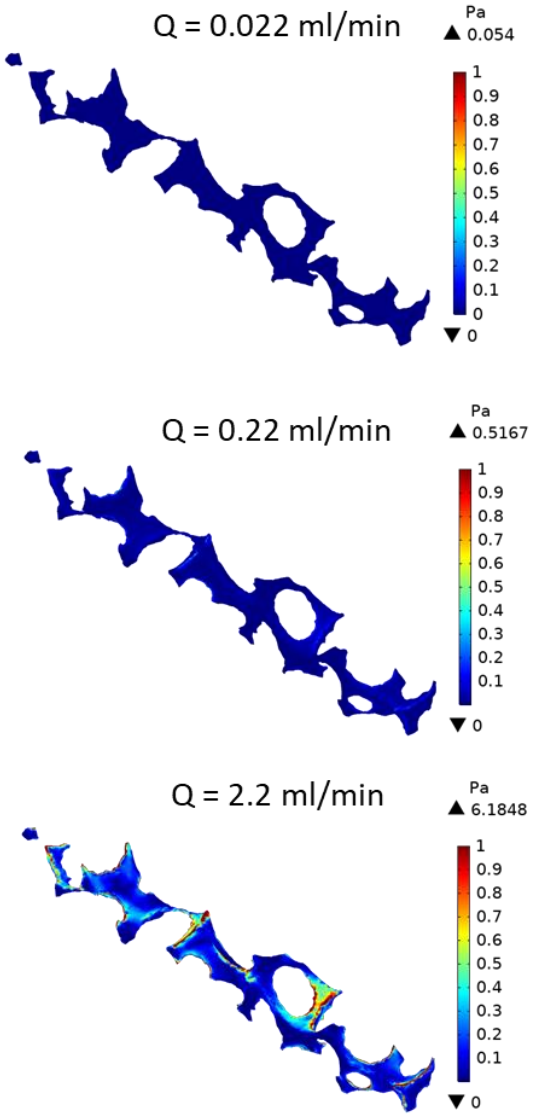

C

Q_{IN} (ml/min)	WSS_{AVG} (Pa)
0.022	0.00238 Max 0.054
0.22	0.024 Max 0.5167
2.2	0.32 Max 6.1848

Figure 3.3.9. A) Schematic representation of a RVE extraction from the PU scaffold µCT file; B) Estimated local wall-shear stress in the PU scaffold for a flow rate (Q) of 0.022 ml/min (top), 0.22 ml/min (middle), and 2.2 ml/min (bottom); C) Table with average and maximum WSS value for each flow rate imposed.

Velocity distributions at the polyurethane-channel interface were also evaluated, using the same inlet flow values used in WSS calculation. Streamlines at the impact zones can be visualised in the left column of **Figure 3.3.10**, whereas on the right one, modules variation along x and z directions are reported. The optimal perfusion velocity it is a parameter that can be easily estimated on the base of cell line-related variables (i.e. oxygen and nutrients consumption rates and the number of cell in culture) and scaffolds-related variables (i.e. geometrical factors) [78].

For a C2C12 cell culture with 10^6 - 10^7 cells per PU scaffold, a perfusion velocity within a range of 0.166 -1.66 mm/s can sustain viability [113]. For this reason, these values were set as interval thresholds were to calculate the percentage of scaffolds' area covered by the correct range of perfusion velocity. The best result was obtained when the maximum flow rate (2.2 ml/min) was imposed at the inlet (65 % along x, 77 % along z). Even with the intermediate flow rate (0.22 ml/min) tested, the scaffold was still partially covered with velocity within range (35 % along x, 21 % along z). On the contrary, the minimum flow rate (0.022 ml/min) did not allow to reach a significant perfusion velocity coverage (0 % along both x and z).

Overall, the fluidic computation analysis made, allowed us to predict reliable flow rates to be imposed within the TMT device to effectively sustain a C2C12 dynamic cell culture [114]

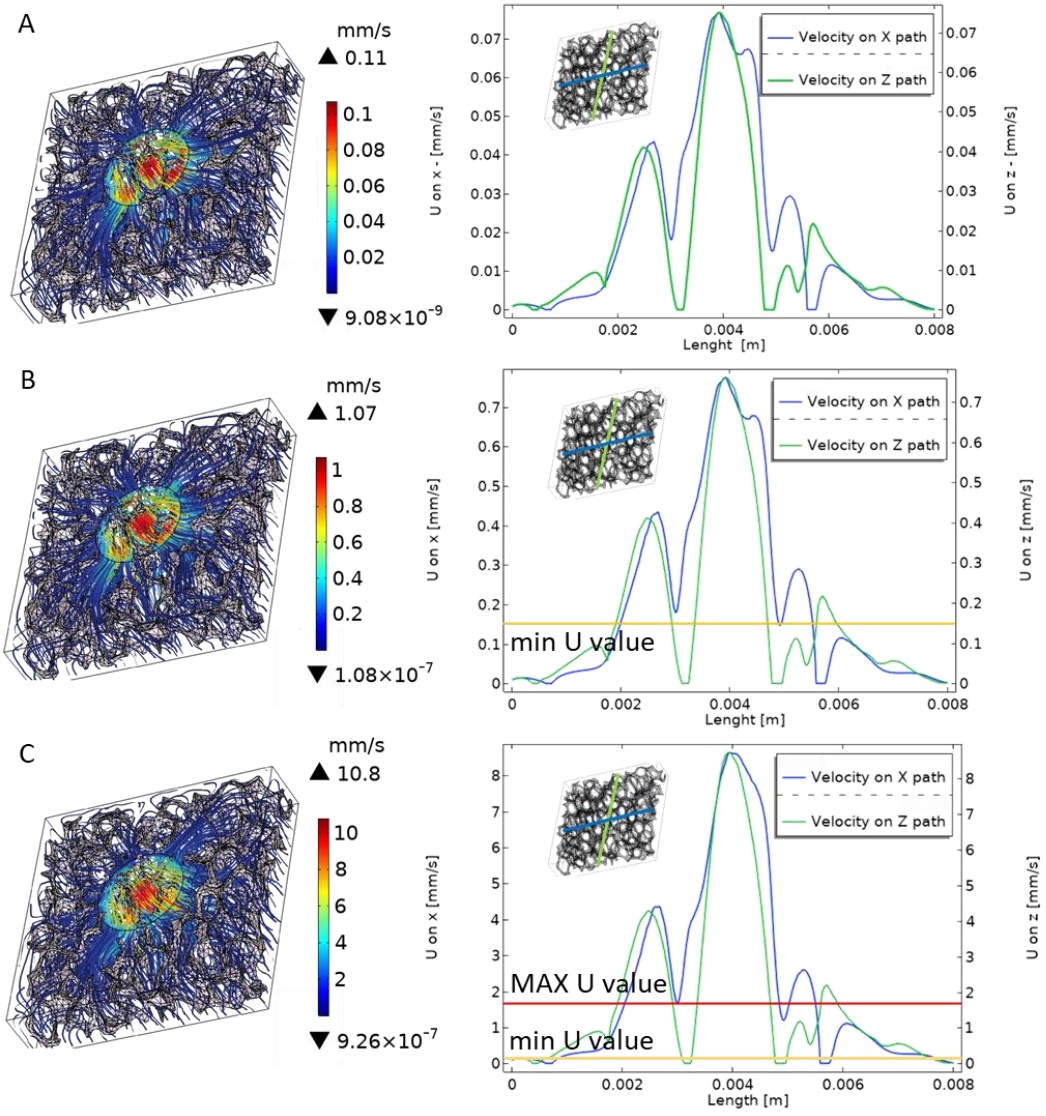

Figure 3.3.10: Streamlines at the polyurethane-channel interface (left column) and velocities' module (U) along x and z paths (right column) for a flow rate of 0.022 ml/min (A) 0.22 ml/min (B) and 2.2 ml/min (C). The yellow and red lines represent the minimum and maximum optimal perfusion velocity.

3.3.4 Biological *in vitro* assays

Myoblast's proliferation in functionalised PU scaffolds

Our polyurethane material was completely inert from a bio-adhesiveness point of view. For this reason, we decided to activate its surface through plasma oxygen treatment so to covalently link some of the most abundant ECM proteins found in the native skeletal muscle tissue basal lamina.

Myoblast proliferation onto functionalised PU scaffolds was evaluated in the presence of two different ECM proteins, laminin (LMN) and fibronectin (FN), and was compared with samples just treated with plasma oxygen (plasma PU). DNA content, which is directly correlated with cell proliferation, underwent a significant 1.3-fold increase on the plasma PU samples and of 1.6-fold on both the protein-coated scaffolds over the period analysed (**Figure 3.3.11**). Nonetheless, statistical analysis showed no significant differences in the proliferation rate between the three different conditions, attesting that surface activation by plasma oxygen is already by itself capable of enabling cell attachment to the polyurethane material. This was possible due to the change from hydrophobic to hydrophilic of PUs' surfaces, which is well known to promote cell attachment.

However, we decided to keep functionalise PU scaffold with ECM proteins since the transition between myoblast proliferation and differentiation is regulated by cell-ECM protein interactions, including FN and LMN.

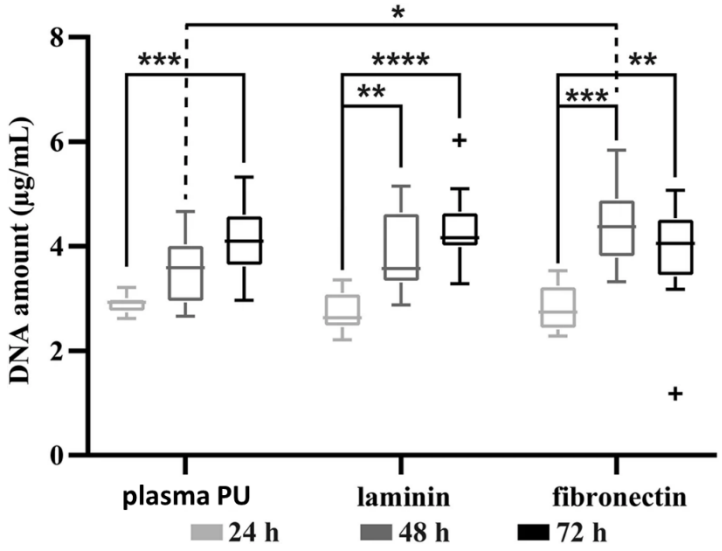

Figure 3.3.11: Cell proliferation assay after 24, 48 and 72 h on bare PU and on LMN- and FN-coated scaffolds (*p ≤ 0.05; **p ≤ 0.01; ***p ≤ 0.001; ****p ≤ 0.0001. Black crosses: outlier values).

Myoblast's differentiation with electrical stimulation

The Electric stimulation (ES) applied to each PU-based sponge was evaluated through a finite element method analysis. The computational results obtained allowed to describe the electric field in the area where muscle cells were differentiating (**Figure 3.3.12**). A small and linear electrical field variation was observed within the PU scaffolds indicating that the cells were stimulated by an electric field with a quite homogeneous strength from 3.4 to 4 V/cm, which falls within the physiological range of 0.1–10 V/cm [95, 115].

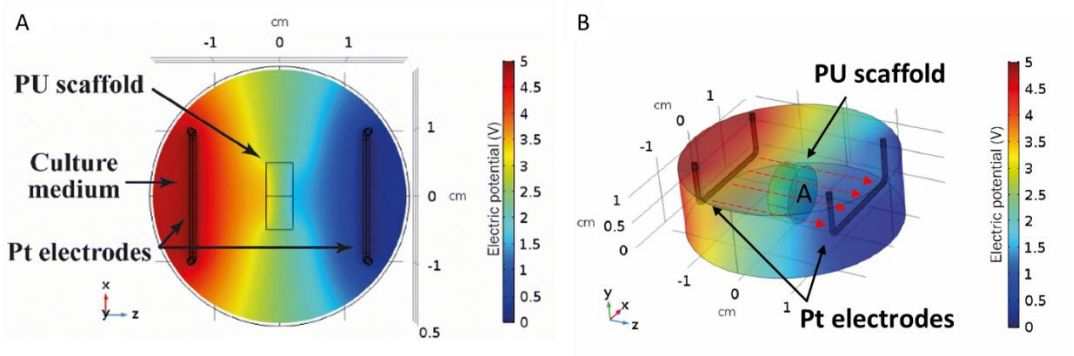

Figure 3.3.12: Top (A) and 3D (B) view of the electric potential distribution within the simulation environment. The PU scaffold cross-section (A) is positioned perpendicularly the electric field lines (red dashed lines).

Myotube morphology was analysed by fluorescent imaging for f-actin and **Figure 3.3.13** compares some representative 3D images of the samples in the four experimental conditions (i.e. plasma PU, plasma PU+ES, laminin, and laminin+ES). Samples not exposed to ES displayed quite abundant dispersion of cell groups in the analysed volumes, with the presence of spheroid-like clusters connected to the walls through small branches of elongated cells. Compared to the plasma PU, the LMN coating itself slightly influenced the spreading of the spheroid-like structures, with a reduction of their roundness in favour of the formation of small protrusions, represented by elongated myotubes.
ES is the most important cue for skeletal muscle tissue development and maturation and has been used to successfully differentiate myoblast into elongated myotubes [116]. Noteworthy, ES for 48 h greatly enhanced myotube formation: spheroid-like structures resulted nearly absent in the analysed samples and cells assumed an organization similar to large bundles of elongated and differentiated myotubes, both on the plasma PU+ES and on the laminin+ES samples. Furthermore, the concurrent presence of LMN and ES remarkably fostered the formation of more elongated myotube bundles, creating a tangled network spanning throughout the pores and cavities.

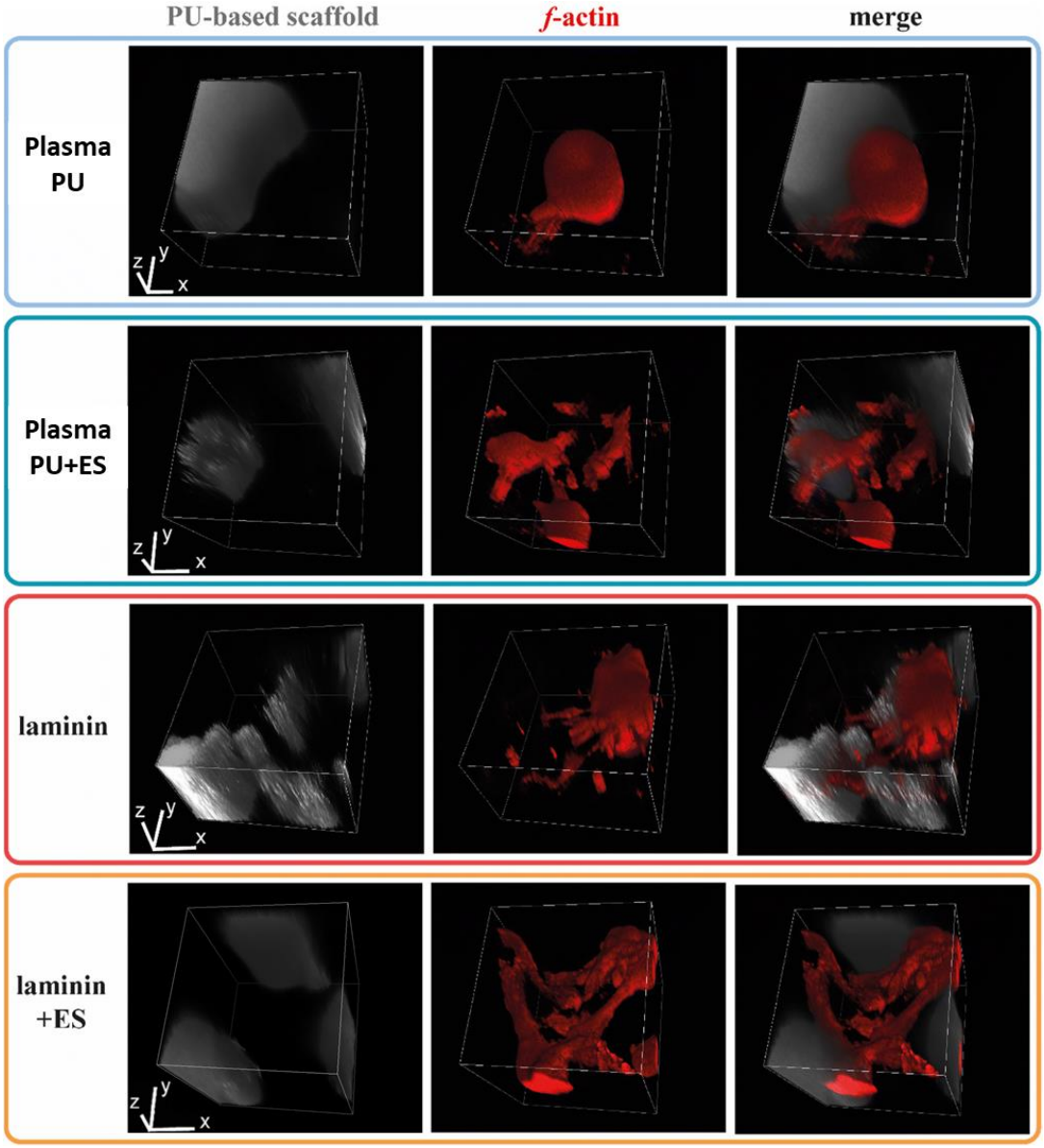

Figure 3.3.13: 3D confocal laser scanning microscopy images of myotubes in PU-based scaffolds in different conditions after 6 days of differentiation. Grey: PU-based scaffold (transmitted light); red: f-actin (TRITC-phalloidin). Plasma PU: width (y) = 381.88 µm, height (x) = 381.88 µm, depth (z) = 210 µm; Plasma PU+ES: width (y) = 381.88 µm, height (x) = 381.88 µm, depth (z) = 375 µm;

laminin: width (y) = 381.88 µm, height (x) = 381.88 µm, depth (z) = 225 µm;
laminin+ES: width (y) = 381.88 µm, height (x) = 381.88 µm, depth (z) = 405 µm.

Such qualitative observations were confirmed by quantitative analyses, obtained by measuring the diameter and length of myotube bundles (**Figure 3.3.14**). The absence of ES prohibited almost completely myotube bundles formation. Muscle cells were confined in small groups of one or two cells and were characterized by a reduced length and diameter compared to the electrically stimulated samples. No significant influence of ES or LMN alone was observed. On the contrary, in the presence of both LMN coating and ES, myotube bundles triplicated their length and doubled their diameter, thus corroborating the qualitative images analyses.
Overall, ES application in co-operation with ECM protein PU scaffold functionalization was correlated with a clear abundance of longer and wider myotube bundles, when compared to other culture conditions.

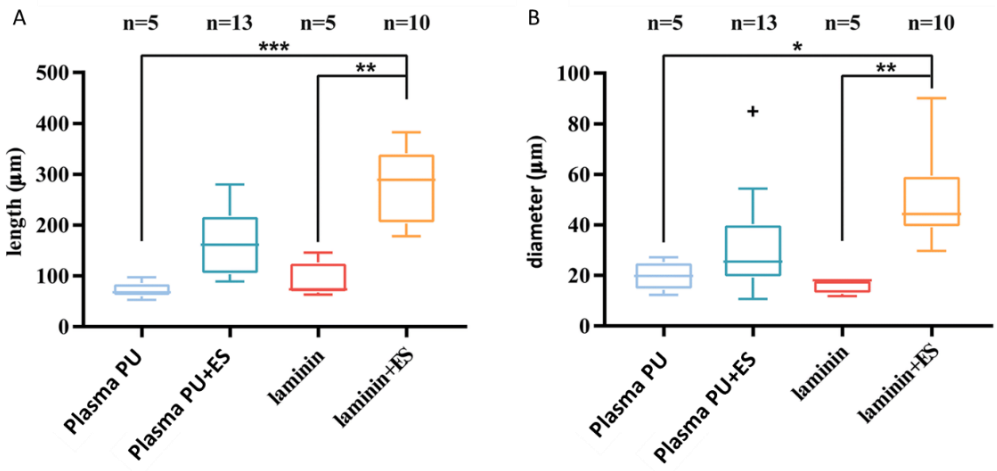

Figure 3.3.14: Quantitative analyses of myotube bundles in PU-based scaffolds in different conditions after 6 days of differentiation. Distribution of myotube lengths (A) and diameters (B). The number of bundles analysed in each condition

(n) is reported on top of each box plot (***p ≤ 0.001; **p ≤ 0.01; *p ≤ 0.05. Black cross: outlier value).

PU scaffolds wet functionalization with polydopamine

In all of the biological experiments described in the previous paragraphs muscle cell cultures were done on PU scaffolds alone, not already inserted in the PDMS shell nor physically interpenetrated with the tendon-like structures. Despite the optimal results in using plasma oxygen to activate PU surfaces, it proved to be impossible to replicate the methodology once the polyurethane material was inside its PDMS envelop. For this reason, we also had to develop a functionalization method that could be performed on the assembled TMT device. In such context, we succeed in adapting to our material the polydopamine coating strategy developed by Lee et al. [71, 70]. After the dopamine coating, PU samples appeared brown-coloured, which is a trend-mark of catechol oxidation and subsequent dopamine self-polymerization [70] (**Figure 3.3.15**).

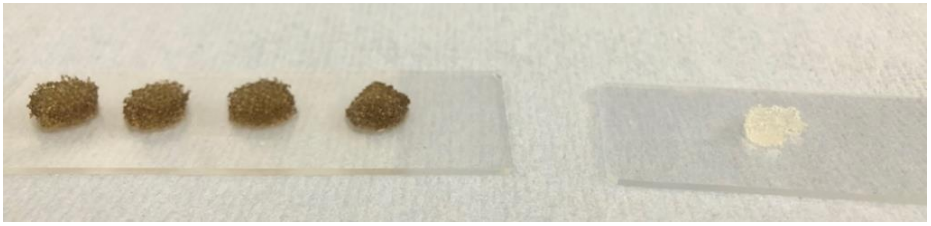

Figure 3.3.15: PU scaffolds covered with polydopamine (left) and a bare PU scaffold (right).

Epifluorescence microscopy images showed in **Figure 3.3.16** compares the three experimental conditions used to culture C2C12 myoblasts on PU scaffolds: non-treated (bare PU), polydopamine-coated (dopa PU), and polydopamine-coated with FN (FN PU) samples. As it can be seen

cell adhesion on bare PU scaffolds was completely denied due to the lack of recognisable moieties on their surface. Polydopamine coating instead improved surface bio-adhesiveness by enhancing its hydrophilicity. However, the strongest effect was undeniably achieved by covalently link ECM proteins onto the polydopamine layer. FN PU samples were completely covered by myoblasts indicating a uniform and strong functionalization of the scaffold surfaces.

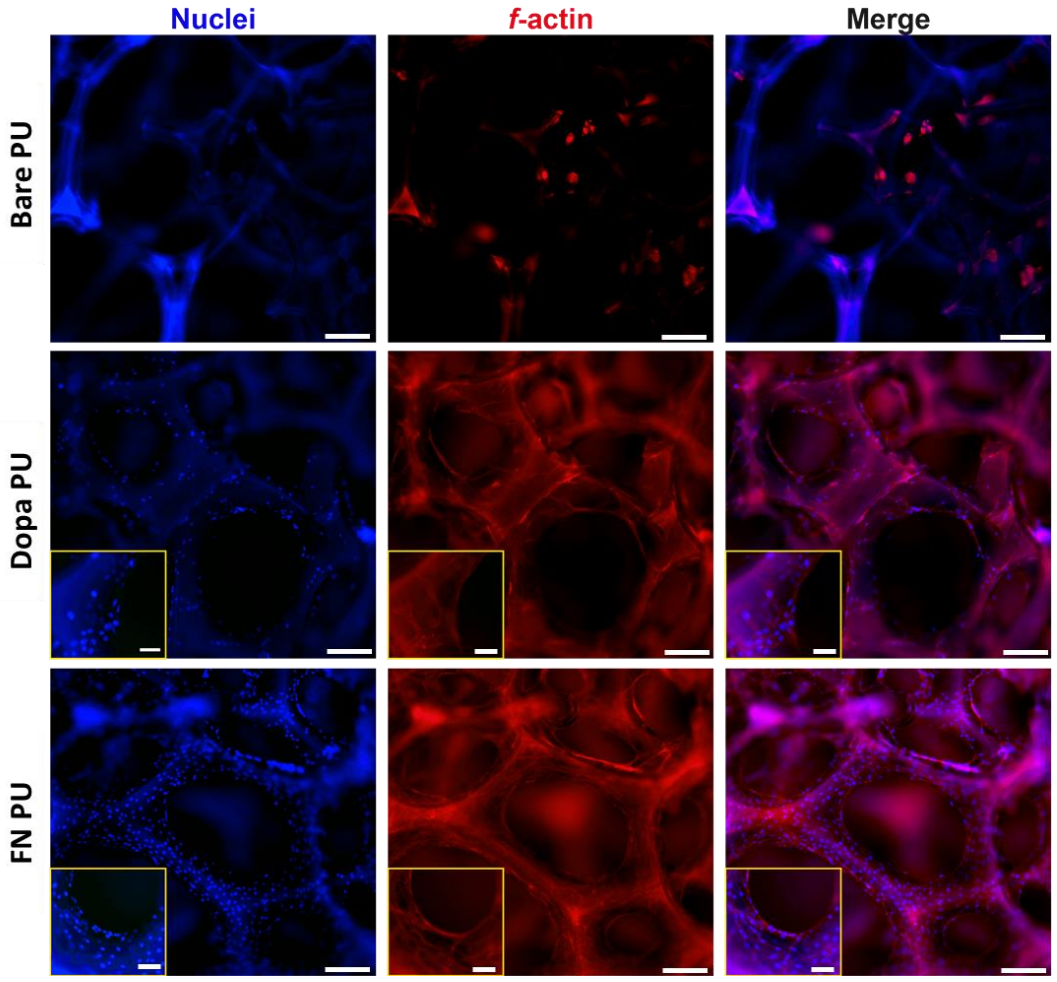

Figure 3.3.16: Epifluorescence images of C2C12 myoblast cell cultures on untreated (bare PU), polydopamine-coated (middle), and polydopamine-coated with fibronectin (bottom) PU scaffolds. Images were taken after 3 days of culture.

Red: f-actin (TRITC-phalloidin), Blue: nuclei (DAPI). Scale bare is 200 µm. Scale bare inside yellow squares is 50 µm.

Since the best results were obtained with the combination of polydopamine coating and FN functionalization, a differentiation protocol was applied to this condition as described in **Chapter 3.5.16**. Confocal images showed thick and long myotubes all over the PU cavity's surfaces (**Figure 3.3.17**).

All of these results proved the efficacy of Lee and co-workers' wet functionalization methodology in immobilizing biomolecules onto polymeric materials, and relative to this work, enabled the future possibility to attach skeletal muscle cells inside the TMT device once already assembled.

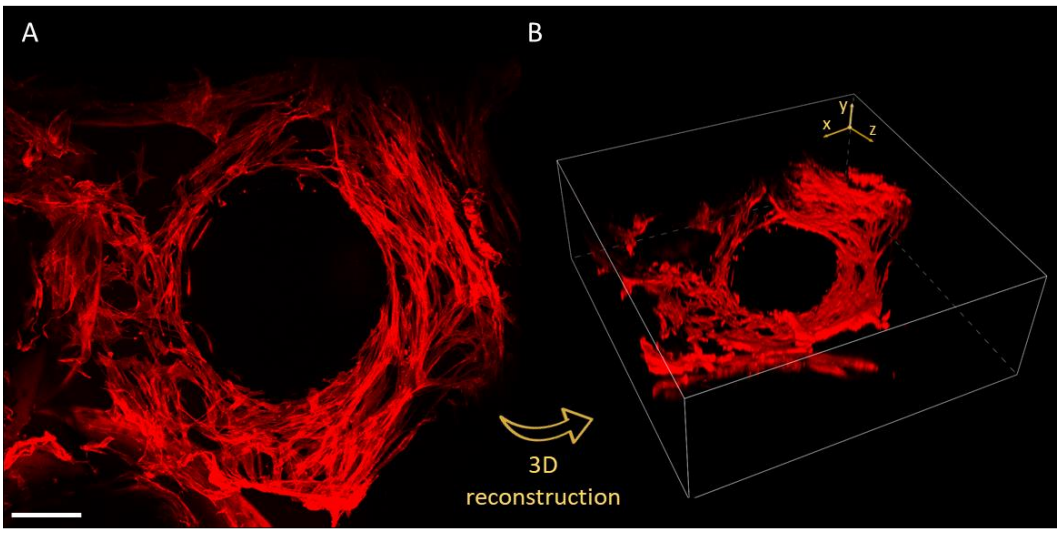

Figure 3.3.17: A) Confocal microscope image of a PU scaffold coated with polydopamine and functionalised with fibronectin after 5 days of cultures (switching to DM at day 4). Scale bar is 200 µm; B) 3D reconstruction of image A. Red: f-actin (TRITC-phalloidin). Width (y) = 800 µm, height (x) = 250 µm, depth (z) = 800 µm.

3.4 Conclusions & Future Outlooks

The TMT device presented in this work demonstrated to be a suitable system to allow three-dimensional skeletal muscle cell cultures *in vitro*, capable of mimicking the native tissue niche in terms of morphology, architecture, and biology.

Future experiments concentrate exclusively on developing a macroscopic muscle cell culture inside the TMT device. In order to achieve this main goal, two parallel lines of research are being pursued: (i) confirming experimentally the predicted flow rate values to sustain muscle cell life inside the TMT; (ii) developing a mechatronic platform to foster myoblasts differentiation into mature muscle fibers.

Regarding the first task, experiments are already ongoing. A set of TMT devices have been functionalised with a polydopamine coating layer linked to fibronectin proteins following protocol describes in **Chapter 3.5.16** and, by using a multi-channel peristaltic pump, a cell suspension is being seeded and dynamically maintained in culture with the predicted perfusion velocity values (**Figure 3.4.1A, B**). The results of such experiments will enable us to identify the best culture conditions for cell adhesion and proliferation in the device.

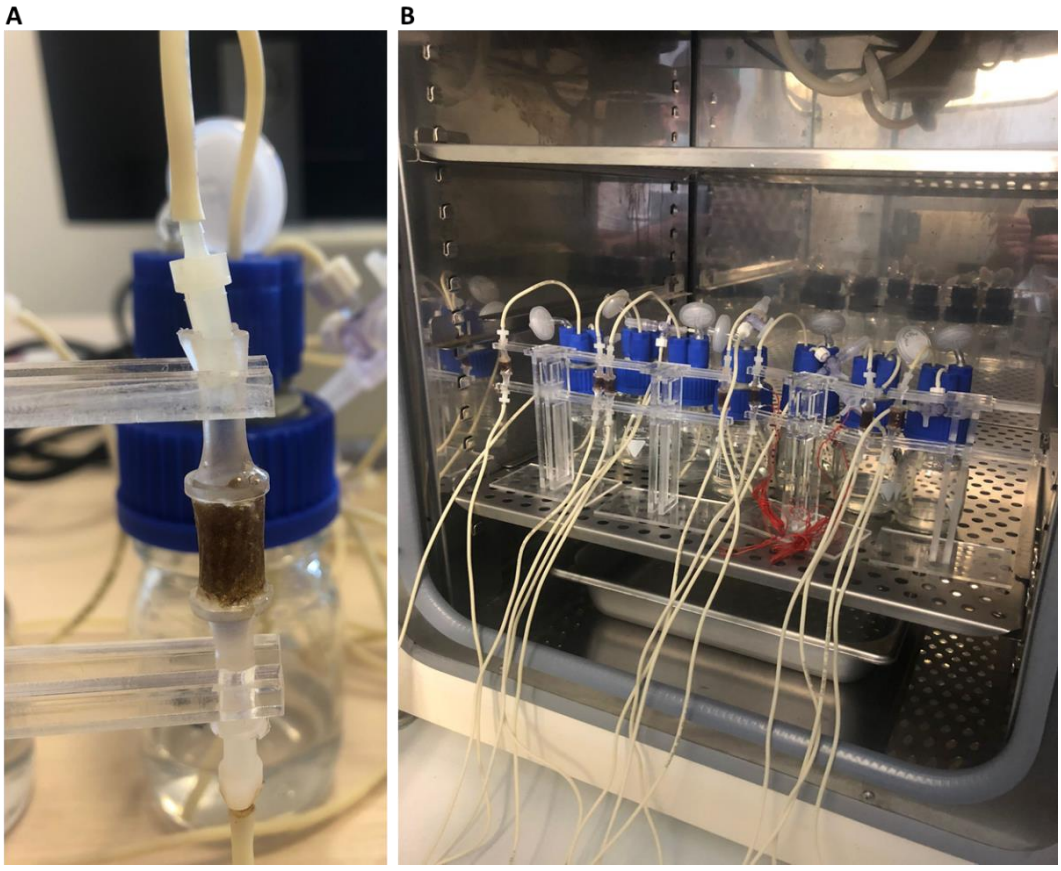

Figure 3.4.1: Dynamic myoblast cell culture inside TMT device. A) single TMT coated with polydopamine (black colour); B) Array of TMT inside an incubator to be tested with different flow rates for myoblast cell culture.

Given the good results presented in **Chapter 3.3.4** the second task will be achieved mainly by cell electrical stimulation. To do this, the TMT device will be provided with two soft electrodes made of a very thin PDMS layer with nano-gold particles implanted on its surface (**Figure 3.4.2A**) capable of generating an electric field within the physiological range. Furthermore, since such soft electronic components will not hamper the overall device deformation, it will be possible to apply mechanical stretching to the cell culture. This last point is of paramount

importance in the context of aligning muscle cells along a preferential direction. The custom-made mechanical stretching platform showed in **Figure 3.4.2B**, will be used to fulfil this purpose.

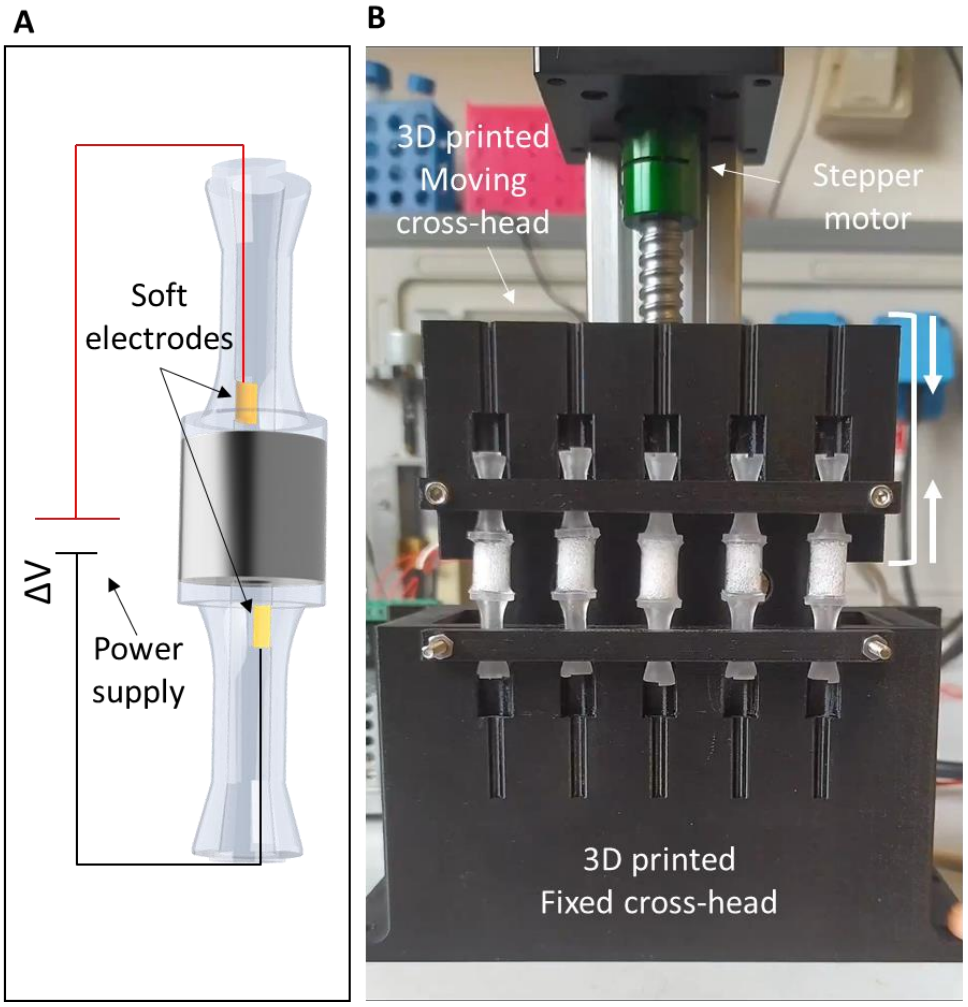

Figure 3.4.2: A) illustration of two soft electrodes integrated into the TMT device; B) Mechanical stretching platform with five TMT devices.

In conclusion, in the next few months, we expect to develop through a bottom-up approach one of the first examples to be found in the literature

of skeletal muscle tissue construct at the macroscale in an all-soft multi-functional bioreactor. The achievement of this goal can potentially be considered a big step forward in the field of skeletal muscle tissue engineering and bio-hybrid robots powered by muscle cells contraction.

3.5 Experimental Section

3.5.1 Polyurethane macroporous scaffold

- *Mixture A* (polyols): 16.00g PEG 2000 (Sigma Aldrich, 99%, 79.46 pphp); Glycerol 1.72g (Sigma Aldrich, ≥99% (GC), 8.57 pphp) and 2.4g MilliQ water (11.96 pphp).
- *Component B* (polyisocyanate): 63.87 g Tolonate™ X FLO 100 (Vencorex, ≥99%). NCO index = 100.
- *Component C* (catalyst): 0.38 g Dibutiltindilaurate DBTL (Sigma Aldrich, ≥ 96.0 %). %DBTL = 0.5% w/w.

The mixture A was introduced in a 2L-PP rectangular container endowed with a lid, then placed in the oven at 85°C for at least 30 min. The temperature of mixture A was 80°C when components B and C were added. The resulting compound was mechanically mixed at 300 rpm for 30 s, then left raising for 1 min, until the expansion was arrested due to crosslinking. The raw foam was kept in the oven at 40 °C for 24 h to complete the curing process. Finally, samples were cut in the shape of 3 cm long cylinders with a diameter of 1 cm and were purified according to the procedure previously described in Gerges et. al. [108].

3.5.2 Protective PDMS shell

12 g of PDMS (SYLGARD™ 184) pre-polymer solution were mixed with 0.6 g of curing agent (PDMS:crosslinker ratio of 20:1). Afterward, the solution was stirred for 20 minutes and degassed for 20 minutes with a vacuum pump.

The custom-made set-up used for dip moulding consisted of an aluminium mould, an automatic micro-shifter, and an oven (**Figure 3.5.1A**). The mould is a 3 cm tall cylinder made of aluminium with four smaller cylindrical polished cavities (diameter = 9 mm) that can be

connected to the micro-shifter by a threaded rod (**Figure 3.5.1B**). The micro-shifter is composed of a 28BYJ-48 step motor controlled through an Arduino UNO board that can linearly move a rail up and down.

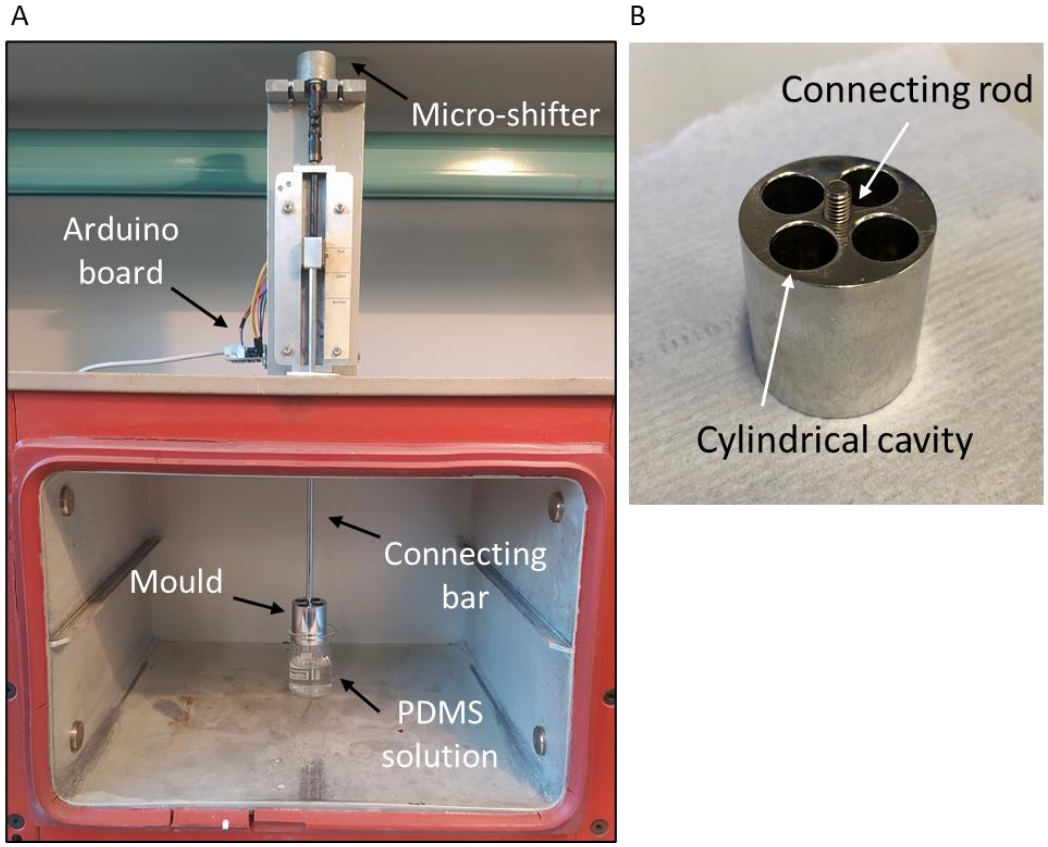

Figure 3.5.1: A) Dip-moulding custom-made set-up; B) Aluminium mould.

Dip-Moulding protocol

Before starting the dip-moulding procedure, the mould was heated in the oven at 110°C so that the aluminium mould surface could reach a temperature of roughly 92°C. At this point, the shifter was activated and moved inside of the PDMS pre-polymer solution at 0.25 mm/s. Once fully submerged in the PDMS, it remained in place for 35 seconds (lag time). When lag time expired, the mould was withdrawn with a speed of

0.125 mm/s. The mould coated with the PDMS remained inside the oven for one hour to complete crosslinking. The final step, demoulding, is done after cooling the aluminium mould. By using a scalpel and a pair of tweezers four thin PDMS shells can be easily detached from the mould and four PU scaffolds can be enveloped inside them (**Figure 3.5.2**).

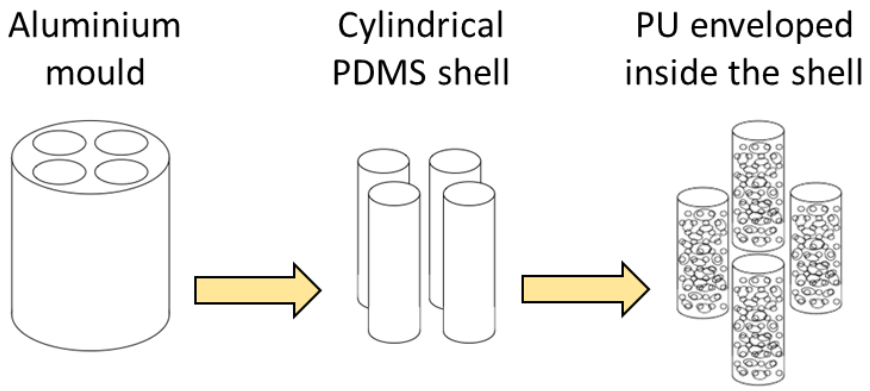

Figure 3.5.2: Schematic workflow of the demoulding procedure from the aluminium mould

3.5.3 Tendon-like structures

Tendon-like structures were manufactured using a 3D printed sacrificial mould technique. The mould was designed using a CAD software (Fusion 360, Autodesk) and then printed using a stereolithographic 3D printer (Formlabs Form 2) with a photopolymerised resin as material (Formlabs Standard Clear V4 resin). At this point, the pre-polymer solution was prepared (PDMS:crosslinker ratio of 10:1) and stirred for 20 minutes. Afterward, the mixed solution was poured inside a syringe provided with a needle and injected inside of the sacrificial mould. Then, the mould was degassed for 20 minutes with a vacuum pump and is placed inside the oven (T = 110°C) for 1 hour to complete PDMS crosslinking. Finally, the mould is gently disrupted using a pair of nippers so to release the PDMS tendon (**Figure 3.5.3A**).

For the TMT assembly, the protocol was slightly changed as described in **Chapter 3.5.4**.

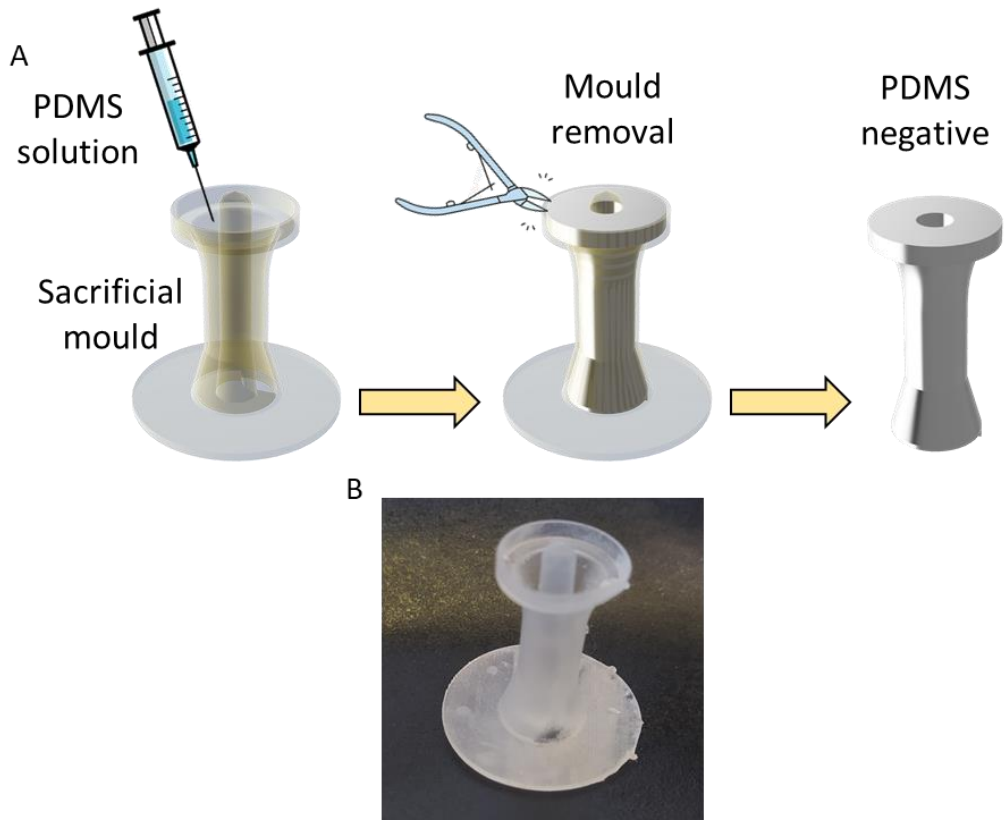

Figure 3.5.3: A) Schematic workflow of the sacrificial mould technique; B) Real picture of a 3D printed sacrificial mould for tendon-like structures fabrication.

3.5.4 TMT fabrication process

To assemble the several TMT components, a multi-step procedure was developed. The strategy consisted in physically interpenetrating the macropores of the PU scaffolds with the PDMS pre-polymer solution of the tendon-like structures during their curing in the oven. A triaxial-

moving clamp with a metallic claw was used to precisely drive the sponge through micro-metrical screws and to hold it in position.
First of all, the tendon-like structures were prepared as described in **Chapter 3.5.3**, but in this case, the PDMS pre-polymer solution was cured only for 6 minutes in the oven. At this point, the PU+shell was lowered in the viscous, but still liquid, PDMS pre-polymer solution. The platform is then placed again in the oven (T = 110 °C) for 15 minutes to allow physical crosslinking (**Figure 3.5.4A**). The procedure is repeated to attach a second tendinous structure on the opposite side of the PU scaffold (**Figure 3.5.4B**). The assembled TMT device is post-cured in the oven at the same temperature for another 40 minutes. In the end, the sacrificial moulds still enclosing the two tendon-like PDMS structures were disrupted using a pair of nippers.

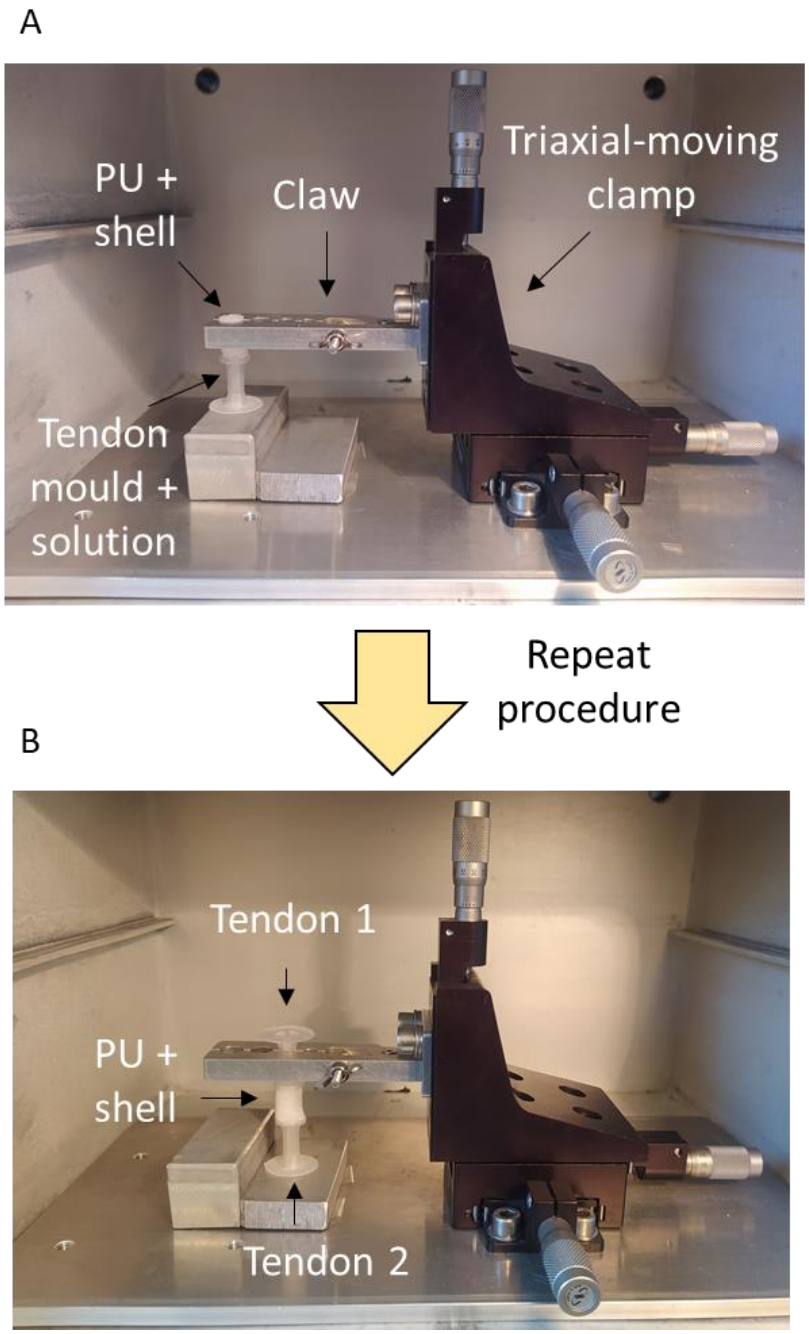

Figure 3.5.4: A) Crosslinking tendon one to the PU scaffold; C) Crosslinking tendon two to the other PU scaffold side.

3.5.5 Micro-computed tomography (μCT)

The files obtained from the μCT were used to set up the computational model. They were obtained through a customized cone beam system known as TomoLab (cone beam energy = 40 kV, power = 200 μA, exposition time = 1.5 s). The dimension of the tomographic projections was 2004 × 1335 pixels and the final resolution was 8 μm. The slices reconstruction and correction were carried out through the software Cobra Exxim and the binary processing of the images was accomplished according to the method proposed in [117]. The combination between the plug-in BoneJ [118, 119] and the software Amira (Thermo Fisher Scientific, Waltham, USA) was used to generate the images and analyse them. The sample extracted and analysed was a volume of 1000 pixels per side (8 mm).

3.5.6 Scanning electron microscopy (SEM)

SEM imaging for morphological analysis of polyurethane scaffolds was performed as follows: each sample was provided with a metallic coating using gold sputtering for 60 s and a current of 25 mA (Q150R ES, Quorum Technologies). SEM (EVO MA15, Zeiss Instrument) scans were performed by setting a beam voltage of 5 kV and a probe current of 200 pA.

3.5.7 Mechanical testing

All mechanical tests were performed by our colleagues at the BioRobotics Institute (SSSA, Pisa) using the Instron Series 4460 mechanical loading structure paired with a load cell of ± 10 N. Four independent specimens were tested for every condition analysed.

Uniaxial compression

Uniaxial compression tests were performed on PU and PU+shell scaffolds with a compression velocity of 2 mm/min. The stress (σ) was evaluated as the ratio between the force measured by the load cell and the undeformed specimen cross-section. Strain (ε) was determined as the ratio between the crosshead displacement and the specimen height. Young's moduli were obtained considering the initial elastic region of the stress-strain curve (strain up to 10 %) and calculated as follow:

$$E = \frac{\sigma}{\varepsilon} \quad (3.1)$$

PU samples and PU+shell samples tested in wet conditions were first immersed in PBS for 24 h at 37°C. Then, loading was performed in a recipient filled with PBS while keeping the sample completely submerged.

Cyclic dynamic compression

Cyclic dynamic compression tests were performed on PU+shell scaffolds in wet conditions, maintaining a frequency of 1 Hz for 1'500 cycles. Compression was tested at 5 % and 10 % calculated relatively to the initial scaffold heights. Softening/hardening degree (SD) was calculated as the ratio between the difference of the last and initial stress, over the initial stress as follow:

$$SD = \frac{(\sigma_f - \sigma_i)}{\sigma_i} \text{ x } 100 \quad (3.2)$$

Cyclic dynamic extension

Cyclic dynamic extension tests were performed on TMT devices filled with DMEM for 24h at 37°C. Frequency was maintained at 1 Hz for 10'000 cycles and compression was set at 15 % relative to the initial scaffold heights. Softening/hardening degree (SD) was calculated as specified in **Formula 3.2**. Integrity checkpoints were set at 1'000, 5'000, and 10'000 cycles. They were done by gently tap the TMT with filter

paper.

3.5.8 Biodegradation studies

PU samples for biodegradation studies were kept immersed in DMEM supplemented with 10% FBS and 1% p/s in the incubator (37°C, 100 % humidity, and 5 % CO_2). Checkpoints for further analysis were set at 30 and 60 days. The medium was changed every 48 hours. Four specimens for each condition were used.

Weight variation
Each sample was measured in dry state at day 0 (W_0) and at the specific time point (W_t) after drying. To do this, PUs were removed from medium, rinsed in distilled water, and dried at 37°C for 24 h. Weight variation was calculated as follow:

$$W\% = \frac{(W_t - W_0)}{W_0} \text{ x } 100 \quad (3.3)$$

Young's modulus variation
Each sample was measured tested in wet conditions with uniaxial mechanical compression as reported in **Chapter 3.5.7**. Young's modulus was assessed at day 0 (E_0) and at the specific time point (E_t). Young's modulus variation was calculated as follow:

$$E\% = \frac{(E_t - E_0)}{E_0} \text{ x } 100 \quad (3.4)$$

3.5.9 Permeability measurements

Scaffold permeability was assessed as described by Darcy's law:

$$k = \eta \frac{Q}{A} \frac{L}{\Delta P} \quad (3.5)$$

where k is the intrinsic permeability (m^2), η is the kinematic viscosity of the fluid (Pa×s), Q is the flow rate (m^3/s), A is the scaffold cross-sectional area (m^2), L is the scaffold total length (m), and ΔP is the pressure drop over the scaffold (Pa).
The constant pressure gradient method was adopted for assessing the experimental scaffold permeability, using the set-up depicted in **Figure 3.5.5**. The volumetric flow rate Q of water (ρ_{water} = 998 kg/m3 and η_{water} = 8.9×10^{-4} Pa×s) through the scaffold was measured as the mass of water crossing the scaffold over 60 s.

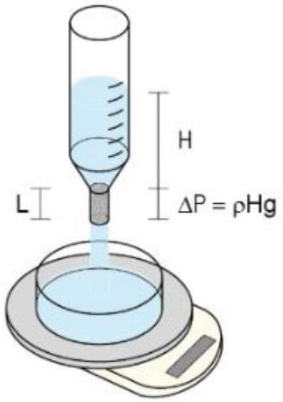

Figure 3.5.5: Schematic representation of the experimental set-up used for permeability measurements. H is the water column height g is 9.81 m/s^2.

3.5.10 Computer simulations

All computer simulations were performed by our colleagues at the BioRobotics Institute (SSSA, Pisa).

Myotubes contraction
The PU-myotubes system was modelled as in **Figure 3.5.6**. Pores

diameter was extracted from µCT (mean value of 637.0 ± 188.7) and myotubes diameter (30 µm) was taken from literature. Contractile force (F_c) was calculated as follow:

$$F_c = \frac{F_m}{A_m} \text{ x (Cell occupancy) x } (A_s) \quad (3.6)$$

where F_m is the contractile force of C2C12 myotubes found in the literature (from 0.1 to 10 µN) [120], A_m is the total myotubes area, cell occupancy is the pore area percentage occupied by myotubes (17.6 %), and A_s is the PU+shell cross-section area (9 mm).

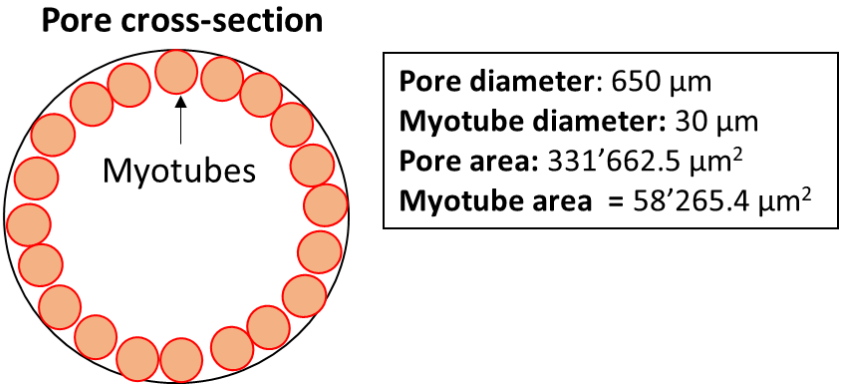

Figure 3.5.6: Schematic representation of PU-myotubes system for used for simulations.

The PU+shell system was modelled as a simple spring system. And displacement (ε) was calculated as the ratio of contractile force (F_c) and the PU+shell elastic constant (K_s = 0.09 N/mm) obtained from uniaxial compression analysis:

$$\varepsilon = \frac{F_c}{K_s} \quad (3.7)$$

Fluid flow

Fluidic computational analysis was simulated on the PU scaffold structure obtained from μCT (**Chapter 3.5.5**) using COMSOL 5.6 to mesh the fluid volume and to solve the steady-state Navier-Stokes equations for laminar flow. A fixed pressure gap (1 bar) was imposed between the extremities of the model, and no-slip conditions were imposed at the channel walls and the scaffold walls. The fluid considered was the cell culture medium DMEM (Dulbecco's Modified Eagle Medium) with 5% FBS (Fetal Bovine Serum) (density $\rho = 1002$ kg/m^3 and dynamic viscosity $\mu = 8.62\ 10^{-4}$ Pa×s). Three flow rates (Q) were considered at the inlet (0.022, 0.22, and 2.2 ml/min).

Local wall-shear stress (WSS) was calculated on an RVE (representative volume elements) placed at the center of the PU scaffold. RVE had an area of 0.9 mm^2 and a length equal to that of the scaffold (8 mm).

Velocity distributions at the interface between the polyurethane and the channel inside the tendon-like structures (diameter = 3 mm) were evaluated on a scaffold with an area equal to that of the scaffold (8 mm x 8 mm = 64 mm^2) and a length of 1.6 mm.

Electrical stimulation

The electrical field experienced by the cells was modelled with a finite element method software (COMSOL Multiphysics v. 5.3) to assess the homogeneity of the field across the whole PU-based scaffold. The simulative environment included the Pt electrodes, the scaffold, and the surrounding culture medium (MDM). A uniform potential was set on the surface of the electrodes (5 V at the positive electrode, 0 V at the ground electrode), while an insulated boundary condition was applied to the external surfaces of the well (radius: 1.9 cm, height: 1.2 cm).

3.5.11 Cell cultures

The C2C12 murine skeletal myoblasts cell line was used for all *in vitro* experiments. C2C12 were subcultured in growth medium (GM): DMEM, supplemented with 10 % fetal bovine serum (FBS), 1 %

glutamine, 1 % amphotericin, and 1 % Penicillin-Streptomycin. In differentiation medium (DM), FBS was substituted with HS at 5 %.
Prior usage for cell culture experiments, PU scaffolds (height ≈ 5 mm, diameter ≈ 9 mm) were always incubated with 70 % EtOH for 30 min, rinsed with phosphate-buffered saline (PBS) and treated with UV light for 30 min.
All reagents and cell lines were purchased from Sigma-Aldrich.

3.5.12 Dynamic cell seeding

PU scaffolds were inserted in a perfusion chamber (P3D-10 perfusion chambers from EBERS Medical Technology SL). Two perfusion chambers with a scaffold in each were connected by a "U" tube in series and an mp6-QuadKey with an Arduino interface was used in order to control four mp6 piezoelectric diaphragm micropumps in parallel (Bartels Mikrotechnik GmbH). Cells were seeded on the scaffolds with a velocity of 2 mm/s (imposing a flow rate of 7 ml/min) and by changing direction every 12 s for a total duration of 1 h. During the seeding procedure, the setup was kept in a controlled environment at 37 °C. The seeded scaffolds were finally transferred into 48-multiwells and placed in the incubator for culturing.

3.5.13 Plasma oxygen surface activation

PU samples were treated with O_2 plasma (Tucano Plasma RF 13.56 MHz, Gambetti) for 60 s at 50 W. After plasma treatment, samples were functionalized with either LMN (10 µg/mL) or FN (25 µg/mL). Treated samples were immersed in an overall volume of 500 µL of protein solution (diluted in PBS) and incubated at 37 °C for 3 h.
Non-functionalized samples were only treated with plasma oxygen before cell seeding and are referred to as plasma PU.

3.5.14 Proliferation assay

250’000 cells were dynamically seeded in each scaffold as described in **Chapter 3.5.12**. Cell proliferation was quantitatively assessed by analyzing the DNA amount after 24, 48, and 72 h of culture in GM. Functionalized scaffolds were compared to bare PU, used as control. Four independent samples were analysed for each experimental condition and for each time point. First, each sample was rinsed twice with PBS. Cells on samples were lysed in distilled water at the desired time point and the DNA amount in the cell lysates was measured by using the PicoGreen kit (Invitrogen Co., Carlsbad, CA, USA), following the manufacturer’s instructions. DNA amount was proportional to fluorescence intensity, which was measured on a VICTOR X microplate reader (excitation wavelength: 485 nm; emission wavelength: 535 nm).

3.5.15 Myotube electrical stimulation assay

Approximately 2.5 million cells were seeded for each PU scaffold as described in **Chapter 3.5.12**. A total of four samples were seeded, one for each experimental condition. On the fourth day of proliferation, myoblast differentiation was triggered by switching to DM (**Figure 3.5.7**). Electrically stimulated PU samples were then placed perpendicularly between two platinum (Pt) electrodes (2.7-cm distant) and cells were continuously stimulated from day 8 to day 10 (48 h) at ~ 0.2 V/mm (5 V, 1 Hz, 5 ms).

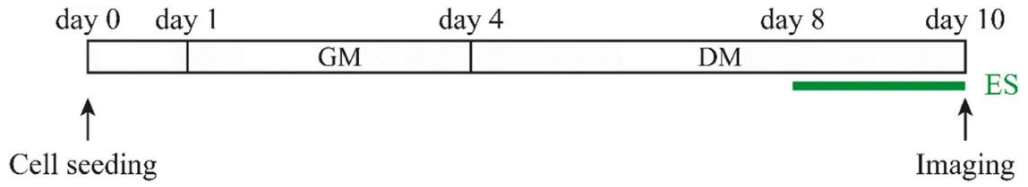

Figure 3.5.7: Schematic representation of the electrical stimulation experimental protocol to assess growth and myotube formation.

3.5.16 Polydopamine coating protocol

PU samples were placed in a 48-multiwell a were immersed in 450 µl of a 2 mg/ml dopamine buffer solution (10 mM Tris-HCl at pH 8.5). Sterile tweezers were used to gently squeeze the scaffolds so to let them impregnate with dopamine buffer solution. After that, the multiwell was sealed with parafilm and stored at 37 °C overnight. The day after samples were washed with Milli-Q water 5 times (waiting 2 min after every rinse) and dried under the hood for 1 hour. At this point, they were functionalized with FN (2 µg/cm^2). Samples were immersed in an overall volume of 500 µl of protein solution and incubated at 37 °C for 4 h. After this, PU scaffolds were washed with Milli-Q water and dried under the hood for 1 hour. The last step consisted in seeding onto the scaffolds a cell suspension of 250'000 cells in 300 µl of medium by using a pipette. After 2 hours of incubation at 37 °C, 200 µl of medium were added (for a total of 500 µl).
The seeded scaffolds were maintained in culture for 3 days using GM. Samples coated with FN were also cultured for a total of 5 days, switching to DM on the fourth day.
Untreated PU scaffolds are referred to as bare PU, whereas those just treated with dopamine solution are referred to as dopa PU.

3.5.17 Staining and imaging

For f-actin and DNA staining, PU samples were rinsed twice with PBS and fixed in a 4 % paraformaldehyde solution for 20 minutes at room temperature. Afterward, samples were rinsed with PBS and permeabilized with a 0.1 % Triton X-100 solution for 15 minutes at room temperature. Samples were then washed in PBS and a 3% bovine serum albumin (BSA) solution was added for 20 min at RT. Finally, PU scaffolds were washed again in PBS and incubated for 1 hour at RT in the dark with the staining solutions: Tetramethylrhodamine (TRITC)-Phalloidin (50 µg/ml) and/or Hoechst dye (dilution 1/200 in PBS) were

used as staining solutions. The staining process was followed by a wash with a 0.2% TWEEN 20 solution and PBS.
All reagents were purchase from Sigma-Aldrich.
Epifluorescence and confocal laser scanning microscopy (C2S Nikon) were performed on stained cells. 3D reconstruction was carried out through the NIS element software (Nikon). Maximum diameter and length of the myotube bundles were measured with the NIS element software.

3.5.18 Statistical Analyses

Data analyses were performed using the GraphPad Prism 8 software. Values are always shown as mean value ± standard deviation unless otherwise noted. Regarding box plots, boxes show the median value, 25th and 75th quartile ± Tukey whiskers (1.5 times the interquartile range, IQR).
For both DNA content and myotube bundles sizing analysis a Kruskal-Wallis test with Dunn's post hoc test for multiple comparisons was performed. Significant threshold was set at 5% and computing a two-tailed p value.

3.6 Publications

Annals of Biomedical Engineering (© 2019)
https://doi.org/10.1007/s10439-019-02419-9

BMES BIOMEDICAL ENGINEERING SOCIETY

Original Article

Combined Effects of Electrical Stimulation and Protein Coatings on Myotube Formation in a Soft Porous Scaffold

FEDERICA IBERITE,[1,5] IRINI GERGES,[2] LORENZO VANNOZZI,[1,5] ATTILIO MARINO,[3] MARCO PIAZZONI,[4] TOMMASO SANTANIELLO,[4] CRISTINA LENARDI,[4] and LEONARDO RICOTTI[1,5]

[1]The BioRobotics Institute, Scuola Superiore Sant'Anna, Piazza Martiri della Libertà 33, 56127 Pisa, Italy; [2]Tensive S.r.l, Via Timavo 34, Milan 20124, Italy; [3]Smart Bio-Interfaces, Istituto Italiano di Tecnologia, Viale Rinaldo Piaggio 34, Pontedera, Pisa 56025, Italy; [4]Interdisciplinary Centre for Nanostructured Materials and Interfaces (CIMaINa) and Department of Physics, Università degli Studi di Milano, Via Celoria 16, Milan 20133, Italy; and [5]Department of Excellence in Robotics & AI, Scuola Superiore Sant'Anna, Piazza Martiri della Libertà 33, 56127 Pisa, Italy

(Received 11 July 2019; accepted 30 October 2019)

Associate Editor Sundar Cohen oversaw the review of the article.

Abstract—Compared to two-dimensional cell cultures, three-dimensional ones potentially allow recreating natural tissue environments with higher accuracy. The three-dimensional approach is being investigated in the field of tissue engineering targeting the reconstruction of various tissues, among which skeletal muscle. Skeletal muscle is an electroactive tissue which strongly relies upon interactions with the extracellular matrix for internal organization and mechanical function. Studying the optimization of myogenesis *in vitro* implies focusing on appropriate biomimetic stimuli, as biochemical and electrical ones. Here we present a three-dimensional polyurethane-based soft porous scaffold (porosity ~ 86%) with a Young's modulus in wet conditions close to the one of natural skeletal muscle tissue (~ 9 kPa). To study the effect of external stimuli on muscle cells, we functionalized the scaffold with extracellular matrix components (laminin and fibronectin) and observed an increase in myoblast proliferation over three days. Furthermore, the combination between laminin coating and electrical stimulation resulted in more spread and thicker myotubes compared to non-stimulated samples and samples receiving the single (non-combined) inputs. These results pave the way to the development of mature muscle tissue within three-dimensional soft scaffolds, through the combination of biochemical and electrical stimuli.

Keywords—Three-dimensional scaffold, Biophysical stimulation, Skeletal muscle, Tissue engineering, Polyurethane scaffold.

ABBREVIATIONS

3D	Three-dimensional
DMEM	Dulbecco's Modified Eagle's Medium
DMSO	Dimethylsulfoxide
ECM	Extracellular matrix
ES	Electrical stimulation
EtOH	Ethanol
FBS	Fetal bovine serum
FN	Fibronectin
HMDI	Hexamethylene diisocyanate
IQR	Interquartile range
LMN	Laminin
MDM	Myoblast differentiation medium
MGM	Myoblast growth medium
MSM	Myoblast seeding medium
PBS	Phosphate buffered saline
PEG6K	Polyethylene glycol 6000 g/mol
Pt	Platinum
PU	Polyurethane
SEM	Scanning electron microscopy
SM	Skeletal muscle
SMTE	Skeletal muscle tissue engineering
TRITC	Tetramethylrhodamine

INTRODUCTION

Leaving two-dimensional cell culture systems and working in three-dimensional (3D) ones has the potential to recapitulate more reliably the complexity

Address correspondence to Federica Iberite, The BioRobotics Institute, Scuola Superiore Sant'Anna, Piazza Martiri della Libertà 33, 56127 Pisa, Italy. Electronic mail: federica.iberite@santannapisa.it

Published online: 07 November 2019

Effects of the 3D Geometry Reconstruction on the Estimation of 3D Porous Scaffold Permeability*.

Daniele Guarnera, Federica Iberite, Marco Piazzoni, Irini Gerges, Tommaso Santaniello, Lorenzo Vannozzi, Cristina Lenardi and Leonardo Ricotti

Abstract **- 3D scaffolds for tissue engineering typically need to adopt a dynamic culture to foster cell distribution and survival throughout the scaffold. It is, therefore, crucial to know fluids' behavior inside the scaffold architecture, especially for complex porous ones. Here we report a comparison between simulated and measured permeability of a porous 3D scaffold, focusing on different modeling parameters. The scaffold features were extracted by micro-computed tomography (μCT) and representative volume elements were used for the computational fluid-dynamic analyses. The objective was to investigate the sensitivity of the model to the degree of detail of the μCT image and the elements of the mesh. These findings highlight the pros and cons of the modeling strategy adopted and the importance of such parameters in analyzing fluid behavior in 3D scaffolds.**

I. Introduction

The design of three-dimensional (3D) scaffolds is crucial for an effective tissue engineering of musculoskeletal tissues. To achieve 3D constructs, a possible strategy consists of developing microporous matrices. The internal architecture of these materials (mainly their porosity, pore size, and pore interconnectivity), influences the mechanical and mass transport properties of porous 3D scaffolds [1, 2]. These features, together with the pore distribution and orientation, determine if the scaffold permits a flow throughout the pores. The property encompassing all these features is known as permeability, a parameter that is independent of the fluid permeating the material [3, 4].

An appropriate permeability is crucial to enable nutrients transport, waste removal, and thus cell survival and growth within the scaffold [5 - 7]. Scaffold permeability is directly linked to the scaffold architecture, which can strongly influence cell behavior: it is known that pore size and scaffold porosity can affect cell viability and proliferation *in vitro* [8], or resident cell colonization and migration *in vivo* [9]. Various methods exist for the fabrication of porous scaffolds, including electrospinning, salt leaching and gas foaming. Reliable virtual models often help an appropriate control of these processes [10].

One of the most effective strategies to assess the scaffold internal architecture is the micro-computed tomography (μCT), which is non-invasive and non-destructive. μCT generates a sequence of high-resolution images of a sample through an X-ray source. The post-processing imaging allows a 3D reconstruction of the sample and the consequent analysis of the aforementioned architecture-related parameters. Furthermore, the 3D images are a key input for computational fluid-dynamic (CFD) simulations on the scaffold.

CFD simulations have been recently used to provide quantitative predictions on scaffold properties, such as permeability and wall shear stress [11-14], but also to predict the impact of such parameters on cell behavior [15, 16]. Computational models have been also used to optimize the internal structure of the scaffold from the mechanical properties standpoint and in the evaluation of the structural aspects on the flow parameters [17, 18]. However, CFD analyses of 3D scaffolds are often prohibitive from the computational cost viewpoint, when μCT-derived architectures must be managed, especially due to the scaffold's complex geometry. Indeed, the outputs of μCT are usually large-size files that require time-consuming pre-processing activities. μCT output files can require hard efforts in reducing the file size and solving the geometry errors that arise from complexity reduction. In addition, meshing, computation, and post-processing times must be taken into account in the case of highly non-homogeneous scaffolds [19, 20]. To overcome these issues, computational analyses are sometimes focused on one or more representative volume elements (RVE) [19, 21]: this strategy allows for shorter simulation times, but it could affect the final result when the pre-processing procedures are not accurately investigated.

The aim of this work is to investigate the RVE-CAD degree of the finish, the spatial position and size of the meshing elements, and to evaluate the effect of these features on the predicted permeability with respect to the measured one.

II. Materials and Methods

A. Scaffold fabrication

Mixture A (polyols): 16.00g PEG 2000 (Sigma Aldrich, 99%, 79.46 pphp); Glycerol 1.72g (Sigma Aldrich, ≥99% (GC), 8.57 pphp) and 2.4g MilliQ water (11.96 pphp).

Component B (polyisocyanate): 63.87 g Tolonate™ X FLO 100 (Vencorex, ≥99%). NCO index = 100.

Component C (catalyst): 0.38 g Dibutiltindilaurate DBTL (Sigma Aldrich, ≥ 96.0 %). %DBTL = 0.5% w/w.

* This work received both financial and technical support by INAIL, in the framework of the project MIO-PRO (Engineered patient-specific muscles for the restoration of myoelectric channels and prosthesis control).

D. Guarnera, F. Iberite, L. Vannozzi and L. Ricotti are with Scuola Superiore Sant'Anna, The BioRobotics Institute, Pontedera, Italy (corresponding author email: daniele.guarnera@santannapisa.it).

I. Gerges is with Tensive s.r.l., Milan, Italy.

M.Piazzoni, T. Santaniello and C. Lenardi are with University of Milan, Milan, Italy.

SECTION 2.

4.

ZanzaRaft: Smart Delivery Hydrogel System for Environmental Control of Invasive Mosquito Species

4.1 Scientific Background

4.1.1 Harmful insects of agricultural and medical interest

Insects are among the most common and widespread organisms on the planet due to their marked adaptation ability, representing about 60 % of all terrestrial animals [121]. The mutual relationship existing between insects and the ecosystem where they live is so strong that they can be considered a bioindicator of its health [122]. As a matter of fact, insects are tightly linked to their food source (mainly of vegetal origin, but also animal), whereas the environment, for example, owes to insects the possibility of plant reproduction through the phenomenon of pollination [123].

The man-insect relationship, on the other hand, is much more recent and limited, if we consider that only 1% of about 5-10 million insect species interact with humans, directly or indirectly. During the last centuries, with the advent of a series of social and economic problematics which include food demand associated with population growth, urbanization, transportation of products and people, and the trend towards monoculture, has emerged the need of increasing the number of beneficial insects and/or decreasing the number of those harmful [124].

It has been observed indeed that insects' activity can have a double-sided effect on both agriculture production and public health. On one hand, insects can provide benefits through ecosystem services such as pollination or predation/parasitism towards even more harmful parasites [125], on the other hand, they can be the cause of significant economic losses (e.g. crops damaging) or public health issues (e.g. spreading of vector-borne diseases) [126, 127].

The scenario is often complex to untangle, as insects can play the role of prey, predators, or parasites, as well as recyclers of decaying matter. In order to achieve an overall distinct benefit, both in an agrarian and a health context, it is therefore always necessary to carefully and deeply

evaluate the subtle balance that exists between useful and harmful organisms in the ecosystem considered.
Harmful organisms, that are capable of causing damage to crops, food-related products, and to public health, are commonly referred to as "pests". Pests are species that have developed and optimized a parasitic ability toward a specific host, be it a plant or an animal, to the point of weakening or, in some cases, death [128].

Vectors and vector-borne diseases

An important category in the context of pests is represented by vectors, organisms capable of transmitting pathogens of various diseases to plant and animal hosts.
In the plant field, for example, vector-related infectious plant diseases have been documented both in anthropized and natural ecosystems. The transmission of the related etiological agents occurs thanks to organisms belonging mainly to two orders, the *Thysanoptera* and the *Hemiptera*. This last one includes the families of plant lice (*Aphidoideae*) and whiteflies (*Aleyrodidae*), which are among the phytomitic insects (i.e. organisms that feed on plant sap) of greatest economic interest, due to their cosmopolitan diffusion and the ability to carry numerous pathogens, mainly viral [129, 121].
Concerning zoonotic infectious diseases (diseases transmitted between animals and humans) and anthroponoses (diseases transmitted between human beings), the majority of responsible vectors are hematophagous insects which, during blood meals, ingest the microorganisms from an infected host and transmit them to a new one, through the next meal. These vectors are involved in the transmission of various diseases such as malaria, yellow fever, typhus, plague, dengue fever, various forms of encephalitis, relapsing fever, river blindness, lymphatic filariasis, sleeping sickness, and countless other debilitating or even fatal diseases. Estimates collected by the World Health Organization (WHO) show that more than 17 % of cases of infections in humans, responsible for over 700'000 deaths a year, are attributable to pathogens transmitted by vector arthropods [130].

In the current historical context, vector-borne diseases are a serious problem, especially because of the global changes we are witnessing. Travels, global trades, and unplanned urbanization are having a significant impact on the transmission of pathogens, making the original transmission season longer or more intense, therefore causing the onset of diseases even in countries in which had never been recorded before [131]. Added to this, there are changes in agricultural practices, due to variations in temperature and rainfalls, which can further favour the spread of vector-borne related illnesses. In order to contain these problems, certified the impossibility of directly controlling the propagation of diseases by targeting the aetiological agent, since vaccines are often not available, the most effective strategy still relies on controlling the density of the vector.

4.1.2 Mosquitoes

Life cycle

Mosquitoes are flying insects belonging to the family *Culicidae*. Their life cycle goes through four separate and distinct stages: (i) egg; (ii) larva, (iii) pupa, (iv) and adult (**Figure 4.1.1**).

Something all mosquitoes have in common is that the young forms' life is confined to water. Depending on the species, eggs can be laid on the water surface, or deposited in spots where water is collected later as a result of floods or rain. Eggs usually hatch into larvae within 48 hours. In most species, larvae hang at the surface of the water and breathe through a snorkel-like siphon on their abdomen. They feed on microorganisms and organic matter in the water in order to develop. Larvae mature in 4 to 10 days, passing through four growth stages until they transformed into pupae. The pupal stage is a resting, non-feeding stage of development, even though pupae are mobile, responding to light changes and tumbling with a flip of their tails towards the bottom or protective areas. The pupal stage may last from 1 to 10 days, or even more, depending on the temperature and the mosquito species involved. After this, with a process is similar to the metamorphosis seen in

butterflies, the pupa becomes an adult. The newly emerged adult mosquito rests on the surface of the water for a short time to allow itself to dry and all its body parts to harden [132].

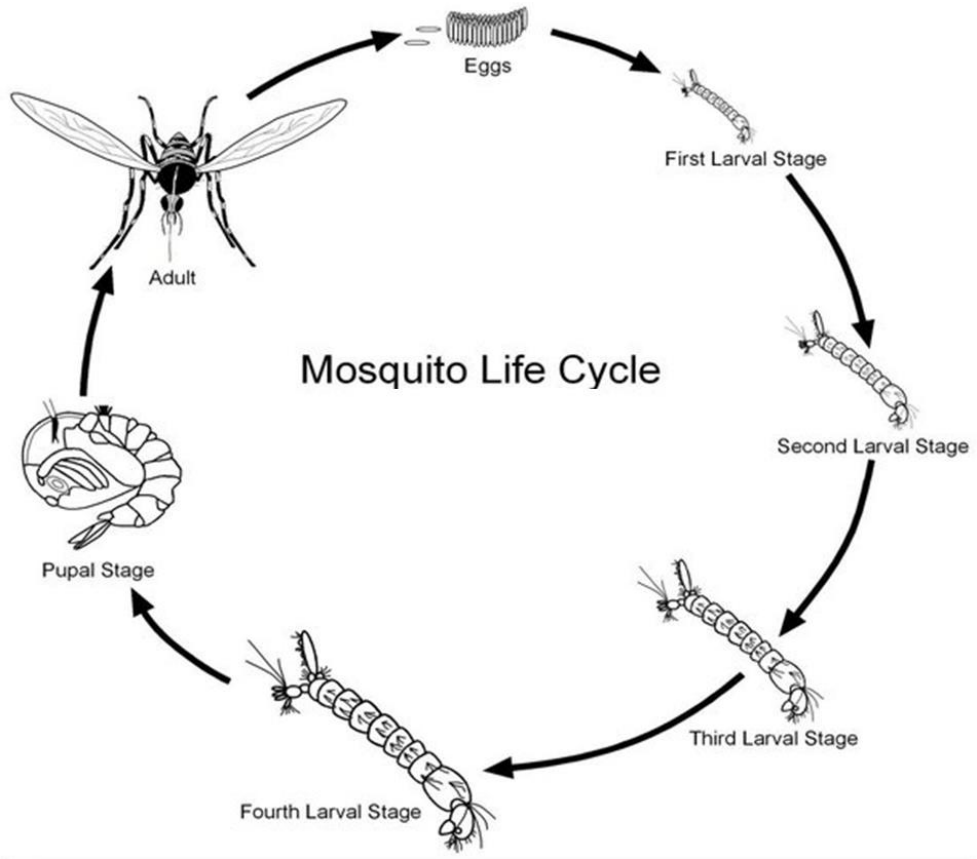

Figure 4.1.1: Mosquitoes' general life cycle. Adapted from [133]

Mosquitoes-borne diseases

Female mosquitoes feed on blood to produce their eggs, which can affect people and animals directly or indirectly. In the first case, the cause of discomfort, is the physical act of feeding that induces mild allergic reactions (such as swelling and itching) into their hosts, due to the injection of irritant salivary fluids. However, much more serious damages can arise, when mosquitoes act as vectors of pathogenic organisms that can indirectly affect people and animals (**Figure 4.1.2**)

[132]. While transmitting the disease, the vector mosquito is not damaged by the presence of the pathogen inside its body. It has been observed indeed that mosquitos are able to defend themself thanks to the presence of a microbiome and the activation of their innate immune system [134]. Infection in humans therefore can only occur when the female takes a blood meal and while her immune system is still in the process of destroying the harmful moiety of the pathogen.

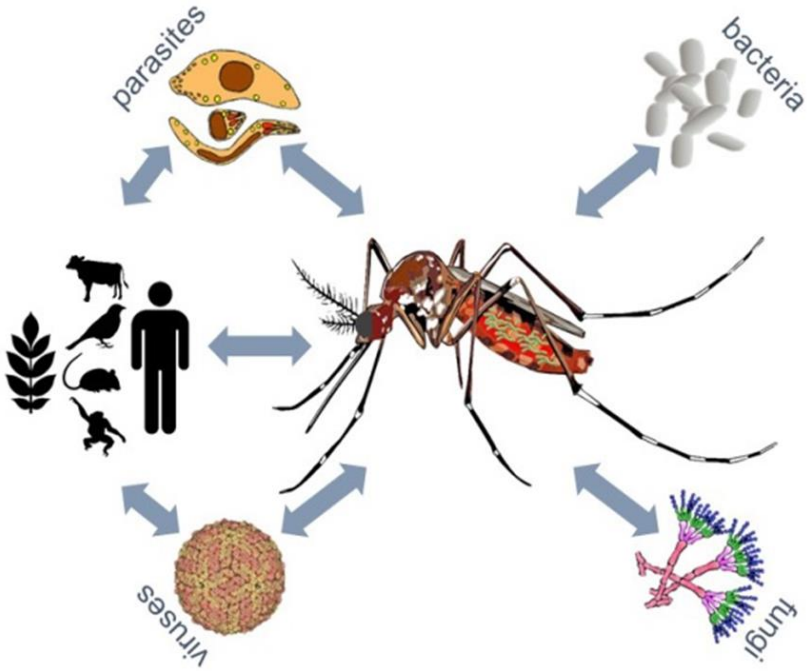

Figure 4.1.2: Schematic representation of mosquito-borne diseases transmission cycle.

Among the most infesting and harmful insect pests, mosquitoes play a role of considerable importance in terms of public health concerns. They are considered indeed among the most lethal organisms for humans. According to some estimates, these arthropods are responsible for over a million deaths a year, thanks to their ability to transport and spread pathogens of various kinds. Diseases transmitted by mosquitoes and

caused by agents such as bacteria, viruses, or parasites include dengue, yellow fever, West-Nile, chikungunya, zika, filariasis, and malaria [130]. Moreover, illnesses transmitted by mosquitoes have assumed a global priority also due to the frequent resurgence of large epidemics and the unprecedented geographical expansion which took place in recent decades. As proof of this, malaria, transmitted by mosquitoes exclusively of the *Anopheles* genus, was the cause of 435'000 deaths and more than 219 million cases in 2017; dengue has increased its incidence 30-fold in the past 30 years alone, and anomalous outbreaks of *Aedes* mosquito-borne diseases such as zika, dengue, chikungunya, and yellow fever have been reported in several countries [135].

Mosquitoes of European public health interest

Among the large family *Culicidae*, there can be outline two major mosquito species of particular relevance for public health in Europe: (i); *Ae. albopictus*; (ii) *Cx. pipiens*. The associated diseases are listed in **Table 4.1.1**.

The species *Ae. albopictus* (also known as tiger mosquito) has the ability to act as a vector for many pathogens like the dengue virus [136] and dirofilarial worms [137]. Moreover, recent studies suggest its possible contribution to Zika virus outbreaks [138]. *Ae. albopictus* is now listed as one of the top 100 invasive species by the Invasive Species Specialist Group [139]. It is particularly well established in Italy (the most heavily infested country in Europe), [140] in all areas with an altitude less than 600 m above sea level and, in general, in many urban areas. In 2006-2007 there was an outbreak of chikungunya virus linked to this mosquito.

Cx. pipiens is also another dominant mosquito species present in several urban areas of Europe [141]. It is among the vectors of several arboviruses, such as those causing West Nile disease, St. Louis encephalitis, Rift Valley fever, and Japanese encephalitis, and is the primary vectors of lymphatic filariasis [142].

Mosquito vectors	Diseases	Pathogens
Aedes 	▪ Chikungunya	- Virus
	▪ Dengue	- Virus
	▪ Lymphatic filariasis	- Parasite
	▪ Rift Valley fever	- Virus
	▪ Yellow Fever	- Virus
	▪ Zika	- Virus
Culex 	▪ Japanese encephalitis	- Virus - Parasite
	▪ Lymphatic filariasis	- Virus
	▪ West Nile fever	

Table 4.1.1: List of diseases and related pathogens caused by the mosquito species *Ae. albopictus* and *Cx. pipiens.*

4.1.3 Control of harmful mosquitoes

The control of mosquitoes is a fundamental and essential element to prevent or contain the spread of etiological agents and related diseases. Considering, in fact, that such vectors have a very rapid multiplication capacity both indoors and outdoors, it is essential to implement efficient control and eradication strategies, which act specifically when the first symptoms arise or preventively in areas of greater risk [143]. The methods and protocols used for the control of these vectors can be of various kinds and can be grouped into three categories: (i) physical; (ii) chemical; (iii) biological.

Physical methods include several techniques targeting mosquitoes at different developmental stages: larvae control is done by reducing the number of stagnant waters and by the usage of ovitraps (tools to entrap

mosquitoes' eggs) at the breeding sites. On the other hand, the main physical tools to control mosquitoes at the adult stage are mosquito nets. Biological methods are based on the introduction of natural enemies or alien species and/or on the dispersion of pathogens or toxins produced by pathogens [144]. Concerning biological methods, larvae control is carried out using weapons of microbial origin. *Bacillus thuringiensis var. israelensis* (Bti) and *Bacillus sphaericus* (Bs) are commonly employed biological weapons able to selectively kill mosquito larvae, with basically null effect on non-target organisms. This specific effect is due to the fact that larvae, apart from having the required molecular recognition sites, also possess an alkaline intestinal tract that allows the activation of microbial prototoxins [145]. Despite the efficacy of such biological compounds, their applicative potential is limited because of the low residual activity which implies repetitive administrations with the consequence of rising costs [146]. For this reason, biological control methods are required to be implemented with the chemical one.

Chemical control is the most utilised method at the present day. It is done at the larvae stage by administering powerful chemical compounds (e.g. organophosphorus) with long-lasting residual activity, but also heavily toxic, at the point of confining their usage only in already polluted waters. An alternative (or preferably reinforcing) strategy consists of biodegradable oils to be applied on water surfaces, with the effect of inducing larvae death by anoxia. Synthetic larvicides are classified as useful tools to control mosquitoes [147], but their usage is not recommended in rural areas [148] and therefore they have to be combined with methods that control mosquitoes at the adult stage. In this context, most of the chemical compounds in use today are neurotoxic products able to affect the mosquito's nervous system causing its rapid death [149], but without affecting more complex organisms like mammals [150]. Despite the good premises, these products can only be used at a domestic level (e.g. vaporizers) because of complications brought to light only in the last decades. As a matter of fact, it has been demonstrated that a prolonged bulk use of such compounds can have negative effects on harmless insect species (like bees), natural mosquitoes predators, and even on the fish fauna.

Environmental pollution and resistance phenomena

In many cases, the impact of interventions based on the massive use of synthetic insecticides has met with extraordinary success. An example is the halving, between 2000 and 2015, in the number of deaths due to malaria transmitted by *Anopheles* mosquitoes [151]. However, the considerable increase in the availability of new products and services for pests' control, must be counterbalanced with a worrying increase in environmental pollution and the onset of resistance phenomena.

Related to the first concept, the introduction on the market of a large number of new chemical compounds does not seem to have gone hand in hand with the study of environmental toxicology. This phenomenon is certainly partially due to the delayed effect that some substances had on the environment, exhibiting negative consequences only years after their administration [152].

Concerning the onset of resistance to pesticides, is mainly attributed to a phenomenon known as bioaccumulation (i.e. the gradual accumulation of substances in an organism). When a target species is continuously exposed to a determined xenobiotic, even at low concentrations, it underwent a continuous selective pressure that ultimately will lead to the development of resistances of various kinds. For example, it can lead to the selection of sub-populations with greater efficiency in the detoxifying xenobiotic substances (i.e. metabolic resistance), with mutations arose within the insecticide target site, thus preventing the ligand-receptor binding (i.e. resistance at the target site), or even, that as develop a danger recognition system which leads them to stop feeding or to move away from the area of administration (i.e. behavioural resistance) [153].

Smart delivery systems

The concept of using polymers for insecticides administration goes back to the early '90s and since then stimulated a great deal of research focusing on the development of formulations suitable for this purpose [154]. Concerning the environmental control of mosquito larvae, polysaccharides (alginate, chitosan, or gelatin) and cellulose-based

hydrogels are the most investigated materials, due to their intrinsic hydrophilic nature, biocompatibility, and possibility of tuning mechanical properties [155]. In particular, smart delivery systems (i.e. engineered technologies for the targeted delivery and/or controlled release of substances) made of hydrogels, could help overcoming some of the above-mentioned problematics in controlling harmful mosquitoes for the following reasons. First of all, the gel matrix acts as a protective scaffold for the insecticide, protecting it from environmental cues that can potentially compromise its stability and functionality. A prolonged residual activity allows in turn to use fewer amounts of the chemical, therefore reducing both production costs and, most importantly, bioaccumulation into the environment and in the target species. Moreover, since compound delivery can be limited at the breeding site it would further minimize environmental pollution.

4.2 Aim of the Project

In this work, a novel smart delivery hydrogel system for in-field control of mosquito larvae is optimized and validated. The operational principle of the device relies on the use of a biocompatible macro-porous hydrogel, provided with a biopesticide (*Bacillus thuringiensis* var. *israelensis* - Bti) physically incorporated into its polymeric matrix. Also, yeast colonies (*S. cerevisiae*) will be embedded into the hydrogel during its synthesis in order to attract the larvae towards the capsules. A controlled administration of the biological compounds will take place mainly by material erosion and will be confined only at the breeding site where the hydrogel tablets will be located. Upon ingestion by the larvae, the insecticide will respond to the characteristic basic pH of its intestinal tract, triggering a lethal burst of Bti activation. The gel will be placed in-field into urban areas of interest (e.g. fountains, manholes, flowerpot dishes, small ponds) as a floating biodegradable raft. A schematic of the operating mechanism of the smart delivery system is reported in **Figure 4.2.1**.

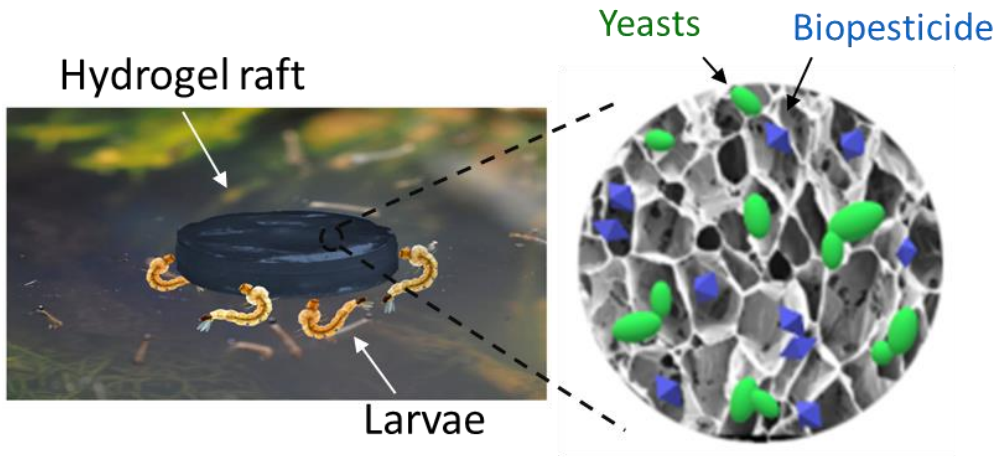

Figure 4.2.1: Illustration of the smart delivery hydrogel system.

This project is a collaboration between our research group (CIMaINa; Physics department, UniMi) and the research group of Professor Claudio Bandi (Bioscience department, UniMi) and it is being financed by a PRIN (progetti di ricerca di rilevante interesse nazionale).
In 2021 we participated in the scouting program of the University of Milan, Seed4Innovation, carried out with the UniMi Foundation and in collaboration with Deloitte and Bugnion. Seed4Innovation is designed to accelerate the development of highly innovative solutions born from academic research and facilitate access to potential industrial partners. At the end of selection, our project (i.e. ZanzaRaft) was rewarded with other 10 winning projects and gained access to the acceleration phase that aims at verifying the industrial and commercial feasibility of the proposed product.

4.3 Results & Discussions

4.3.1 Hydrogel matrix characterization

The chitosan-based hydrogel, after crosslinking with genipin, appeared as a blue-coloured tablet with a very soft consistency. Due to the liquid foam templating technique, small bubbles, with diameters in the millimetre and sub-millimetre range, were entrapped inside the matrix and allowed it to float in water (**Figure 4.3.1A**). Both these physical features are expected to be useful in terms of increasing baiting towards the hydrogel, since it is known that dark and buoyant objects are used by the mosquito larvae to hide and protect themself from natural predators. Two important aspects to be considered in view of commercializing a product are its conservation and packaging. The hydrogel tablets were sealed in plastic bags and stored in the refrigerator at 4 °C and, after several months, no changes in shape nor dimension could be observed at a qualitative level (**Figure 4.3.1B**).

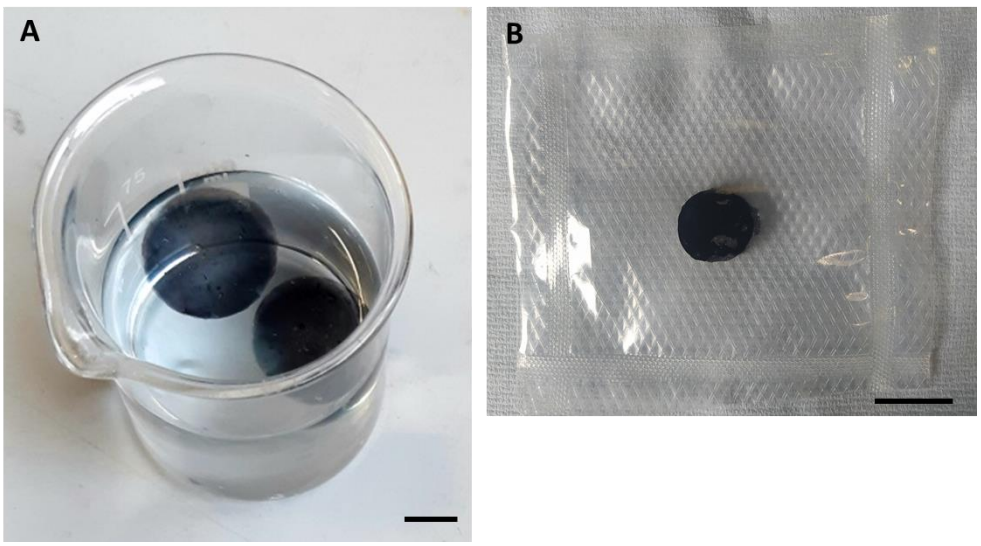

Figure 4.3.1: A) Two hydrogel rafts floating in a beaker full of DI water; B) A sealed plastic bag with a hydrogel tablet on the inside. Scale bar is 15 mm.

Mechanical characterization

The hydrogel elasticity and resistance to fatigue were assessed through uniaxial and cyclic compression tests respectively. Empty matrices (Empty) resulted to have Young's module of 0.17 ± 0.05 kPa and a softening degree of - 48.95 ± 14.51 %. These data were comparable with those registered by samples filled with Bti and yeasts (Bti+Y) (E = 0.23 ± 0.05 kPa; SD% = - 34.34 ± 19.75 % (**Figure 4.3.2**). Such mechanical features collocate the hydrogels in the broad category of soft materials (Young's moduli in the range of 10^4-10^9 Pa).

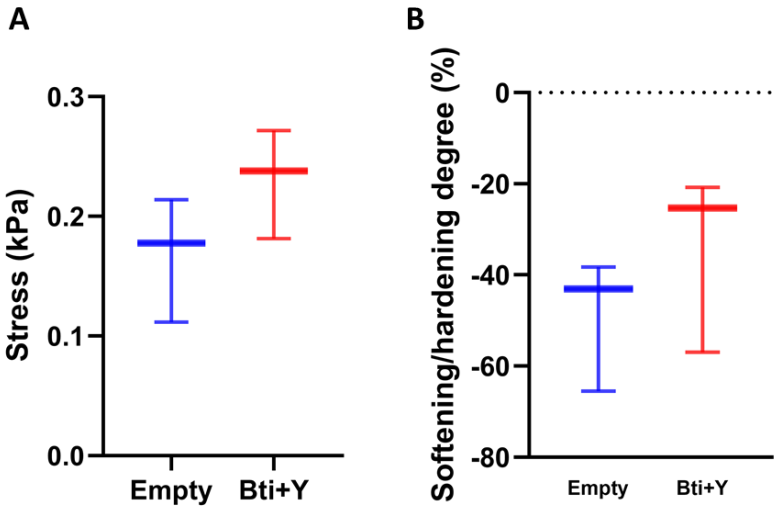

Figure 4.3.2: Young's modulus (A) and softening/hardening degree (B) distributions of Empty and Bti+Y matrices.

Swelling degree and biodegradability

The swelling degree of the hydrogel was measured to predict its behaviour in aqueous environments of possible practical interest, like surface water (IS ≈ 10^{-3} M) and groundwaters (IS ≈ 10^{-2} M) (**Figure 4.3.3A**). The hydrogel was found to consistently increase its weight from 0 mM to 50 mM, both when filled with Bti and yeasts, and as an empty

matrix. A slight shrinkage was registered only when the ionic strength reached the value of 500 mM ($Q\%_{Empty}$ = - 35.97 ± 3.22 %; $Q\%_{Bti+Y}$ = - 49.69 ± 3.21%).

A compound degradation is of paramount concern when its usage does not plan to retrieve from the action site. The hydrogel degradation potential was monitored over a period of 28 days in deionised (DI) water at room temperature. From the graph shown in **Figure 4.3.3B** it can be observed that already at day 7, both the Empty and the Bti+Y samples, are quite degraded ($W\%_{Empty}$ = 64.87 ± 12.28 %; $W\%_{Bti+Y}$ = 27.19 ± 11.02 %). Interestingly, the weight loss continued with a steady trend and reached the highest level at day 28th ($W\%_{Empty}$ = 95.22 ± 4.27 % and $W\%_{Bti+Y}$ = 89.15 ± 10.98 %).

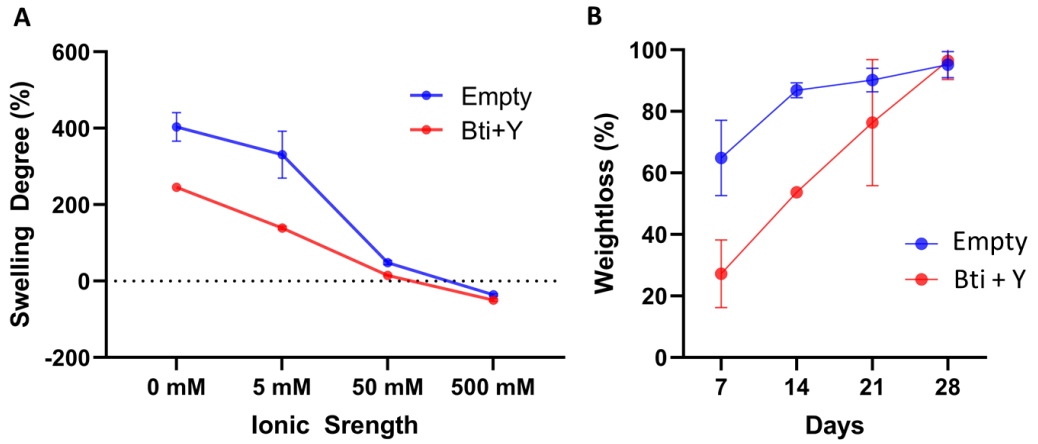

Figure 4.3.3: A) Swelling degree data at different ionic strength (IS): 0 (DI water), 5, 50, 500 mM B) Weight loss percentage after 7, 14, 21, and 28 days in DI water.

4.3.2 Bioassays on mosquito's larvae

Yeasts ingestion

To evaluate the larvae erosion and ingestion of the hydrogel tablet, GFP-tagged yeasts were included in the matrix, so to detect them in the gastrointestinal tract of the insects (**Figure 4.3.4A**). From images

reported in **Figure 4.3.4B**, it is possible to observe small green dots along the entire digestive system of the larvae, which were not detectable in larvae fed with empty matrices. This result attests that the hydrogel rafts filled with yeasts represent an attractive feeding source for mosquito larvae.

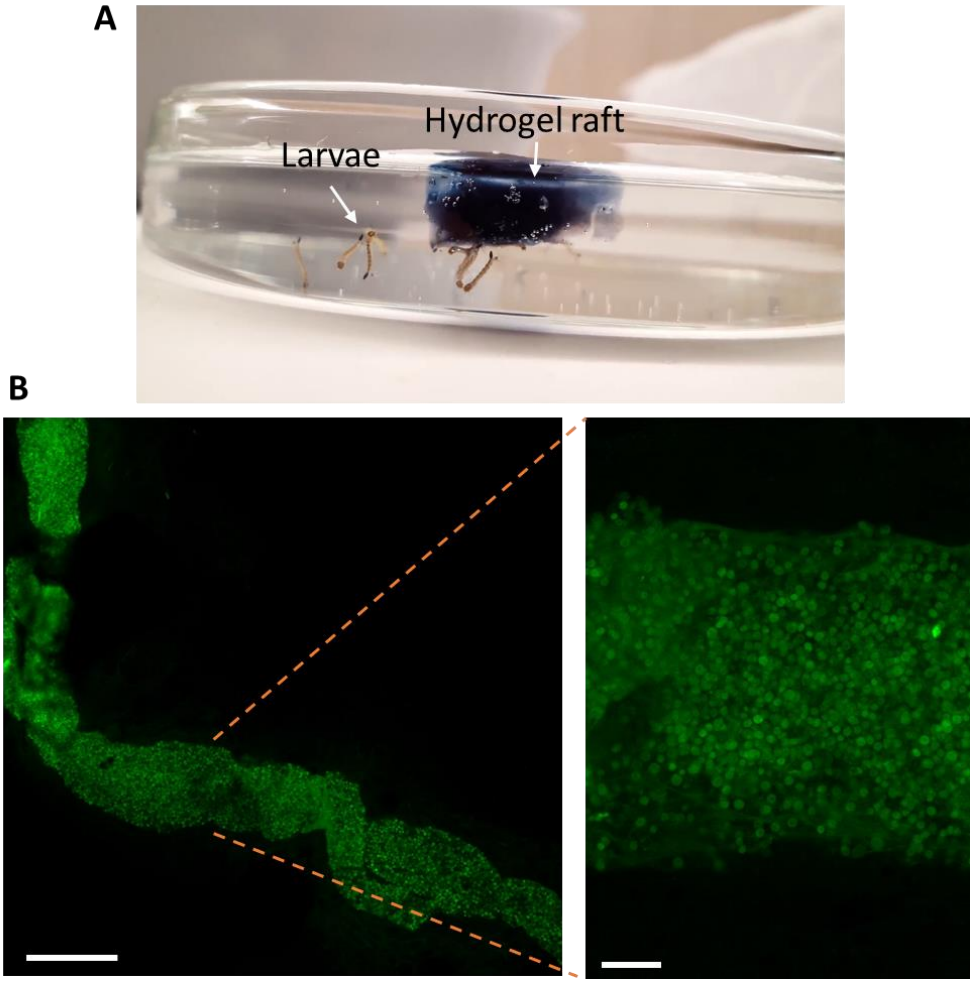

Figure 4.3.4: A) A hydrogel raft filled with GFP-tagged yeasts being eaten by larvae during ingestion tests; B) Confocal image of a larva's intestinal tract (left; scale bar is 250 µm) with a higher magnification frame (right; scale bar is 50 µm). Green dots are fluorescent yeast eaten by the larva.

Yeasts attraction studies

To assess how the presence of Bti and/or of yeasts influenced the larvae behaviour, we monitored and tracked larvae movements in a petri dish with a hydrogel raft fixed in the center.

Figure 4.3.5A show changes in the larvae position in relation to the matrix area (M) as heatmaps. As it can be noted, when an empty matrix is used, it is displaced a uniform blue background colour, demonstrating that larvae not only move much more but also pass the same amount of time in the proximity of borders (border area - B), in the centre of the petri dish (center area - C) or beneath the hydrogel raft (M area). On the opposite, in every other condition, there is a substantially higher density of position (reddish colour) in the centre of the petri dish (i.e. M area), attesting that the larvae behaviour has been conditioned to move towards that region.

The same conclusion can be drawn by the cumulative duration distributions shown in **Figure 4.3.5B**. Larvae spent much more time around/beneath the matrices filled with yeasts (mean value 153.82 s), Bti (mean value 241.80 s), or both (mean value 79.43 s), compared to an empty matrix (mean value 12.85 s).

From these experiments, it seems like the biopesticide Bti possesses an intrinsic attractiveness on mosquito larvae, since yeasts' inclusion in the hydrogel matrix did not induce a significant variation in any of the parameters evaluated.

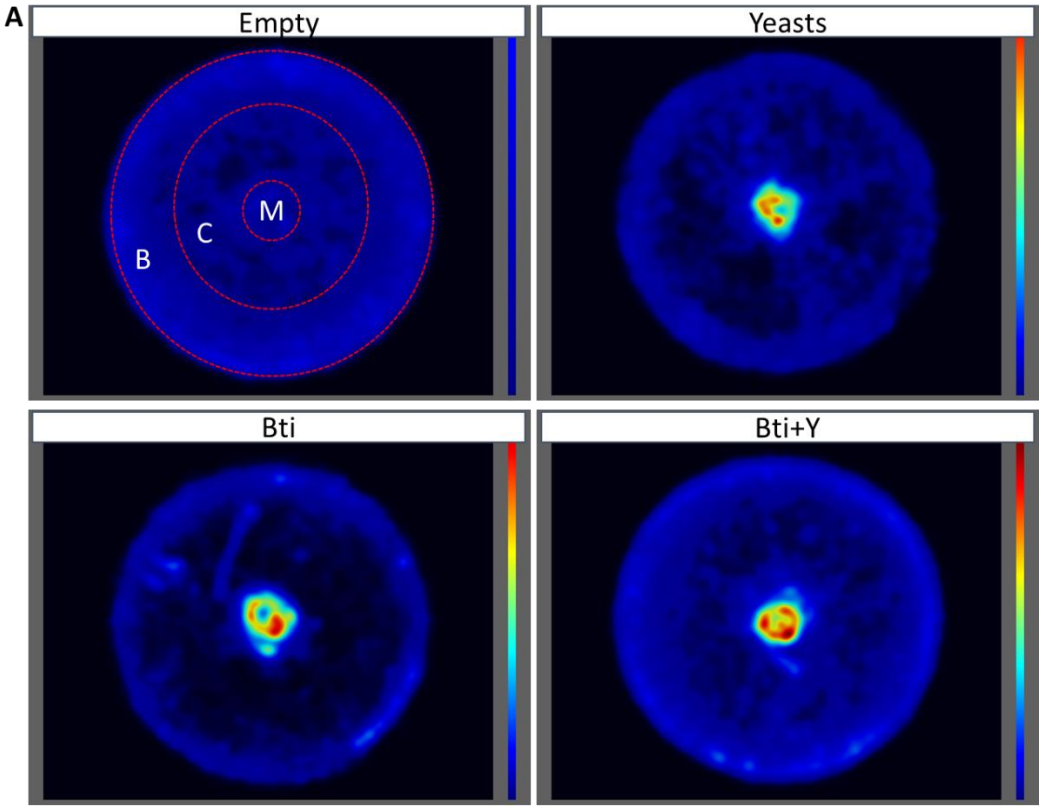
A
Empty
Yeasts
Bti
Bti+Y
M
C
B

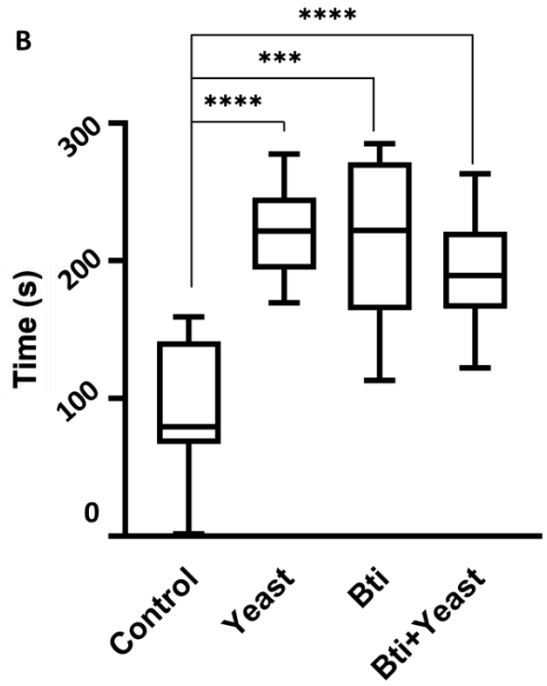
B
****
***
****
300
200
100
0
Time (s)
Control
Yeast
Bti
Bti+Yeast

Figure 4.3.5: A) Heatmaps of larvae position in the petri dish in relation to that one of the hydrogel raft. Red-coloured areas represent zones at higher position density, whether blue-coloured areas of lower position density. M (matrix area), C (central area), B (border area); B) Larvae's cumulative duration distributions around the matrix area of the petri dish. ***$p \leq 0.001$; ****$p \leq 0.0001$.

Biological activity of chitosan rafts on mosquito larvae

Larvae of *Ae. albopictus* (the "tiger mosquito") were exposed to chitosan rafts filled with Bti formulation or with both Bti formulation and yeasts colonies. The bioassay demonstrated that the Bti presence significantly affected the survival of mosquito larvae compared to empty matrices (**Figure 4.3.6**), killing almost always 100 % of the individuals each day. This result undeniably attested that the insecticidal residual activity was stable during all of the testing period (i.e. about 30 days).

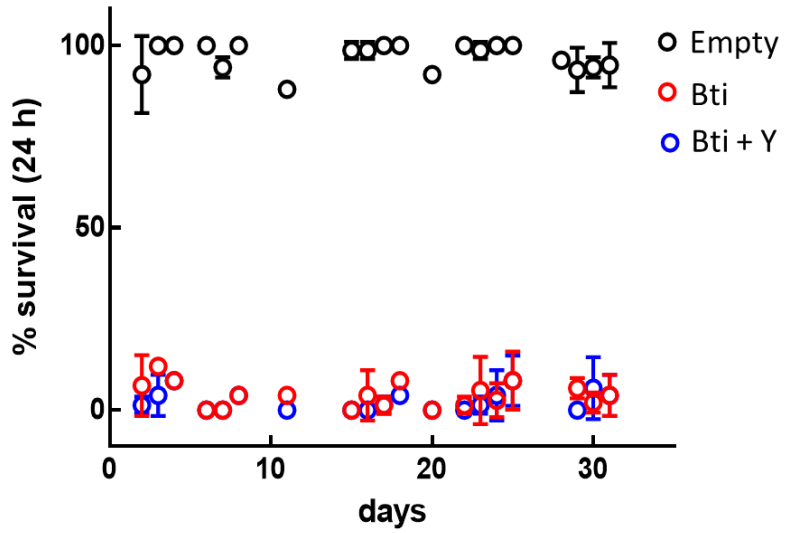

Figure 4.3.6: Survival of *Ae. albopictus* larvae exposed to chitosan rafts with a Bti alone (Bti) or in combination with yeasts (Bti+Y). Controls chitosan rafts (Empty) did not contain any insecticidal molecule nor yeasts. Data were not reported for those days when larvae were not enough to make three replicates for each condition.

4.3.3 Conclusions and future prospects

The proposed smart delivery hydrogel system proved its efficacy towards the selected mosquito model species (i.e. *Ae. albopictus*) by: i) increasing the residual activity of the incorporated biopesticide (Bti) at least up to 28 days; ii) confining Bti activity only at the usage site (i.e. at the mosquitoes breeding site), thus preventing its dispersions in the environment. Moreover, the attested biodegradability of the hydrogel matrix and of the chemical compounds on its inside will help reducing insecticide-derived pollution.

Future advancements on this work will aim at increasing the hydrogel formulation's efficacy. As a matter of fact, the exposure of mosquito larvae to Bti causes midgut damages that allow the entry of midgut flora into the insect body cavity, which ultimately leads to death by septicaemia. By consequence, the larvae immune response efficiency against microorganisms has a mirror impact on Bti toxicity. In this context, engineered yeasts bearing double stranded RNA (dsRNA) capable of targeting those genes most involved in insect cellular immune response, could act as synergists to increase larvae sensitivity towards Bti (and of other candidate insecticides), thus preventing further development of xenobiotic resistances.

4.4 Experimental Section

4.4.1 Chitosan hydrogels' chemical formulation

One hydrogel tablet was prepared by slowly dissolving 10 mg of chitosan (medium MW chitosan, with 75-85% degree of deacetylation) in 1 ml of a 1% acetic acid solution and by adding few droplets of a 20 mM surfactant solution (sodium dodecyl sulphate - SDS). The whole solution was stirred for 1 h at 300 rpm at room temperature (RT). After this, 100 µl of a 44 mM Genipin solution (EtOH 10 %) were added. At this stage, 50 µl of *Bacillus thuringiensis var. israelensis* (VectoBac® 12 AS - Bti) and 10^7 yeast cells (*S. cerevisiae*) were pipetted as well inside the solution of all samples except for those used as negative control (Empty matrices). Stirring was carried out for another hour to blend everything together at 600 rpm at RT and then, the pre-polymer solution was pipetted in custom-made aluminium moulds (1.260 ml for each well). To enable crosslinking the mould was placed in the oven at 37°C overnight.
The solidified hydrogel tablets were mould as small cylinders (diameter of 16 mm and height of 5 mm).
All reagents were purchased from Sigma Aldrich but Genipin, which was bought from Wako Chemicals.

4.4.2 Liquid foam templating technique

To enable hydrogel tablets to buoyance in water, small air bubbles were entrapped in the matrix using an *ad-hoc* liquid foam templating technique (**Figure 4.4.1**). In order to do this, the pre-polymer hydrogel solution, prepared as described in section 4.4.1, was first cured at 42 °C in the oven to increase viscosity. Matrices with Bti and yeasts (Bti+Y) or Bti alone were cured for 35 min, whereas empty matrices for 1.10 h. After this, a syringe pump in combination with vigorous stirring (1000 rpm) was used to inflate air bubbles in the viscous solution at a controlled

rate (10 µl/min) as depicted in **Figure 4.4.1**. The procedure lasted for roughly 2 min and then, the solution was finally pipetted in the designated aluminium mould to be cured in the oven overnight (T = 37 °C).

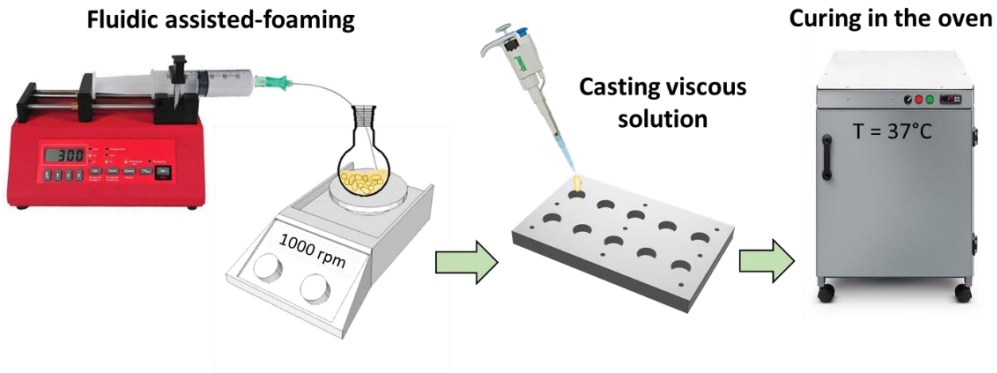

Figure 4.4.1: Diagram of the liquid foam templating technique employed to made floating hydrogel rafts.

4.4.3 Swelling degree measurements

Cured hydrogels were weighted right after synthesis ($W_{relaxed}$) and then equilibrated in a large excess of NaCl aqueous solutions of increasing ionic strength (0 mM, 5 mM, 50 mM, and 500 mM) for 24 h at room temperature. Then, samples were removed from the water, gently tapped onto filter paper, and weighed to determine their fully swollen weight (W_{swell}). Three samples were used for each condition. The swelling capabilities of the hydrogel were expressed in terms of mass swelling ratio (Q%), calculated as:

$$Q\% = \frac{(W_{swell} - W_{relaxed})}{W_{relaxed}} \text{x } 100 \qquad (4.1)$$

4.4.4 Weight loss measurements

Hydrogel tablets were synthetised and weighted after being immersed in DI water for 24 h (W_0). Following this operation, samples were immersed again in DI water and weighted on the designated time point (W_t), specifically at 7, 14, 21, and 28 days. Three samples were used for each condition. When weighing wasn't possible, the sample was considered fully degraded (null weight). Weigth loss percentage was calculated as follow:

$$W\% = \frac{(W_t - W_0)}{W_0} \text{ x } 100 \quad (4.2)$$

4.4.5 Mechanical tests

All mechanical tests were performed using a traction machine (TVM-N, Sauter) coupled with a dynamometer (FH-10, Sauter) and the relative software (AFH-FAST/FD, Sauter).
Samples were always immersed in DI water for 24 h at RT prior testing. Three independent specimens were tested for every condition analysed.

Uniaxial compression
Uniaxial compression tests were performed on hydrogel tablets with a deformation rate of 5 mm/min. The stress (σ) was evaluated as the ratio between the force measured by the load cell and the undeformed specimen cross-section. Strain (ε) was determined as the ratio between the crosshead displacement and the specimen height. Young's moduli were obtained considering the elastic region of the stress-strain curve and calculated as follow:

$$E = \frac{\sigma}{\varepsilon} \quad (4.3)$$

Cyclic dynamic compression
Cyclic dynamic compression tests were performed maintaining a frequency of 1 Hz for 100 cycles. Compression was tested at 50 % calculated relatively to the initial scaffold heights. Softening/hardening degree (SD) was calculated as the ratio between the difference of the last and initial stress, over the initial stress as follow:

$$SD = \frac{(\sigma_f - \sigma_i)}{\sigma_i} \text{ x } 100 \quad (4.4)$$

4.4.6 larvae culture

Larvae of *Aedes albopictus* were used to study the insecticidal activity of chitosan rafts. The larvae came from the Italian Rimini laboratory strain, established in 2004 from mosquitoes collected in Rimini, Italy [156]. The colony was maintained in the insectary under standard rearing conditions (27 ± 1°C, 65%-80% relative humidity, 12:12 hours light/dark photoperiod). 4th instar larvae were used in every bioassay at the

4.4.7 Yeast ingestion assay

A transformed S. cerevisiae colony expressing GFP (green fluorescent protein) was used. Before testing, GFP was induced with galactose at 30 % for 3 h at 30 °C. Yeasts were then centrifuged to be included in the hydrogel matrix as described in **Chapter 4.4.1**.
Larvae were immersed in a petri dishes filled with 50 ml of tap water and were starved for 12 h. At this point, a hydrogel raft containing GFP-yeasts was introduced in the culture environment for 24 h. Fluorescence was evaluated with a confocal microscope SIM A1 (Nikon) at the UNITECH NOLIMITS facility of the University of Milan.

4.4.8 Yeast attraction studies

One larva per condition was placed in a petri dish filled with 5 ml of tap water where a hydrogel raft was previously fixed in the center. The petri was then inserted in a pre-warmed plate holder of the DanioVision system equipped with a Basler camera containing an infrared filter (Noldus Information Technology, NL). Ten larvae were used for every condition (Empty matrix, Bti matrix, Yeast matrix, Bti+Y matrix). Acquisition lasted always 1 h and larvae movements were evaluated in relation to three different areas of the petri dish: a matrix area (M), equivalent to the that one of hydrogel tablet; a central area (C), in close proximity of the hydrogel tablet; a border area (B), at the petri dish periphery.

4.4.9 Mortality tests

First of all, preliminary toxicity bioassays on mosquito larvae were performed to evaluate the quantity of Bti formulation (VectoBac® 12 AS) to be included in chitosan rafts. At this point, larvae were exposed to the rafts according to the guidelines for laboratory and field testing of mosquito larvicides [157]. Briefly, batches of 25 larvae were transferred by means of plastic Pasteur pipettes to disposable plastic cups containing 100 ml of tap water. Then, chitosan rafts with Bti formulation (Bti), with Bti formulation and yeasts (Bti+Y) or empty (controls) were gently introduced in the water and experimental cups were placed in the insectary. Larval mortality was recorded after 24 hours. Chitosan rafts were moved to another plastic cup, with fresh tap water and 25 larvae, to start a new 24-h bioassay. The insecticidal activity of chitosan rafts was recorded across an overall period of 30 days. Three batches of 25 larvae were used to measure mortality for each experimental condition.

4.4.10 Statistical Analyses

Data analyses were performed using the GraphPad Prism 8 software. Values are always shown as mean value ± standard deviation unless otherwise noted. Regarding box plots, boxes show the median value, 25th and 75th quartile ± Tukey whiskers (1.5 times the interquartile range, IQR).
For yeasts attraction tests a one-way ANOVA test with Tukey's post hoc test for multiple comparisons was performed. The significant threshold was set at 5% and computing a two-tailed p value.

5 Summary Table

2D	Bi-Dimensional
3D	Three-Dimensional
3D-FGH	Three-Dimensional Functionally Graded Hydrogel
4HBA	4-Hydroxybutyl Acrylate
AC	Alternating Current
AM	Additive Manufacturing
AN	Acrylonitrile
AOI	Area Of Interest
RGD	Arg-Gly-Asp
BCF	Body/Caudal Fin
BL	Basal Lamina
Bs	Bacillus Sphaericus
BSA	Bovine Serum Albumin
Bti	Bacillus Thuringiensis Var. Israelensis
BTJ	Bone-Tendon junction
CAD	Computer-Aided Design
CIMaINa	Interdisciplinary Centre for Nanostructured Materials and Interfaces
DC	Direct Current
DE	Dielectric Elastomer
DF	Differentiation Medium
DIC	Digital Image Correlation
DMEM	Dulbecco's Modified Eagle Medium
DOPA	3,4-Dihydroxy-L-Phenylalanin
dsRNA	Double Stranded RNA
ECM	Extracellular Matrix
EGDMA	Ethylene Glycol Dimethacrylate
ES	Electric Stimulation
ESF	European Science Foundation
FBS	Fetal Bovine Serum
FDM	Fused Deposition Modelling
FG	Functionally Graded
FN	Fibronectin
GFP	Green Fluorescent Protein
GM	Growth Medium
HEMA	2-Hydroxyethyl Methacrylate
HS	Horse Serum
IS	Ionic Strength

LFT	Liquid Foam Templating
LMN	Laminin
MTJ	Muscle-Tendon junction
Na-4-VBS	Na-4-vinylbenzenesulfonate
NIPAM	N-isopropylacrylamide
NMJ	Neuromuscular Junction
PBS	Phosphate-Buffered Saline
PDMS	Polydimethylsiloxane
PGA	Poly(Glycolic Acid)
PLA	Poly(Lactic Acid)
PLC	Poly(ε-Caprolactone)
Pt	Platinum
PU	Polyurethane
PVA	Poly(Vinyl Alcohol)
RT	Room Temperature
RVE	Representative Volume Elements
SD	Softening/hardening Degree
SDS	Sodium Dodecyl Sulphate
SEM	Scanning Electron Microscopy
SLA	Stereolithography
SMTE	Skeletal Muscle Tissue Engineering
TMT	Tendon-Muscle-Tendon
TRITC	Tetramethylrhodamine
VML	Volumetric Muscle Loss
WHO	World Health Organization
WSS	Wall-Shear Stress
μCT	Micro-Computed Tomography

6 Bibliography

1. Rinaldi A. Naturally better. *EMBO Rep.* 8, 995–999 (2007).
2. MacKinnon R. B. et al. Promises and Presuppositions of Biomimicry. *Biomimetics.* 5, 33 (2020).
3. European Science Foundation. *et al.* Nature-Inspired Science and Engineering for a Sustainable Future. *Sci. Policy Brief.* (2012).
4. Liu Z. *et al.* Functional gradients and heterogeneities in biological materials: Design principles, functions, and bioinspired applications. *Prog. Mater. Sci.* 88, 467–498 (2017).
5. Weaver J. C. *et al.* The stomatopod dactyl club: A formidable damage-tolerant biological hammer. *Science.* 336, 1275–1280 (2012).
6. du Plessis A. *et al.* Beautiful and Functional: A Review of Biomimetic Design in Additive Manufacturing. *Addit. Manuf.* 27, 408–427 (2019).
7. Yang Y. *et al.* Recent Progress in Biomimetic Additive Manufacturing Technology: From Materials to Functional Structures. *Adv. Mater.* 30, 1–34 (2018).
8. Wehner M. *et al.* An integrated design and fabrication strategy for entirely soft, autonomous robots. *Nature.* 536, 451–455 (2016).
9. Mannoor M. S. *et al.* 3D printed bionic ears. *Nano Lett.* 13, 2634–2639 (2013).
10. Fisch M. The Nature of Biomimicry: Toward a Novel Technological Culture. *Sci. Technol. Hum. Values* 42, 795–821 (2017).
11. Laschi C. *et al.* Soft robotics: Technologies and systems pushing the boundaries of robot abilities. *Sci. Robot.* 1, 1–12 (2016).
12. Yang G.-Z. *et al.* The grand challenges of Science Robotics. *Sci. Robot.* 3, 7650 (2018).
13. Rus D. & Tolley M. T. Design, fabrication and control of soft robots. *Nature.* 521, 467–475 (2015).
14. Merceron T. K. *et al.* A 3D bioprinted complex structure for engineering the

muscle-tendon unit. *Biofabrication.* 7, 35003 (2015).

15. Porter M. M. *et al.* 3D-printing and mechanics of bio-inspired articulated and multi-material structures. *J. Mech. Behav. Biomed. Mater.* 73, 114–126 (2017).
16. Baldino L. *et al.* Regeneration techniques for bone-To-Tendon and muscle-To-Tendon interfaces reconstruction. *Br. Med. Bull.* 117, 25–37 (2016).
17. Kempaiah R. & Nie Z. From nature to synthetic systems: Shape transformation in soft materials. *J. Mater. Chem. B.* 2, 2357–2368 (2014).
18. Peppas N. A. *et al.* Hydrogels in biology and medicine: From molecular principles to bionanotechnology. *Adv. Mater.* 18, 1345–1360 (2006).
19. Peppas N. A. *et al.* Hydrogels in pharmaceutical formulations Hydrogels in pharmaceutical formulations. *Eur. J. Pharm. Biopharm.* 6411, 27–46 (2000).
20. Peppas N. A. & Khare A. R. Preparation, structure and diffusional behavior of hydrogels in controlled release. *Adv. Drug Deliv. Rev.* 11, 1–35 (1993).
21. Chang C. *et al.* Superabsorbent hydrogels based on cellulose for smart swelling and controllable delivery. *Eur. Polym. J.* 46, 92–100 (2010).
22. Peng X. & Wang H. Shape Changing Hydrogels and Their Applications as Soft Actuators. *J. Polym. Sci. B Polym. Phys.* 1314–1324 (2018).
23. Hu Z. *et al.* Synthesis and application of modulated polymer gels. *Science.* 269, 525–527 (1995).
24. Leng, L. *et al.* A. Mosaic hydrogels: One-step formation of multiscale soft materials. *Adv. Mater.* 24, 3650–3658 (2012).
25. Kazi G. A. S. *et al.* Fabrication of single gel with different mechanical stiffness using three-dimensional mold. *J. Biomed. Mater. Res. - Part A.* 107, 6–11 (2019).
26. Kim J. *et al.* Designing responsive buckled surfaces by halftone gel lithography. *Science.* 335, 1201–1205 (2012).
27. Elsing J. *et al.* Toward Functionally Graded Polymer Foams Using Microfluidics. *Adv. Eng. Mater.* 19, 1–5 (2017).
28. Ionov L. Biomimetic hydrogel-based actuating systems. *Adv. Funct. Mater.* 23, 4555–4570 (2013).
29. Erol O. *et al.* Transformer Hydrogels: A Review. *Adv. Mater. Technol.* 4, 1–27 (2019).
30. Deligkaris K. *et al.* Hydrogel-based devices for biomedical applications. *Sens.*

Actuators B Chem. 147, 765–774 (2010).

31. Andrieux S. *et al.* Liquid foam templating – A route to tailor-made polymer foams. *Adv. Colloid Interface Sci.* 256, 276–290 (2018).
32. Mac Murray B. C. *et al.* Poroelastic Foams for Simple Fabrication of Complex Soft Robots. *Adv. Mater.* 27, 6334–6340 (2015).
33. Luo R. *et al.* Gradient porous elastic hydrogels with shape-memory property and anisotropic responses for programmable locomotion. *Adv. Funct. Mater.* 25, 7272–7279 (2015).
34. Migliorini L. *et al.* Low-voltage electrically driven homeostatic hydrogel-based actuators for underwater soft robotics. *Sens. Actuators B Chem.* 228, 758–766 (2016).
35. Santaniello T. *et al.* Hybrid nanocomposites based on electroactive hydrogels and cellulose nanocrystals for high-sensitivity electro–mechanical underwater actuation. *Smart Mater. Struct.* 26, 0964-1726 (2017).
36. Katzschmann R. K. *et al.* Exploration of underwater life with an acoustically controlled soft robotic fish. *Sci. Robot.* 3, 1–13 (2018).
37. Kou H. *et al.* Wireless wide-range pressure sensor based on graphene/PDMS sponge for tactile monitoring. *Sci. Rep.* 9, 1–7 (2019).
38. Andrieux S. *et al.* Highly ordered biobased scaffolds: From liquid to solid foams. *Polymer.* 126, 425–431 (2017).
39. Lau T. H. M. *et al.* Tailored for simplicity: Creating high porosity, high performance bio-based macroporous polymers from foam templates. *Green Chem.* 16, 1931–1940 (2014).
40. van der Net A. *et al.* Highly structured porous solids from liquid foam templates. *Colloids Surfaces A Physicochem. Eng. Asp.* 346, 5–10 (2009).
41. Sfakiotakis M. *et al.* Review of fish swimming modes for aquatic locomotion. *IEEE J. Ocean. Eng.* 24, 237–252 (1999).
42. Li T. *et al.* Fast-moving soft electronic fish. *Sci. Adv.* 3, 1–8 (2017).
43. Christianson C. *et al.* Jellyfish-Inspired Soft Robot Driven by Fluid Electrode Dielectric Organic Robotic Actuators. *Front. Robot. AI.* 6, 1–11 (2019).
44. Punning A. & Anton M. A biologically inspired ray-like underwater robot with electroactive polymer pectoral fins. *IEEE Confrence* 2004, 241–245 (2004).

45. Ueoka Y. *et al.* Chemomechanical polymer gel with fish-like motion. *J. Intell. Mater. Syst. Struct.* 8, 465–471 (1997).
46. Tzeranis D. *et al.* On the Design of an Autonomous Robot Fish. *2006 IEEE Int. Conf. Robot. Biomimetics.* 1–6 (2006).
47. Jusufi A. *et al.* Undulatory Swimming Performance and Body Stiffness Modulation in a Soft Robotic Fish-Inspired Physical Model. *Soft Robot.* 4, 202–210 (2017).
48. Long J. H. & Nipper K. S. The importance of body stiffness in undulatory propulsion. *Am. Zool.* 36, 678–694 (1996).
49. ASTM-2856. Standard Test Method for Open-Cell Content of Rigid Cellular Plastics.
50. Invitrogen. Cell culture basic Handbook.
51. Sigma-Aldrich. Fundamental techniques in cell culture. 3rd edition.
52. Segeritz C. P. & Vallier L. Cell Culture: Growing Cells as Model Systems In Vitro. *Basic Science Methods for Clinical Researchers.* Chapter 9 *(*2017).
53. Kapałczyńska M. *et al.* 2D and 3D cell cultures – a comparison of different. *Arch. Med. Sci.* 14, 910–919 (2016).
54. Knight E. & Przyborski S. Advances in 3D cell culture technologies enabling tissue-like structures to be created in vitro. *J. Anat.* 227, 746–756 (2015).
55. Abbott A. Biology's new dimension. *Nature.* 424, 870–872 (2003).
56. Mouw J. K. *et al.* Extracellular matrix assembly: A multiscale deconstruction. *Nat. Rev. Mol. Cell Biol.* 15, 771–785 (2014).
57. Chaicharoenaudomrung N. *et al.* Three-dimensional cell culture systems as an in vitro platform for cancer and stem cell modeling. *World J. Stem Cells.* 11, 1065–1083 (2019).
58. Cukierman E. *et al.* Taking cell-matrix adhesions to the third dimension. *Science.* 294, 1708–1712 (2001).
59. Pradhan-Bhatt S. *et al.* Implantable three-dimensional salivary spheroid assemblies demonstrate fluid and protein secretory responses to neurotransmitters. *Tissue Eng. - Part A.* 19, 1610–1620 (2013).
60. Anders, M. *et al.* Disruption of 3D tissue integrity facilitates adenovirus infection by deregulating the coxsackievirus and adenovirus receptor. *Proc. Natl. Acad. Sci. U. S. A.* 100, 1943–1948 (2003).

61. Saydé T. *et al.* Biomaterials for three-dimensional cell culture: From applications in oncology to nanotechnology. *Nanomaterials.* 11, 1–29 (2021).
62. Pina S. *et al.* Regenerative Medicine Applications. *Materials.* 12, 1824 (2019).
63. Verjans E. T. *et al.* Three-dimensional cell culture models for anticancer drug screening: Worth the effort? *J. Cell. Physiol.* 233, 2993–3003 (2018).
64. Eltom A. *et al.* Scaffold Techniques and Designs in Tissue Engineering Functions and Purposes: A Review. *Adv. Mater. Sci. Eng.* (2019).
65. Tallawi M. *et al.* Strategies for the chemical and biological functionalization of scaffolds for cardiac tissue engineering: A review. *J. R. Soc. Interface.* 12 (2015).
66. Carmagnola I. *et al.* Functional 3D Tissue Engineering Scaffolds: Materials, Technologies, and Applications. Chapter 11 (2018).
67. Richbourg N. R. *et al.* Tuning the biomimetic behavior of scaffolds for regenerative medicine through surface modifications. *J. Tissue Eng. Regen. Med.* 13, 1275–1293 (2019).
68. Nemani S. K. *et al.* Surface Modification of Polymers: Methods and Applications. *Adv. Mater. Interfaces.* 5, 1–26 (2018).
69. Lee H. *et al.* Mussel-Inspired Surface Chemistry for Multifunctional Coatings. *Science.* 318, 426–431 (2007).
70. Madhurakkat Perikamana S. K. *et al.* Materials from Mussel-Inspired Chemistry for Cell and Tissue Engineering Applications. *Biomacromolecules.* 16, 2541–2555 (2015).
71. Lee H. *et al.* Facile conjugation of biomolecu les onto surfaces via mussel adhesive protein inspired coatings. *Adv. Mater.* 21, 431–434 (2009).
72. Kasper C. Bioreactor systems for tissue engineering. (2008).
73. Palsson B. & Bhatia S. N. Tissue engineering. (2004).
74. Martin I. *et al.* The role of bioreactors in tissue engineering. *Trends Biotechnol.* 22, 80–86 (2004).
75. Wendt D. *et al.* Oscillating perfusion of cell suspensions through three-dimensional scaffolds enhances cell seeding efficiency and uniformity. *Biotechnol. Bioeng.* 84, 205–214 (2003).
76. Schmid, J. *et al.* A perfusion bioreactor system for cell seeding and oxygen-controlled cultivation of three-dimensional cell cultures. *Tissue Eng. - Part C.* 24,

585–595 (2018).
77. Akiyama Y. Nanotechnology and Microfluidic. Design Considerations for Muscle-Actuated Biohybrid Devices. Chapeter 11 (2020).
78. Place T. L. *et al.* Limitations of oxygen delivery to cells in culture: An underappreciated problem in basic and translational research. *Free Radic. Biol. Med.* 113, 311–322 (2017).
79. Dvir T. *et al.* A novel perfusion bioreactor providing a homogenous milieu for tissue regeneration. *Tissue Eng.* 12, 2843–2852 (2006).
80. Mescher A. Junqueras's Basic Histology Text and Atlas. (2016).
81. Nukavarapu S.P. *et al. R*egenerative Engineering of Musculoskeletal Tissues and Interfaces. (2015).
82. Gillies A. R. & Lieber R. L. Structure and function of the skeletal muscle extracellular matrix. *Muscle and Nerve.* 44, 318–331 (2011).
83. Sanes J. R. The basement membrane/basal lamina of skeletal muscle. *J. Biol. Chem.* 278, 12601–12604 (2003).
84. Frontera W. R. & Ochala J. Skeletal Muscle: A Brief Review of Structure and Function. *Behav. Genet.* 45, 183–195 (2015).
85. Cittadella Vigodarzere G. & Mantero S. Skeletal muscle tissue engineering: strategies for volumetric constructs. *Front. Physiol.* 5, 1–13 (2014).
86. Nelson D.L. & Michael C. Lehninger Principles of Biochemistry. (2008).
87. Vannozzi L. *et al.* 3D porous polyurethanes featured by different mechanical properties: Characterization and interaction with skeletal muscle cells. *J. Mech. Behav. Biomed. Mater.* 75, 147–159 (2017).
88. Sartori S. *et al.* Biomimetic polyurethanes in nano and regenerative medicine. *J. Mater. Chem. B Mater. Biol. Med.* 2, 5128–5144 (2014).
89. Ostrovidov S. *et al.* Three-dimensional co-culture of C2C12 / PC12 cells improves skeletal muscle tissue formation and function. *J. Tissue. Eng. Regen. Med.* 11, 582–595 (2017).
90. Bentzinger C. F. *et al.* The emerging biology of muscle stem cells: Implications for cell-based therapies. *Bioessays.* 35, 231–241 (2012).
91. Handschin C. *et al.* External physical and biochemical stimulation to enhance skeletal muscle bioengineering. *Adv. Drug Deliv. Rev.* 82, 168–175 (2015).

92. Pavlidou T. *et al.* Regulation of myoblast differentiation by metabolic perturbations induced by metformin. *PLoS One.* 12, 1–19 (2017).
93. Heher P. *et al.* A novel bioreactor for the generation of highly aligned 3D skeletal muscle-like constructs through orientation of fibrin via application of static strain. *Acta Biomater.* 24, 251–265 (2015).
94. Somers S.H. & Grayson W.L. Protocol for the Use of a Novel Bioreactor System for Hydrated Mechanical Testing. *Front. Cell Dev. Biol.* 9, 661036 (2021).
95. Hronik-Tupaj M. & Kaplan D. L. A review of the responses of two-and three-dimensional engineered tissues to electric fields. *Tissue Eng. - Part B Rev.* 18, 167–180 (2012).
96. Ito A. *et al.* Induction of functional tissue-engineered skeletal muscle constructs by defined electrical stimulation. *Sci. Rep.* 4, 1–7 (2014).
97. Khodabukus A. *et al.* Electrical stimulation increases hypertrophy and metabolic flux in tissue-engineered human skeletal muscle. *Biomaterials.* 198, 259–269 (2019).
98. Chen C. *et al.* Electrical stimulation as a novel tool for regulating cell behavior in tissue engineering. *Biomater. Res.* 23, 1–12 (2019).
99. Ricotti L. & Menciassi A. Biohybrid actuators for robotics: A review of devices actuated by living cells. *Sci. Robot.* 14, 987–998 (2017).
100. Herr H. & Dennis R. G. A swimming robot actuated by living muscle tissue. *J. Neuroeng. Rehabil.* 1, 1–9 (2004).
101. Gao L. *et al.*. Recent progress to engineer the functional biohybrid robots actuated by living cells. *Acta Biomater.* 121, 29–40 (2021).
102. Chan V. *et al.* Development of miniaturized walking biological machines. *Sci. Rep.* 2, 857 (2012).
103. Nawroth J. C. *et al.* A tissue-engineered jellyfish with biomimetic propulsion. *Nat. Biotechnol.* 30, 792–797 (2012).
104. Park S. J. *et al.* Phototactic guidance of a tissue-engineered soft-robotic ray. *Science.* 353, 158–162 (2016).
105. Morimoto Y. *et al.* Biohybrid robot powered by an antagonistic pair of skeletal muscle tissues. *Sci. Robot.* 3, 1–11 (2018).
106. Ricotti L. & Menciassi A. Bio-hybrid muscle cell-based actuators. *Biomed.*

Microdevices. 14, 987–998 (2012).

107. Appiah C. *et al.* Living Materials Herald a New Era in Soft Robotics. *Adv. Mater.* 31, 1807747 (2019).
108. Gerges I. *et al.* Acta Biomaterialia Exploring the potential of polyurethane-based soft foam as cell-free scaffold for soft tissue regeneration. *Acta Biomater.* 73, 141–153 (2018).
109. Karande T. S. *et al.* Diffusion in musculoskeletal tissue engineering scaffolds: Design issues related to porosity, permeability, architecture, and nutrient mixing. *Ann. Biomed. Eng.* 32, 1728–1743 (2004).
110. Santamaría V. A. A. *et al.* Computational methodology to determine fluid related parameters of non regular three-dimensional scaffolds. *Ann. Biomed. Eng.* 41, 2367–2380 (2013).
111. Varley M. C. *et al.* Cell structure, stiffness and permeability of freeze-dried collagen scaffolds in dry and hydrated states. *Acta Biomater.* 33, 166–175 (2016).
112. Melchels F. P. W. *et al.* The influence of the scaffold design on the distribution of adhering cells after perfusion cell seeding. *Biomaterials.* 32, 2878–2884 (2011).
113. Wagner B. A. *et al.* The rate of oxygen utilization by cells. *Free Radic. Biol. Med.* 51, 700–712 (2011).
114. Radisic M. *et al.* High-density seeding of myocyte cells for cardiac tissue engineering. *Biotechnol. Bioeng.* 82, 403–414 (2003).
115. Handschin C. *et al.* External physical and biochemical stimulation to enhance skeletal muscle bioengineering. *Adv. Drug Deliv. Rev.* 82, 168–175 (2015).
116. Ito A. *et al.* Induction of functional tissue-engineered skeletal muscle constructs by defined electrical stimulation. *Sci. Rep.* 4, 1–7 (2014).
117. Otsu N. *et al.* A threshold selction method from gray-level histogram. *IEEE Trans. Syst. Man. Cybern.* C, 62–66 (1979).
118. Doube M. *et al.* BoneJ : free and extensible bone image analysis in ImageJ. *Bone.* 47, 1076–1079 (2010).
119. Schindelin J. *et al.* Fiji: An open-source platform for biological-image analysis. *Nat. Methods.* 9, 676–682 (2012).
120. Shimizu K. *et al.* Assembly of skeletal muscle cells on a Si-MEMS device and their

generative force measurement. *Biomed. Microdevices*. 12, 247–252 (2010).
121. Tremblay E. Entomologia applicata. (1871).
122. Corbi J. J. *et al.* Evaluating the use of predatory insects as bioindicators of metals contamination due to sugarcane cultivation in neotropical streams. *Environ. Monit. Assess.* 177, 545–554 (2011).
123. Sarwar M. Biological Control to Maintain Natural Densities of Insects and Mites by Field Releases of Lady Beetles (Coleoptera: Coccinellidae). *Int. J. Entomol. Nematol.* 2, 21–26 (2016).
124. Gillott C. *Entomology*. 2th Edition (2005).
125. Garibaldi L. A. *et al.* Wild Pollinators Enhance Fruit Set of Crops Regardless of Honey Bee Abundance. *Sciencexpress Reports.* Page 3, 10.1126 (2013).
126. Arora R. & Sandhu S. Breeding insect resistant crops for sustainable agriculture. *Breed. Insect Resist. Crop. Sustain. Agric.* 1–421 (2017)
127. Murray D. A. H. *et al.* Estimating invertebrate pest losses in six major Australian grain crops. *Aust. J. Entomol.* 52, 227–241 (2013).
128. Sarwar M. The Killer Chemicals for Control of Agriculture Insect Pests: The Botanical Insecticides. *Int. J. Chem. Biomol. Sci.* 1, 123–128 (2015).
129. Nault L. R. Arthropod Transmission of plant viruses: A new synthesis. *Ann. Entomol. Soc. Am.* 90, 521–541 (1997).
130. WHO 2017. Vector-borne diseases.
131. Fernando C. L. & Koenraadt C. J. M. Climate change and highland malaria fresh air for a hoy debate. *Am. J. Sociol.* 118, 676–727 (2010).
132. Jackman J. A. & Olson J. K. Mosquitoes and the Diseases they Transmit. *Agric. Commun. Texas A&M Univ. Syst. Ext. Publ.* 1–12 (2011).
133. Rogozi E. Mosquito trapping in recreational parks of selangor and their role in public health. Thesis. (2014).
134. Huang Y. J. S. *et al.* Arbovirus-mosquito vector-host interactions and the impact on transmission and disease pathogenesis of arboviruses. *Front. Microbiol.* 10, 1–14 (2019).
135. Gubler D. J. The global emergence/resurgence of arboviral diseases as public health problems. *Arch. Med. Res.* 33, 330–342 (2002).
136. Effler P. V. *et al.* Dengue fever, Hawaii, 2001-2002. *Emerg. Infect. Dis.* 11, 742–

749 (2005).
137. Pampiglione S. *et al.* Dirofilariasis due to Dirofilaria repens in Italy, an emergent zoonosis: Report of 60 new cases. *Histopathology.* 38, 344–354 (2001).
138. Wong P. S. J. *et al.* Aedes (Stegomyia) albopictus (Skuse): A Potential Vector of Zika Virus in Singapore. *PLoS Negl. Trop. Dis.* 7, 1–6 (2013).
139. Global Invasive Species Database. (2018).
140. European Centre for Disease Prevention and Control. (2018).
141. Möhlmann T. W. R. *et al.* Community analysis of the abundance and diversity of mosquito species (Diptera: Culicidae) in three European countries at different latitudes. *Parasites and Vectors.* 10, 1–12 (2017).
142. WHO. A global brief on vector-borne diseases. (2014).
143. Nelson S. C. & Bushe B. C. Collecting Plant Disease and Insect Pest Samples for Problem Diagnosis. *Soil Crop Manag.* 14, 1–10 (2006).
144. Can Ulu T. *et al.* Effects of different pesticides on virulence and mortality of some entomopathogenic nematodes. *Invertebr. Surviv. J.* 13, 111–115 (2016).
145. Alejandra B. *et al.* Mode of action of Bacillus thuringiensis Cry and Cyt toxins and their potential for insect control. *Toxicon. 49(4): 423–435* (2007).
146. Majambere S. *et al.* Is mosquito larval source management appropriate for reducing malaria in areas of extensive flooding in the Gambia? A cross-over intervention trial. *Am. J. Trop. Med. Hyg.* 82, 176–184 (2010).
147. Walker K. & Lynch M. Contributions of Anopheles larval control to malaria suppression in tropical Africa: Review of achievements and potential. *Med. Vet. Entomol.* 21, 2–21 (2007).
148. WHO. An Operational Manual for Indoor Residual Spraying (Irs) for Malaria Transmission Control and Elimination Second Edition Indoor Residual Spraying. (2013).
149. Zalom F. G. *et al.* Managing resistance is critical to future use of pyrethroids and neonicotinoids. *Calif. Agric.* 59, 11–15 (2005).
150. Ritchie H. & Roser M. Malaria. https://ourworldindata.org/malaria. (2018).
151. Ritchie H. & Roser M. Malaria. https://ourworldindata.org/malaria. (2018).
152. Aktar W. *et al.* Impact of pesticides use in agriculture: Their benefits and hazards. *Interdiscip. Toxicol.* 2, 1–12 (2009).

153. Donnelly M. J. *et al.* Identification, Validation, and Application of Molecular Diagnostics for Insecticide Resistance in Malaria Vectors. *Trends Parasitol.* 32, 197–206 (2016).
154. Mogul M. G. *et al.* Controlled release of biologically active agents for purposes of agricultural crop management. *Resour. Conserv. Recycl.* 16, 289–320 (1996).
155. Ebara M. Smart Biomaterials. Smart Hydrogels. Chapter 2. (2014).
156. Dritsou V. *et al.* A draft genome sequence of an invasive mosquito: An Italian Aedes albopictus. *Pathog. Glob. Health.* 109, 207–220 (2015).
157. WHO. Guidelines for laboratory and field testing of mosquito larvicides. (2005).